

Old Dominion University

## ODU Digital Commons

---

Electrical & Computer Engineering Theses & Dissertations

Electrical & Computer Engineering

---

Spring 2011

# Characterizations of Atmospheric Pressure Low Temperature Plasma Jets and Their Applications

Erdinc Karakas  
*Old Dominion University*

Follow this and additional works at: [https://digitalcommons.odu.edu/ece\\_etds](https://digitalcommons.odu.edu/ece_etds)



Part of the [Electrical and Computer Engineering Commons](#), and the [Plasma and Beam Physics Commons](#)

---

### Recommended Citation

Karakas, Erdinc. "Characterizations of Atmospheric Pressure Low Temperature Plasma Jets and Their Applications" (2011). Doctor of Philosophy (PhD), Dissertation, Electrical & Computer Engineering, Old Dominion University, DOI: 10.25777/yfbs-rj14  
[https://digitalcommons.odu.edu/ece\\_etds/80](https://digitalcommons.odu.edu/ece_etds/80)

This Dissertation is brought to you for free and open access by the Electrical & Computer Engineering at ODU Digital Commons. It has been accepted for inclusion in Electrical & Computer Engineering Theses & Dissertations by an authorized administrator of ODU Digital Commons. For more information, please contact [digitalcommons@odu.edu](mailto:digitalcommons@odu.edu).

CHARACTERIZATIONS OF ATMOSPHERIC  
PRESSURE LOW TEMPERATURE PLASMA JETS AND  
THEIR APPLICATIONS

by

ERDINC KARAKAS

M.Sc. June 2006, Eskisehir Osmangazi University

M.Ed. June 2005, Anadolu University

B.Sc. June 2004, Eskisehir Osmangazi University

B.Sc. August 2003, Eskisehir Osmangazi University

A Dissertation Submitted to the Faculty of  
Old Dominion University in Partial Fulfillment of the  
Requirements for the Degree of


DOCTOR OF PHILOSOPHY

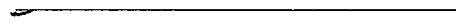
ELECTRICAL AND COMPUTER ENGINEERING

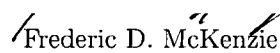
OLD DOMINION UNIVERSITY

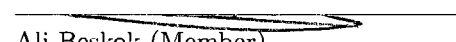
May 2011

Approved by:

  
Mounir Laroussi (Director)

  
Shirhsak K. Dhali (Member)

  
Frederic D. McKenzie (Member)

  
Ali Beskok (Member)

## ABSTRACT

# CHARACTERIZATIONS OF ATMOSPHERIC PRESSURE LOW TEMPERATURE PLASMA JETS AND THEIR APPLICATIONS

ERDINC KARAKAS

Old Dominion University, 2011

Director: Dr. Mounir Laroussi

Atmospheric pressure low temperature plasma jets (APLTPJs) driven by short pulses have recently received great attention because of their potential in biomedical and environmental applications. This potential is due to their user-friendly features, such as low temperature, low risk of arcing, operation at atmospheric pressure, easy hand-held operation, and low concentration of ozone generation. Recent experimental observations indicate that an ionization wave exists and propagates along the plasma jet. The plasma jet created by this ionization wave is not a continuous medium but rather consists of a bullet-like-structure known as "Plasma Bullet". More interestingly, these plasma bullets actually have a donut-shaped makeup. The nature of the plasma bullet is especially interesting because it propagates in the ambient air at supersonic velocities without any externally applied electric field. In this dissertation, experimental insights are reported regarding the physical and chemical characteristics of the APLTPJs. The dynamics of the plasma bullet are investigated by means of a high-speed ICCD camera. A plasma bullet propagation model based on the streamer theory is confirmed with adequate explanations. It is also found that a secondary discharge, ignited by the charge accumulation on the dielectric electrode surfaces at the end of the applied voltage, interrupts the plasma bullet propagation due to an opposing current along the ionization channel. The reason for this interesting phenomenon is explained in detail. The plasma bullet comes to an end when the helium mole fraction along the ionization channel, or applied voltage, or both, are less than some critical values. The presence of an inert gas channel in the surrounding air, such as helium or argon, has a critical role in plasma bullet formation and propagation. For this reason, a fluid dynamics study is employed by a commercially available

simulation software, COMSOL, based on finite element method. Spatio-temporally resolved optical emission spectroscopy (OES) gives the evolution of excited species along the trajectory of the plasma bullets. The APLTPJs' chemical composition includes short-lived species, such as  $He$ ,  $N_2$ ,  $N_2^+$ , and long-lived species, such as  $He^m$  (helium metastable),  $O_3$ ,  $NO$ ,  $NO_2$ . It is worth noting that metastable level excited atoms play an important role in promoting an enhanced chemistry along the plasma jet. Some of the APLTPJs' biomedical applications, such as dental hygiene applications and destruction of amyloid fibrils underlying Parkinson's disease, are explored along with an important discussion showing that the APLTPJs do not have a cytotoxic effect on living cells.

*Dedicated to  
my father Mehmet Erol and my mother Sevinc  
my wife Ummahan and my kids Numan and Levent Ege*

## ACKNOWLEDGEMENTS

It is a pleasure to thank those who made this dissertation possible and inspired me during my doctoral study.

This dissertation would not have been possible without the guidance and help of my advisor, Prof. Mounir Laroussi, who has supported me throughout my Ph.D. research with his patience, motivation, enthusiasm, immense knowledge, and for allowing me the opportunity to work in my own way. His guidance, encouragement, and continuous support helped me the whole time of research and writing of this dissertation. I could not have imagined having a better advisor for my Ph.D study.

I would like to express my sincere appreciation and gratitude to Prof. Shirhsak K. Dhali, Prof. Frederic D. McKenzie, and Prof. Ali Beskok as my thesis committee members for their encouragement and insightful comments.

My deepest gratitude goes to Dr. Tamer Akan for his encouragement leading me to join Dr. Laroussi's group. He was always generous with me sharing his experience and motivation during my career.

Dr. Julien Jarrige deserves special thanks for giving me valuable insights into the relevance of spectroscopic investigations. He was a great friend and colleague with his unselfish and unfailing support.

I am indebted to many of my colleagues. Asma Begum, Nicolas-Mericam Bourdet, and Mehmet Arda Akman, for their help, moral support, and friendship.

My deepest appreciation goes to my family for their unflagging love and support throughout my life. This dissertation would simply be impossible without them. I would like to convey my utmost thanks to my father, Mehmet Erol, my mother, Sevinc, and my brother. Erdem. I would like to express my gratitude to my wife. Ummahan and my sons. Numan and Levent Ege. They were always patient and understanding with me while I was always busy to build our future.

## TABLE OF CONTENTS

	Page
List of Tables . . . . .	ix
List of Figures . . . . .	xv
I INTRODUCTION . . . . .	1
I.1 Atmospheric Pressure Low Temperature Plasma Jets . . . . .	1
I.2 Applications of Atmospheric Pressure Low Temperature Plasma Jets . . . . .	5
I.3 Outline of Present Research . . . . .	6
I.4 Main Targeted Contributions to the Field . . . . .	6
II EXPERIMENTAL SETUP AND PROCEDURES . . . . .	7
II.1 Experimental Setup . . . . .	7
II.2 Procedures . . . . .	9
II.2.1 High voltage pulse generation system . . . . .	9
II.2.2 High voltage and current probes and the wideband oscilloscope . . . . .	9
II.2.3 Intensified charged-couple device (ICCD) camera . . . . .	11
II.2.4 Optical emission spectroscopy system . . . . .	14
II.3 Summary . . . . .	16
III ELECTRICAL CHARACTERISTICS . . . . .	17
III.1 Total Current, Displacement Current, and Discharge Current Measurements . . . . .	17
III.2 Jet Current Measurements . . . . .	22
III.3 Argon Admixture Effect on the Discharge Current . . . . .	23
III.4 Summary . . . . .	25
IV DYNAMICS, FORMATION, AND PROPAGATION . . . . .	26
IV.1 Plasma Bullet Dynamics and its Formation . . . . .	26
IV.1.1 Secondary discharge ignition . . . . .	26
IV.1.2 Electron density estimation in a plasma bullet . . . . .	29
IV.1.3 Streamer theory for the plasma bullet propagation . . . . .	31
IV.1.4 Similarities between the streamers and the plasma bullets . . . . .	34
IV.1.5 Observation of the plasma bullet early formation . . . . .	38
IV.1.6 Photo-ionization vs. helium metastables . . . . .	41
IV.2 Plasma Bullet Propagation and its Inhibition* . . . . .	42
IV.2.1 Correlation between helium mole fraction and plasma bullet propagation <sup>†</sup> . . . . .	43
IV.2.2 Secondary discharge ignition effect . . . . .	55
IV.3 Accurate Measurement of the Plasma Bullet Velocity by Optical Emission Spectroscopy . . . . .	59
IV.4 Summary . . . . .	64
V SPECTROSCOPIC INVESTIGATIONS . . . . .	66
V.1 General Visible-IR and UV Spectra for Different Working Gases . . . . .	66
V.1.1 Visible-IR spectra . . . . .	68
V.1.2 UV spectra . . . . .	71
V.1.3 Argon admixture effect on the helium plasma jet . . . . .	77

V.2	Effects of the Experimental Parameters on Excited Species . . . . .	80
V.2.1	Applied voltage pulse . . . . .	80
V.2.2	Pulse width . . . . .	80
V.2.3	Repetition rate (Frequency) . . . . .	82
V.2.4	Flow rate . . . . .	82
V.3	Spatio-temporally Resolved Distributions of Excited Species . . . . .	86
V.3.1	Spatial behavior . . . . .	86
V.3.2	Temporal behavior . . . . .	86
V.4	Radial Profiles of the Plasma Bullet . . . . .	90
V.5	Rotational and Vibrational Temperature . . . . .	97
V.6	Line Ratio of Helium Line Intensities . . . . .	101
V.7	Summary . . . . .	103
VI	APPLICATIONS IN BIOLOGY AND MEDICINE . . . . .	106
VI.1	Studies on Cytotoxicity of the Plasma Jets . . . . .	106
VI.2	Dental Hygiene Applications of the Plasma Jets* . . . . .	110
VI.2.1	<i>Streptococcus mutans</i> ( <i>S. Mutans</i> ) . . . . .	110
VI.2.2	<i>Porphyromonas gingivalis</i> ( <i>P. gingivalis</i> ) . . . . .	113
VI.2.3	<i>Treponema denticola</i> ( <i>T. denticola</i> ) . . . . .	114
VI.3	Destruction of $\alpha$ -synuclein Based Amyloid Fibrils <sup>i</sup> . . . . .	117
VI.4	Summary . . . . .	120
VII	CONCLUSIONS . . . . .	121
VII.1	Summary and Outlooks . . . . .	121
VII.2	Recommendations for Future Researches . . . . .	125
REFERENCES	. . . . .	127
VITA	. . . . .	137



## LIST OF TABLES

	Page
1 The maximum electron number density. . . . .	29
2 The empirical formula calculation between the plasma bullet velocity and the plasma bullet area for different applied voltages. . . . .	38
3 Penning ionization mechanism . . . . .	46
4 The computational boundary conditions. . . . .	50
5 Kinetics mechanisms in the plasma jet fed by pure helium. . . . .	68
6 Kinetics mechanisms in the plasma jet fed by helium/argon mixture. . . . .	69
7 Energy levels of helium and argon metastables, <i>C</i> level of $N_2$ , and <i>X</i> and <i>B</i> level of $N_2^+$ . . . . .	71
8 Summary statistics of CFU/ml for all samples, where <i>N</i> represents number of the repeated experiments for <i>S. Mutans</i> . . . . .	112
9 CFU/ml repeated measures ANOVA for control versus the exposure times for <i>S. Mutans</i> . . . . .	112
10 CFU/ml repeated measures ANOVA for the consecutive exposure times for <i>S. Mutans</i> . . . . .	112
11 Summary statistics of inactivation factor (IF) for all samples for <i>S. Mutans</i> . . . . .	113
12 Summary statistics for the <i>P. gingivalis</i> samples exposed to the APLT- PJs, where <i>N</i> is the number of the repeated experiments and <i>I</i> is the zone of inhibition. . . . .	116
13 CFU/ml repeated measured ANOVA for the consecutive exposure times of <i>P. gingivalis</i> . . . . .	116

## LIST OF FIGURES

		Page
1	(a) Plasma jet as a continuous medium; (b) ICCD camera pictures showing plasma bullets. Exposure time of the camera is set to 20 ns.	3
2	(a) An illustration of the cathode-directed streamer propagation; (b) streamer propagation model as described in the text, where $\alpha$ is the Townsend's first ionization coefficient. . . . .	3
3	Donut-shaped structure of the plasma bullet [11]. . . . .	4
4	Schematics of the plasma jet devices: (a) plasma pencil; (b) tube reactor.	8
5	Experimental setup showing diagnostics consisting of a monochromator, an ICCD camera, and an oscilloscope. The light emitting from the plasma jet is collected by lenses. . . . .	8
6	High voltage pulse generation system: (a) positive DC power supply; (b) negative DC power supply; (c) pulse generator; (d) single channel arbitrary function generator. . . . .	10
7	Electrical characteristics diagnostics system: (a) high voltage probe; (b) current probe amplifier; (c) current probe; (d) wideband oscilloscope.	11
8	(a) Intensified charged-couple device (ICCD) camera; (b) ICCD camera block diagram [36]. . . . .	13
9	Optical emission spectroscopy system used in experiments: (a) monochromator; (b) controlled scanning system; (c) micrometer controlled entrance slit, (d) photomultiplier tube (PMT); (e) computer. .	15
10	Monochromator diagram showing the entrance and exit slits, mirrors, and grating turrets. . . . .	15
11	An example of the high voltage waveform. HV pulse is 10 kV with a 2 $\mu$ s pulse width . . . . .	18
12	The total current and displacement current for 10 kV HV amplitude and 2 $\mu$ s pulse width. . . . .	18
13	The discharge current as a function of the applied voltage (pulse width: 2 $\mu$ s; repetition Rate: 5 kHz; flow rate: 5.0 L/min). . . . .	20
14	Time of first peak as a function of applied voltage (pulse width: 2 $\mu$ s; repetition Rate: 5 kHz; flow rate: 5.0 L/min). . . . .	20
15	The energy injected into the reactor per pulse (pulse width: 2 $\mu$ s; repetition Rate: 5 kHz; flow rate: 5.0 L/min). . . . .	21
16	The discharge waveform for the plasma pencil (applied voltage: 6 kV. pulse width: 1 $\mu$ s, repetition rate: 5 kHz; flow rate: 5.0 L/min). . . . .	21
17	The jet current measurements along the trajectory of the plasma bullets (applied voltage: 10 kV; pulse width: 2 $\mu$ s; repetition rate: 5 kHz; flow rate: 5.0 L/min). . . . .	23
18	Argon admixture effect on the discharge current and its peak time (applied voltage: 8 kV; pulse width: 2 $\mu$ s; repetition rate: 5 kHz; flow rate: 5.0 L/min). . . . .	24
19	Jet current measurements as a function of the distance to the reactor.	27

20	ICCD camera photographs showing the secondary discharge arising from the positive electrode side then propagating along the ionization channel. After the secondary discharge ignition (2200 ns), the plasma bullet first slows down, and then no longer propagates further (2245 ns) (applied voltage: 9 kV; pulse width: 2 $\mu$ s; repetition rate: 5 kHz; flow rate: 5.0 L/min).	28
21	The plasma bullet velocity during a high voltage pulse (applied voltage: 9 kV; pulse width: 2 $\mu$ s; repetition rate: 5 kHz; flow rate: 5.0 L/min).	30
22	The maximum electron density ( $I_{max}$ ) estimation along the plasma jet axis (applied voltage: 9 kV; pulse width: 2 $\mu$ s; repetition rate: 5 kHz; flow rate: 5.0 L/min).	30
23	The plasma bullet velocity during a high voltage pulse (applied voltage: 9 kV; pulse width: 2 $\mu$ s; repetition rate: 5 kHz; flow Rate: 5.0 L/min).	31
24	A single electron is accelerated towards the original sphere [49].	33
25	Plasma bullet formation processes: (a) Ignition of discharge inside chamber by the electron avalanche; (b) photons are emitted from positively charged plasma, and then photo-ionization occurs at a suitable distance; (c) plasma bullet is formed by the acceleration of photo-electrons towards the positively charged plasma head (an electron avalanche occurs). (d) as the plasma bullet propagates further with the normal succession of the events, it leaves behind an ionization channel consisting of excited states and metastables; (e) while the applied voltage pulse is decreasing to zero, the secondary discharge is ignited due to the charges accumulated on the dielectric electrode. The electrons of this secondary discharge are accelerated towards the head of positively charged bullet by the electric field established by the charges accumulated on the dielectric surface. The motion of the electrons constitutes a current that counters a negative current. This opposing motion of electrons cancels out positive charges of the plasma bullet. Therefore, the electric field between photo-electrons and the head of the plasma bullet becomes almost zero; thus, no more avalanche occurs. Henceforth, the plasma bullet stops propagating further.	35
26	Negative applied voltage and the measured plasma jet current by Rogowski coil. The current is negative as in the anode-directed streamers	36
27	The plasma bullet propagation in the case of the negative applied voltage (applied voltage:-9 kV; pulse width: 2000 ns; repetition rate: 5 kHz; flow rate: 5.0 L/min).	37
28	Experimental setup for the head-on and side-on view ICCD pictures	39

29	The early formation of the plasma bullet: a) applied voltage and discharge current waveforms at the early beginning of the discharge; b) head-on view: early formation inside the wrapped positive electrode (i.e. no propagation started yet); c) side-on view: plasma bullet formation between two electrodes. . . . .	40
30	The plasma bullet early formation generated by a negative applied voltage pulse. . . . .	41
31	The plasma bullet collapsing toward its center for only 1 ns in every 10 ns in the case of a negative applied voltage pulse. . . . .	41
32	Plasma bullet lifetime as a function of the pulse width (applied voltage: 4 kV, repetition rate: 5 kHz; flow rate: 5.0 L/min). . . . .	44
33	The pulse width transition time as a function of the applied voltage (repetition rate: 5 kHz; flow rate: 5.0 L/min). . . . .	45
34	Helium emission intensity at 501.6 nm and plasma jet length versus helium exit velocity. . . . .	47
35	An ICCD camera photograph when the plasma pencil is horizontally positioned with 3 m/s low helium flow velocity. . . . .	48
36	Plasma jet length versus helium velocities for a constant 6 kV, applied high voltage, 1 $\mu$ s pulse width, and 5 kHz repetition rate. Flow regimes are determined by experimental observations using ICCD camera photographs. . . . .	49
37	The computational mesh domain. . . . .	51
38	(a) The helium mole fraction simulation near the helium exit for 8 m/s helium velocity, 6 kV applied high voltage, 1 $\mu$ s pulse width, and 5 kHz repetition rate, (b) Extracted simulation corresponding to the real plasma jet length and structure. For this case, the plasma jet length is 86.7 mm, and the helium mole fraction at the end of plasma jet is 0.445. . . . .	52
39	The minimum corresponding helium mole fraction at the tip of the plasma jet as a function of different helium velocities for a constant 6 kV applied high voltage, 1 $\mu$ s pulse width, and 5 kHz repetition rate. . . . .	53
40	The plasma jet length and the minimum corresponding helium mole fraction at the tip of the plasma jet as a function of applied high voltage for a constant 10 m/s helium flow, 1 $\mu$ s pulse width, and 5 kHz repetition rate. . . . .	54
41	The plasma bullet propagation showing the channel consisting of emitting species along the ionization channel. Secondary discharge ignition causing the plasma bullet inhibition (applied voltage: 5.5 kV; pulse width: 300 ns; repetition rate: 5 kHz; flow rate: 5.0 L/min). . . . .	56
42	Temporal evolution of the reactive species at 20 mm away from the plasma pencil (applied voltage: 5.5 kV; pulse width: 1000 ns; repetition rate: 5 kHz; flow rate: 5.0 L/min). . . . .	57
43	Plasma bullet break-off time for different applied voltages (pulse width: 2000 ns; repetition rate: 5 kHz; flow rate: 5.0 L/min). . . . .	58

44	Secondary discharge propagation at 7 kV applied voltage and 2800 ns pulse width. . . . .	58
45	Showing a shift of the highest emission peak for the plasma bullet velocity measurements. . . . .	60
46	The average plasma bullet velocity for different reactive species as a function of the applied voltage (pulse width: 2000 ns; repetition rate: 5 kHz; flow rate: 5.0 L/min). . . . .	62
47	The instantaneous plasma bullet velocity from the emission of SPS by a time-resolved OES applied voltage: 5.5 kV; pulse width: 2000 ns; repetition rate: 5 kHz; flow rate: 5 L/min). . . . .	63
48	Plasma bullet experiences three different phases: launching, propagation, and ending (applied voltage: 5.5 kV; pulse width: 2000 ns; repetition rate: 5 kHz; flow rate: 5 L/min). . . . .	63
49	General spectra of visible-IR wavelength range for pure helium, helium/oxygen, and helium/argon mixtures. . . . .	70
50	An example energy level diagram of helium. . . . .	72
51	General spectra of UV wavelength range for pure helium, helium/oxygen, and helium/argon mixtures. . . . .	73
52	<i>NO</i> bands between 230 nm and 290 nm for pure helium, helium/oxygen, and helium/argon mixtures. . . . .	76
53	Argon admixture effect on the intensities of the emitting species. The total flow rate is kept at a constant value of 5 L/min. (applied voltage: 9 kV; pulse width: 2 $\mu$ s; repetition rate: 5 kHz). . . . .	79
54	Emission line intensities of the emitting species as a function of the HV pulse amplitude (pulse width: 2 $\mu$ s; repetition rate: 5 kHz; flow rate: 5.0 L/min). . . . .	81
55	Emission line intensities of the emitting species as a function of the pulse width (applied voltage: 9 kV; repetition rate: 5 kHz; flow rate: 5.0 L/min). . . . .	83
56	Emission line intensities of the emitting species as a function of the frequency (applied voltage: 9 kV; pulse width: 2 $\mu$ s; flow rate: 5.0 L/min). . . . .	84
57	Emission line intensities of the emitting species as a function of the flow rate (applied voltage: 9 kV; pulse width: 2 $\mu$ s; repetition rate: 5 kHz). . . . .	85
58	Spatially resolved emission line intensities of the emitting species. These species reach their maxima around 12 mm away from the reactor nozzle (applied voltage: 9 kV; pulse width: 2 $\mu$ s; repetition rate: 5 kHz; flow rate: 5 L/min). . . . .	88
59	Temporally resolved emission line intensities of the emitting species (applied voltage: 9 kV; pulse width: 2 $\mu$ s; repetition rate: 5 kHz; flow rate: 5 L/min). . . . .	89
60	Chordal measurement in the cylindrical coordinates. . . . .	91

61	Radial profiles of excited states for $N_2$ SPS at 337.1 nm, $N_2^+$ FNS, and helium line at 706.4 nm at 10 mm axial position: (a) experimental radial profiles; (b) Abel inverted radial profiles (applied voltage: 8 kV; pulse width: 2 $\mu$ s; repetition rate: 5 kHz; flow rate: 5 L/min). $N_2$ and $He$ lines show almost no emission at the center of the plasma bullet.	93
62	Radial profiles of $N_2$ SPS at 337.1 nm for different axial positions (10 mm, 20 mm, 30 mm, and 40 mm): (a) experimental radial profiles; (b) Abel inverted radial profiles (applied voltage: 8 kV; pulse width: 2 $\mu$ s; repetition rate: 5 kHz; flow rate: 5 L/min). The plasma bullet collapses toward its center as it propagates forward.	94
63	Radial profiles of $N_2$ SPS at 337.1 nm at 10 mm axial position for different applied voltages (7 kV, 8 kV, 9 kV, and 10 kV): (a) experimental radial profiles; (b) Abel inverted radial profiles (pulse width: 2 $\mu$ s; repetition rate: 5 kHz; flow rate: 5 L/min). The cavity at the center of the plasma bullet is more distinctive at higher HV pulse amplitudes.	95
64	Radial profiles of $N_2$ SPS at 337.1 nm for different argon admixtures (0%, 10%, 20%, and 30%): (a) experimental radial profiles; (b) Abel inverted radial profiles (applied voltage: 8 kV; pulse width: 2 $\mu$ s; repetition rate: 5 kHz; flow rate: 5 L/min).	96
65	Comparison of experimental and simulated spectra of $N_2$ SPS for pure helium: (a) 0-0 band, $T_r = 325$ K; (b) $\Delta v = -2(0 - 2, 1 - 3, 2 - 4)$ bands. $T_r = 325$ K, $T_v = 3000$ K (simulated spectra courtesy of J. Jarrige) [12].	99
66	Comparison of experimental and simulated spectra of $N_2$ SPS for different argon admixtures: (a) 0-0 band, $T_r = 325$ K; (b) $\Delta v = -2(0 - 2, 1 - 3, 2 - 4)$ bands. $T_r = 325$ K. $T_v = 3000$ K (simulated spectra courtesy of J. Jarrige) [84].	100
67	Argon admixture effect on the vibrational temperature (courtesy of J. Jarrige) [84].	101
68	Helium line ratio 587.6/706.5 nm as a function of the applied voltage pulse inside the reactor and along the plasma jet.	103
69	Effects of the plasma pencil on cell regeneration after a cut. The plasma exposure duration is 40 seconds.	107
70	Cell regeneration patterns after the plasma pencil exposure: (a) No plasma is exposed to samples; (b) 10 seconds plasma exposure; (c) 20 seconds plasma exposure; (d) 30 sec plasma exposure.	109
71	Mean CFU change over time for <i>S. Mutans</i> .	111
72	<i>P. gingivalis</i> spread over sheep blood agar samples and exposed to the plasma pencil.	114
73	Change in mean zones of inhibition for different exposure times.	115
74	A LIVE/DEAD stain procedure results for <i>T. denticola</i> .	117

75	(a) TEM image of mature intact $\alpha$ -synuclein fibrils, (b), (c), (d), and (e) TEM images of the fibrils after 2, 4, 6, 10 minute exposures to the plasma plume, respectively, showing clear evidence of extensive breakage. . . . .	119
----	--	-----

# CHAPTER I

## INTRODUCTION

In ancient Greece, *Aristotle* first classified matter into five states: earth, water, air, fire, and aether (divine substances)\*. At later times, this classification was mainly used, excluding fire and aether. In the 20<sup>th</sup> century, with modern civilization, ionized gas was classified as a new state called "Plasma". Indeed, this new state was already introduced by *Aristotle* as fire and aether several thousands of years ago. Therefore, *Aristotle's* classification has been justified by putting the fire and aether into one state.

Even though the plasma state was first identified in a Crookes tube by *Sir William Crookes* in 1879, the term plasma was first coined by *Irving Langmuir* in 1928. The physics of plasmas is usually considered difficult since both electromagnetic and fluid dynamics forces are involved. Charged particles inside plasmas interact with each other not only by collisions but also by long-range electromagnetic fields. Most plasmas cannot be considered as a continuous fluid due to their low density ( $10^9 - 10^{13} \text{cm}^{-3}$ ). This discrete fluid structure and complicated electromagnetic calculations often lead to the kinetic theory of plasmas.

The most important characteristic property of plasma is probably quasineutrality having a density  $n_i \approx n_e$  over a plasma length  $L$ . This plasma length  $L$  is often assumed to be much larger than the characteristic length of plasma called *Debye Length*,  $\lambda_{De}$ , ( $L \gg \lambda_{De}$ ), where  $\lambda_{De}$  is given by  $(\frac{\epsilon_0 T_e}{en_0})^{1/2}$ . The quasineutrality condition is often violated around a region called the plasma sheath near walls. The thickness of the plasma sheath is usually in the order of  $5\lambda_{De}$ .

For more detailed information, the reader is referred to the many textbooks on plasma theory [1, 2, 3, 4, 5, 6, 7].

### 1.1 ATMOSPHERIC PRESSURE LOW TEMPERATURE PLASMA JETS

In the last few years atmospheric pressure low temperature plasma jets (APLTPJs) (Figure 1.a) driven by very short pulses have been attracting the interest of researchers. Especially, their enhanced plasma chemistry has marked a new era with

---

\*This dissertation follows the style of *IEEE Transactions on Plasma Science*.



a huge technological impact in biomedical applications [8, 9]. However, the physical properties of the APLTPJs are not well understood. Several experimental results have shown that the APLTPJ is not a continuous medium; rather it consists of a train of bullet-like-structures called plasma bullets, propagating in the ambient air with supersonic velocities in the order of  $10^4$ - $10^5$  m/s without any externally applied electric field (Figure 1.b).

How the plasma bullets reach such high velocities is an intriguing question. Based on a theory suggested by Lu and Laroussi [10], the propagation of a plasma bullet resembles that of streamers. In the streamers, the photo-ionization mechanism plays a main role. Although some aspects of the APLTPJs are well explained by the streamer theory, their homogenous structure, small dimension, and low temperature are difficult to elucidate. In this streamer model, a cathode-directed streamer head containing  $n^+$  positive ions with a sphere of radius  $r_0$  is assumed. Photons emitted by a primary streamer head create photoelectrons at a suitable distance  $r_1$  (Figure 25). Then these photoelectrons are attracted by positive ions towards the sphere due to the influence of the field set by the space charges. Therefore, an avalanche is initiated. If the number of the electrons is sufficiently high, the sphere becomes quasi-neutral. The electrons attracted by the sphere leave behind a new positively charged region. Then the photons emitted from this region cause new photoelectrons at a new suitable distance. This process repeats until the power applied to the propagation path or the amount of feeding gas (i.e. helium mole fraction) along the ionization channel, or both, become inadequate. Hence, the plasma bullet ceases to propagate.

Recently, Laroussi's group also suggested another theory based on surface discharges [11, 12]. In this theory, it was revealed that the plasma bullets propagate similarly as solitary surface wave. Experimental observations supported this idea: A high-speed intensified charged coupled device (ICCD) is placed at a head-on position with respect to the plasma jet. The observation indicated that the plasma bullet actually has a donut-shaped structure (Figure 3), and it propagates along the interface of two media formed by helium gas channel and air. The solitary surface waves were, in fact, predicted by earlier investigators for low temperature plasmas [13].

Ionization and attachment processes dominate the formation of the plasma bullets. Since the plasma bullet travels in the ambient air, electron attachment by air molecules plays a key role. In order to maintain this ionization process, in addition to energy, the propagation channel should always be fed by a new volume of the

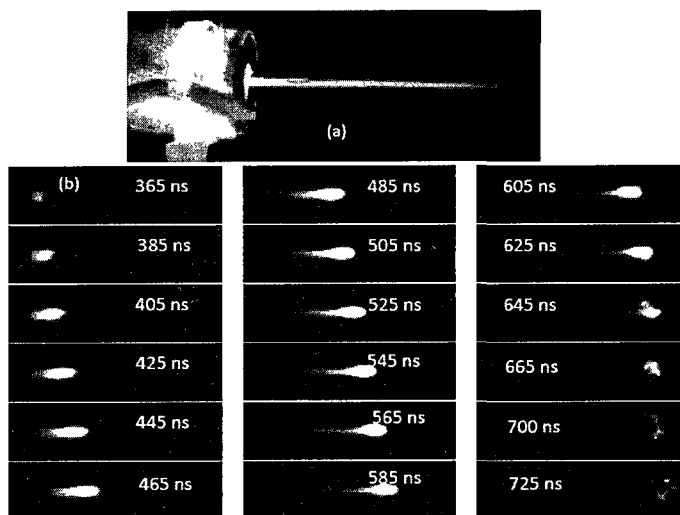


FIG. 1: (a) Plasma jet as a continuous medium; (b) ICCD camera pictures showing plasma bullets. Exposure time of the camera is set to 20 ns.

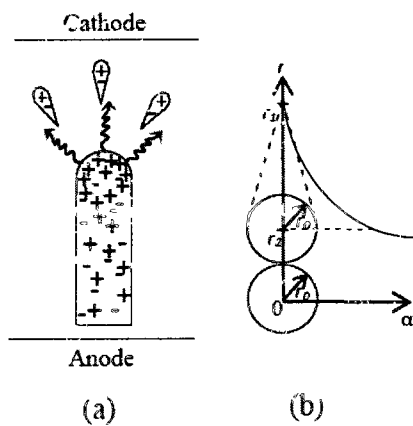


FIG. 2: (a) An illustration of the cathode-directed streamer propagation; (b) streamer propagation model as described in the text where  $\alpha$  is the Townsend's first ionization coefficient.



FIG 3: Donut-shaped structure of the plasma bullet [11].

working gas.

Recently, experimental and modeling studies on the plasma bullet's structure, propagation, behavior, and chemical makeup have led to advancements regarding its properties. New results were presented by many researchers in several discussion forums [14, 15, 16, 17, 18, 19, 20, 21, 22, 23]. Early investigators working on the plasma bullets can be briefly given as follows:

- The first plasma bullet observation emitted by a low temperature plasma jet was reported by Engeman's group in 2004 [24, 25]. Their dielectric barrier discharge (DBD)-like device with two tubular electrodes generates a plasma jet that consists of plasma bullets travelling in air at a velocity of  $15 \times 10^3$  m/s. A sinusoidal high voltage in the order of a few kV at a frequency of 5 to 50 kHz is applied between electrodes. The tube is fed by a helium gas with a velocity of 16.5 m/s.
- In 2005, Laroussi's group observed plasma bullets in their pulsed plasma jet device, known as "Plasma Penci" [10, 11, 26, 27]. A square unipolar high voltage pulse (pulse width is in the range of several hundred nanoseconds) is applied to ring-shaped electrodes with a repetition rate varying from 1 kHz to 10 kHz. Helium flow passing through the electrodes has a flow velocity around 10 m/s (5 L/min flow rate). The bullet velocity is typically in the order of  $10^4$ - $10^5$  m/s depending on the magnitude of applied voltage pulse.
- Kong's group, in 2007, also developed an atmospheric pressure low temperature plasma jet consisting of trains of the plasma bullets using a RF power at 13.56 MHz [28]. Their plasma bullet also travels at high velocities varying from  $7 \times 10^3$  m/s to  $4.31 \times 10^4$  m/s. Their APLTPJ is generated in a dielectric tube.

between a wrapped metal strip as a power electrode and a metal plate as a ground electrode. The working gas is helium, and its flow rate is 5 slm.

## I.2 APPLICATIONS OF ATMOSPHERIC PRESSURE LOW TEMPERATURE PLASMA JETS

APLTPJs are usually operated at atmospheric pressures and generate enhanced gas-phase chemistry when mixed with air, without the need for elevated gas temperatures. These properties of the APLTPJs lead to their extensive use in heat-sensitive applications, such as in material processing and biomedical applications [9, 29].

Especially, their applications in biomedicine are pursued by a number of research efforts [8, 9, 20, 26, 27, 30, 31]. The first paper on biological applications of atmospheric pressure cold plasmas was published in 1996 by Laroussi [32]. This paper was the first attempt to study the interaction of cold plasmas with microbiological cells. This attempt ultimately initiated a new interdisciplinary field. Basically, it was shown that cold plasmas are able to destroy microorganisms living on an exposed medium without damaging the medium itself. Therefore, cold plasmas at atmospheric pressures began promising several novel applications, such as sterilization of heat sensitive materials [26, 33], wound healing [33], blood coagulation [34], amyloid fibrils destruction [35], and others.

The success of low temperature plasmas, including jets, in biological applications emerges from their enhanced gas-phase chemistry. This enhanced chemistry is made possible through the contribution of air molecules. In low temperature plasma jets, the electron energy is much higher than the energies of the ions and neutral species. Therefore, the energetic electrons mainly undergo collisions with the background gas triggering an enhanced level of dissociation, excitation and ionization. Hence, the plasma does not cause any thermal damage to the articles since the heavy species (ions and neutral species) are relatively cold [9].

Experimental results have shown that the charged particles in the APLTPJs indirectly play a role in biological applications. In the case of our plasma jets, the lifetime of the charged particles is very short (usually in the order of the pulse width). These charged particles promote the production of short-lived and long-lived reactive species, such as  $O$ ,  $O_2^*$ ,  $O_3$ ,  $OH$ ,  $NO$ ,  $NO_2$ , etc, which are known to interact with living matter at the cellular level

### I.3 OUTLINE OF PRESENT RESEARCH

This dissertation is organized as follows. After experimental setup and procedures are introduced in chapter II, typical electrical characteristics of the APLTPJs will be presented. These chapters will help the readers understand how the discharge mechanism develops and how the plasma jet is created between two dielectric media. Next, the APLTPJ's dynamics, formation, and structure will be investigated by means of a high-speed ICCD camera. In this chapter, the flow dynamics effect on the plasma jet will also be discussed along with a correlation study between the helium mole fraction and plasma bullet propagation comparing the experimental results with flow dynamics simulations. In addition, the plasma bullet lifetime and its velocity will be determined as a function of several experimental and operating parameters. In order to help developing a model for the plasma bullet formation and its propagation, the jet current will be measured by a Rogowski coil. From these jet current measurements, the electron density will be estimated. In the fourth section, the knowledge obtained from the spatio-temporally resolved optical emission spectroscopy (OES) will be used to determine the chemical makeup of the APLTPJs. Even though the working gas is helium under optimal operating conditions, the advantages, or disadvantages of different working gases will be discussed. A detailed study on the vibrational and rotational temperatures will be shown. In the last chapter, two medical applications of the APLTPJs will be demonstrated: inactivation of oral borne bacteria for dental hygiene and destruction of amyloid fibrils for controlling the progress of Parkinson's disease. In addition, the potentially harmful effects of the APLTPJs, such as cytotoxicity, will be discussed.

### I.4 MAIN TARGETED CONTRIBUTIONS TO THE FIELD

The main contribution of this dissertation to the field will be the exploration of the physical and chemical characteristics of the APLTPJs. The nature of the plasma bullet's supersonic velocities will be investigated along with its formation and propagation dynamics. Power considerations will be also presented in order to determine optimal operating conditions. The chemical makeup of the plasma bullets will be elucidated to understand the kinetic mechanism of the plasma chemistry. Promising biomedical applications of the APLTPJs will be introduced in the last chapter.

## CHAPTER II

### EXPERIMENTAL SETUP AND PROCEDURES

#### II.1 EXPERIMENTAL SETUP

Two different type of electrode configurations have been used in experiments depending on the research focus. In order to generate the plasma plume/jet/bullet, a unipolar square high voltage pulse in the order of 3.5 kV to 10 kV is applied to electrodes with a pulse width ranging from 200 ns to several microseconds. a repetition rate up to 10 kHz, and a helium flow rate between 1 L/min and 7 L/min . For both configurations, the gas is injected into the reactor from the anode side. A discharge is first ignited in the gap between electrodes, and then a plasma plume/jet/bullet comes out from the ground electrode side. The length of the plasma jet can reach up to 90 mm in the surrounding air (i.e. the plasma bullet can travel in the air up to 90 mm).

The first configuration is traditionally known as “Plasma Pencil”, which is made of a 25 mm diameter hollow dielectric tube with two copper ring electrodes attached to the surface of centrally perforated dielectric disks separated by 5 mm (Figure 4.a). The diameter of the hole is about 3 mm. The diameter of the copper ring electrodes is smaller than that of the disk but bigger than that of the hole.

The second configuration is called the “Tube Reactor” (Figure 4.b), which has a simpler geometric structure than that of the plasma pencil. It only consists of a cylindrical Pyrex tube with 3 mm inner diameter and two copper foil electrodes wrapped around the tube. The electrodes are separated by a distance that can be varied from 5 mm to 10 mm. The magnitudes of the applied voltage and pulse width, and the amount of the gas flow rate are relatively higher than those of the plasma pencil.

The entire experimental setup consists of six main components: the reactor with its high voltage pulse generator system and a suite of diagnostic instruments consisting of an oscilloscope, high voltage and current probes, optical emission spectroscopy system. and intensified charge-coupled device (ICCD) camera (Figure 5).

The high voltage pulse generation system includes a high voltage power supply, a high voltage pulse generator, and a single channel arbitrary function generator. The gas flow into the reactor is controlled by a mass flow meter (Bronkhorst High-Tech).

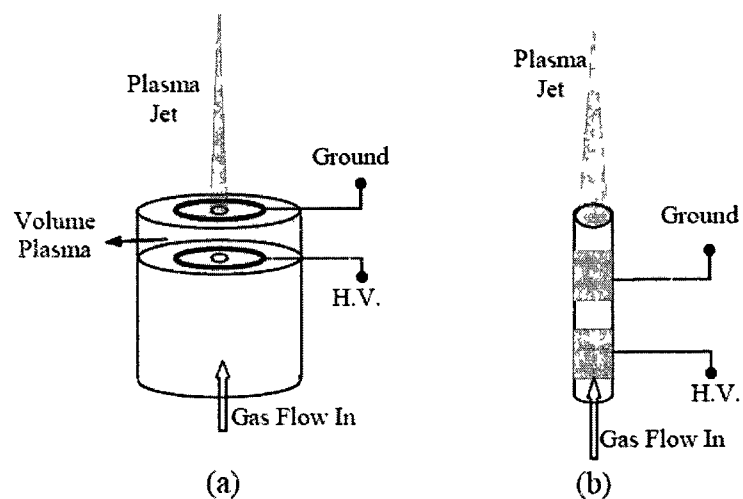


FIG. 4: Schematics of the plasma jet devices: (a) plasma pencil; (b) tube reactor

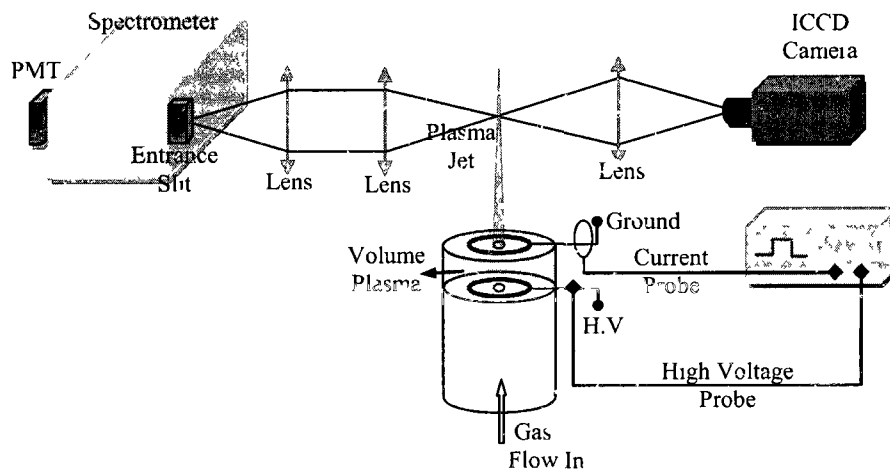


FIG. 5: Experimental setup showing diagnostics consisting of a monochromator, an ICCD camera, and an oscilloscope. The light emitting from the plasma jet is collected by lenses.

The applied voltage and discharge current are measured by high voltage and current probes. The voltage and current waveforms are monitored by a wideband digital oscilloscope. The OES system is composed of a monochromator, a photomultiplier tube (PMT), lenses, and filters.

## II.2 PROCEDURES

There are several key points needed to be addressed for the production and the characterization of the APLTPJs. In this section, we explain these key points in detail.

### II.2.1 High voltage pulse generation system

The high voltage pulse generation system consists of a DC high voltage power supply (Figure 6.a and 6.b) (Spellman SL 1200 Watt maximum power), a high voltage pulse generator (Figure 6.c) (DEI PVX-41, maximum output voltage: 10 kV), and a single channel arbitrary function generator (Figure 6.d) (Tektronix AFG 3021). The high voltage pulse generator converts a DC high voltage input into a pulsed output. The width and repetition rate of this pulse are controlled by a function generator. DC power coming from the power supply directly goes into the pulse generator inputs. The pulse generator has two inputs depending on the polarization of DC voltage (i.e. positive, or negative). The function generator controls the pulse generator. The output voltage of the function generator is adjusted to 5 V in order to properly trigger the pulse generator. If the pulse generator delivers an over current to the reactor more than the allowable limit (or any short circuit occurs), the system needs to be shut down immediately to avoid possible damage to the electronic circuit of the pulse generator. The upper limits of the pulse generator are 10 kV for the high voltage and 10 kHz for the repetition rate.

### II.2.2 High voltage and current probes and the wideband oscilloscope

A P6015A Tektronix high-voltage probe is used to measure the magnitude of the voltage pulse (Figure 7.a). This probe is designed for heavy-duty, high-performance measurements for voltages over 2.5 kV. The upper limit for the measurements is  $20 \text{ kV}_{7ms}$  for DC voltages and 40 kV for pulses (100 ms duration). In addition, 75 MHz



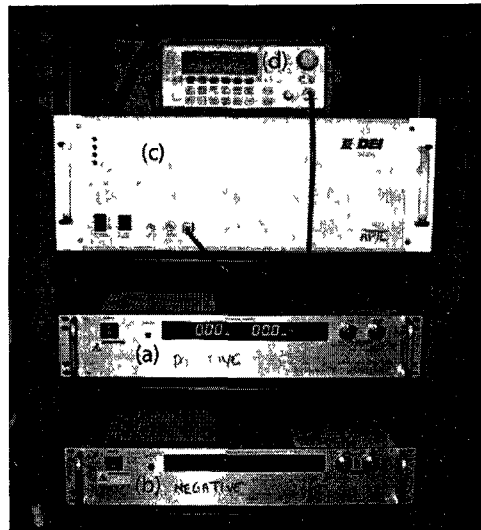


FIG. 6: High voltage pulse generation system: (a) positive DC power supply; (b) negative DC power supply, (c) pulse generator, (d) single channel arbitrary function generator.

bandwidth allows capturing the fast high voltage signals. The voltage waveform is displayed on the oscilloscope.

A TCPA300 current probe amplifier (Figure 7 b) is employed to measure the current waveform. The amplifier converts the sensed current into a proportional voltage signal. DC measurement capability and high bandwidth enable the amplifiers to accurately represent square waves and fast-rise signals.

The current measurement system also consists of a compatible current probe. A TCP312 (30 A, 100 MHz) current probe (Figure 7.c), which is compatible with the TCPA300 amplifier, is used in our experiments. The input impedance of the oscilloscope channel must be  $50 \Omega$ . In order to utilize the full bandwidth of the amplifier, the bandwidth of the oscilloscope needs to be five times larger than that of the current probe.

Degaussing the probe enables removal of any residual magnetization from the probe core. Such residual magnetization can induce measurement error. Auto-balancing also removes unwanted DC offsets in the amplifier circuitry. Failure to degauss the probe is a leading cause of measurement errors.

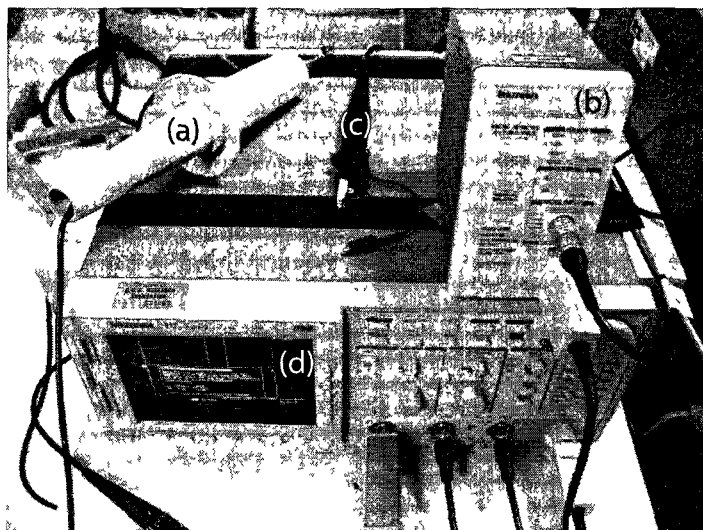


FIG 7. Electrical characteristics diagnostics system: (a) high voltage probe; (b) current probe amplifier; (c) current probe; (d) wideband oscilloscope.

A wideband oscilloscope is needed for the visualization of both the high voltage and the current waveforms. A TDS784D 1 GHz bandwidth Tektronix oscilloscope with four channels is used (Figure 7.d). This oscilloscope contains the high waveform capture rate, advanced triggering, protocol decode, and search capabilities needed to debug.

### II.2.3 Intensified charged-couple device (ICCD) camera

A high performance intensified charged-couple device (ICCD) camera is used with a gating time as low as 3 ns (Figure 8.a). Its 12 bit dynamic range and its high resolution CCD image sensor provide excellent signal-to-noise-ratio and the ability for single photon detection. This camera can be triggered by either electrical or light inputs.

Figure 8 b shows the block diagram of the complete camera system. The light emitted from an object is focused on the photocathode material of the camera. Therefore the photoelectrons are released from the photocathode and then penetrate into a micro channel plate (MCP) producing secondary electrons. Finally, these electrons hit a phosphor screen producing a light emission.

The photocathode is the most sensitive component of the camera. It is made of a thin layer of a material with a low activation energy for electrons and allows a high quantum efficiency from short to long wavelengths [36]. The photocathode material of our camera is S20, a multialkali-green. Its quantum efficiency is almost constant starting from 200 nm to 900 nm. This specification is especially important for the characterization of the plasma bullets. The lifetime of the photocathode material depends on the photocurrent produced by the incident light (i.e. photo effect).

For the light intensification, the secondary photoelectron occurs in the micro channel plate (MCP) made of lead glass and having about  $10^6 - 10^7$  microscopic channels of typically  $6 \mu\text{m}$  in diameter and  $0.5 \text{ mm}$  in length. The intensification mainly depends on the ratio of the channel length to diameter and the applied voltage [36].

After the intensification and acceleration of all electrons towards the phosphor screen by a fixed bias voltage (several KV), the light production occurs. The decay time of the phosphor screen determines how often consecutive pictures can be taken [36].

In order to minimize interaction of electrons with background gas atoms, the photocathode, MCP, and phosphor screen are sealed in a high vacuum device. Excessive light inputs could destroy the light intensification system. It is very important to avoid very long exposure times from room lighting, or short and intense laser beams.

The ICCD camera is connected to the computer with a PCI-interface-board. This board is a dedicated component for the camera. Software called "Sensicam" is used for the operation and control of the camera. Since we are dealing with nanosecond events duration during our experiments, the camera needs to be properly triggered. In our experimental setup, the camera is triggered by the arbitrary function generator that also triggers the pulse generator. The camera control tab in the Sensicam software allows adjusting the camera settings. In order to trigger the system and the camera simultaneously, the external trigger mode is chosen. The delay and exposure times can be also set in this tab. The flow files could be very useful to acquire the consecutive pictures. The camera only takes consecutive pictures with less than 20 ns intervals for the first 50 ns. After this first 50 ns the camera triggered, the picture intervals cannot be less than 20 ns. For that reason, it is sometimes necessary to trigger the camera with a delay. It is also worth noting that a system delay should be taken into account for the exact timing determination of a final picture. The current

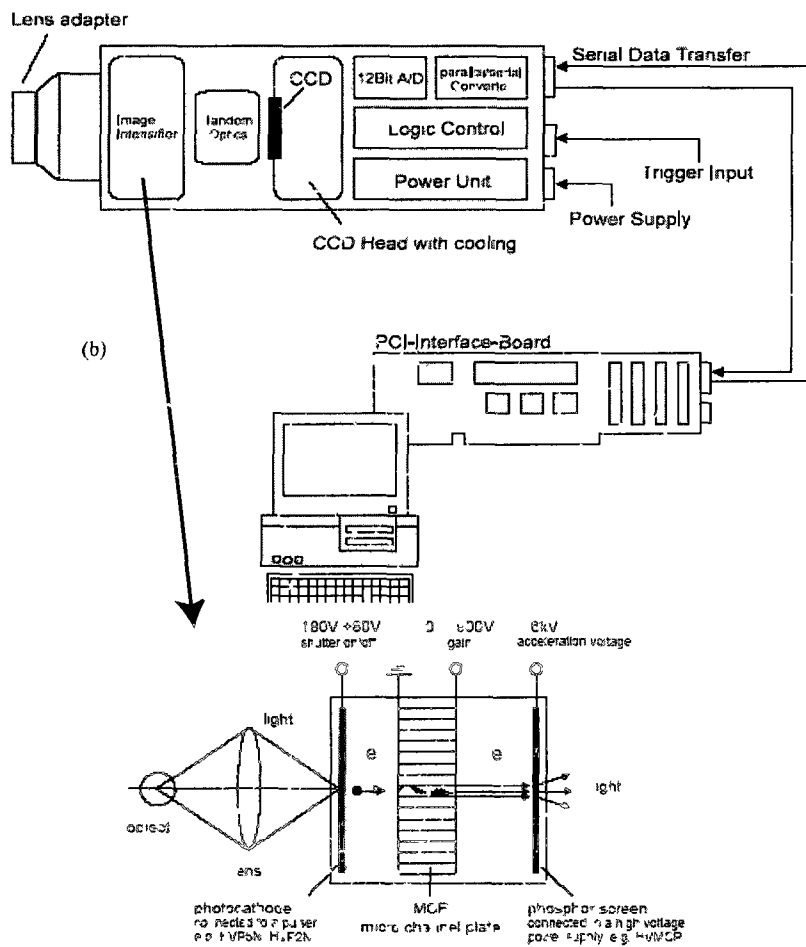
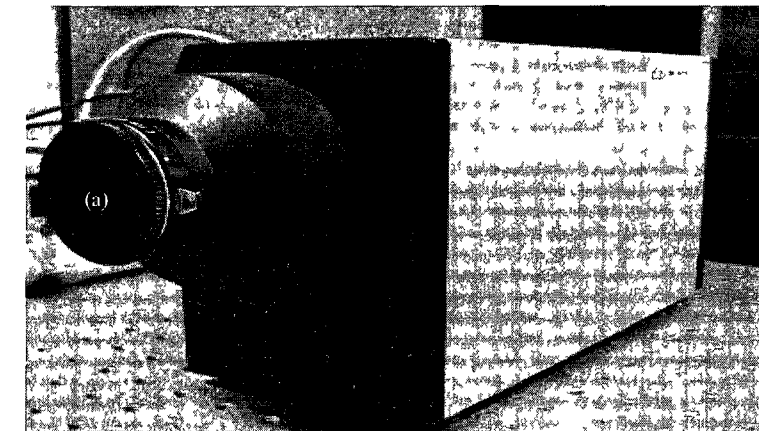


FIG 8 (a) Intensified charged-couple device (ICCD) camera, (b) ICCD camera block diagram [36]

system delay is around 85 ns.

#### II.2.4 Optical emission spectroscopy system

An optical emission spectroscopy system (Figure 9), SpectraPro-500i, is used with a 500 mm focal length monochromator (Figure 9.a) including a double grating turret, an imaging optical system, a 32-bit microprocessor controlled scanning (Figure 9.b), a built-in RS232 and IEEE488 interfaces, and a micrometer controlled entrance slit (Figure 9.c).

The diagram of the monochromator is shown with the entrance and exit slits, mirrors, and grating turrets in Figure 10. The grating is adjusted to 1200 mm/groove for UV to 500 nm range and 3600 mm/groove from 500 nm to far-infrared range. In order to focus the light onto the monochromator, two UV-grade lenses are used to enhance sensitivity of the spatial profile of the emitting species. The slit width is usually kept in the order of several micrometers. The smaller slit width leads to higher resolution with less light intensity. Employing a UV filter for the visible-infrared spectroscopy is a crucial task to prevent the higher order diffraction inside the monochromator. The integration time is usually set between 100 ms and 500 ms. For the temporal profiles, the outlet of the PMT is connected to the oscilloscope after the grating position of the monochromator is adjusted on the software.

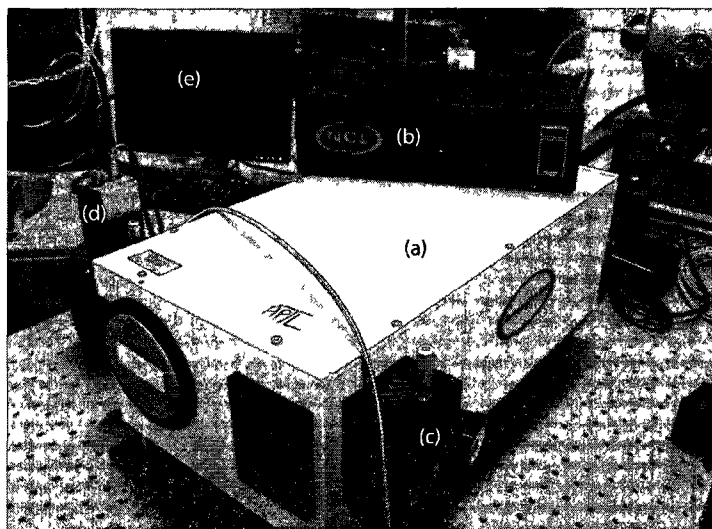


FIG. 9 Optical emission spectroscopy system used in experiments: (a) monochromator, (b) controlled scanning system; (c) micrometer controlled entrance slit; (d) photomultiplier tube (PMT). (e) computer.

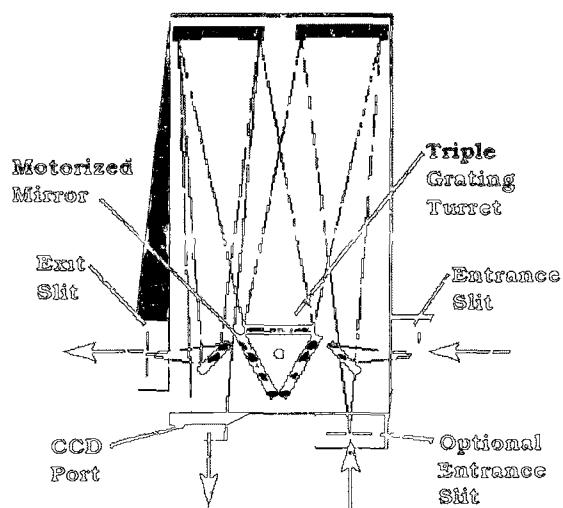


FIG. 10: Monochromator diagram showing the entrance and exit slits, mirrors, and grating turrets.

### II.3 SUMMARY

In this chapter, the components of our experimental setup are introduced along with the operating procedures. Each component of the setup requires special care. Optimization and synchronization issues are crucial steps in our experiments.

The OES system and ICCD camera have to be used properly. The optical parts should be especially designed for the experimental needs; for example, usage of the UV filters for the visible-IR spectrum. Moreover, since these devices are very sensitive to excessive lights or voltages, one should be very careful during the operation.

Details regarding the reactors, such as dimensions and materials, are schematically given in this chapter. In addition, brief technical notes and important operating instructions are summarized for each device that was used in experiments.

## CHAPTER III

### ELECTRICAL CHARACTERISTICS

The current-voltage characteristics of our two atmospheric pressure low temperature plasma jets are presented in this chapter. The tube reactor is the one mainly used in our experiments. Some minor differences between the tube reactor and the plasma pencil are indicated in the text.

In this chapter, four different current waveforms of the APLTPJ reactors will be discussed: the total current, the displacement current, the discharge current, and the jet current. The reactors using the dielectric barrier electrodes show little different behaviors. The total current  $I_{TOT}$  states the conduction current between anode and cathode. The displacement current  $I_{NO}$  is due to the capacitance nature of the devices, including the cable capacitances. The actual discharge current  $I_{DIS}$  waveform can be found by subtracting the displacement current from the total current. Additionally, the plasma jet emitted in the surrounding air carries a current called the jet current,  $I_{JET}$ .

#### III.1 TOTAL CURRENT, DISPLACEMENT CURRENT, AND DISCHARGE CURRENT MEASUREMENTS

We use high voltage (HV) pulses in the operation of the APLTPJs. An example diagram of the pulse is shown in Figure 11. In this particular example, the HV value is set to 10 kV with a pulse width  $2 \mu\text{s}$  and a repetition rate 5 kHz.

Figure 12 shows the total current  $I_{TOT}$  and the displacement current  $I_{NO}$  without helium gas (no plasma). The experimental conditions are as follows: 10 kV applied voltage,  $2 \mu\text{s}$  pulse width, 5 kHz frequency. Operating gas is helium, and its velocity is 10 m/s. The total current  $I_{TOT}$  has two peaks one at the rising and the other at the falling edge of the HV pulse.  $I_{TOT}$  is the sum of the discharge current and the displacement current.

Figure 13 shows the actual discharge current  $I_{DIS}$  waveform after the displacement current is subtracted from the total current. As shown in Figure 13, the discharge current experiences two different peaks. After the high voltage is applied to the electrodes, the current waveform reaches its first peak at around 150 ns. This delay of 150 ns is the time it takes to establish a discharge between the electrodes.



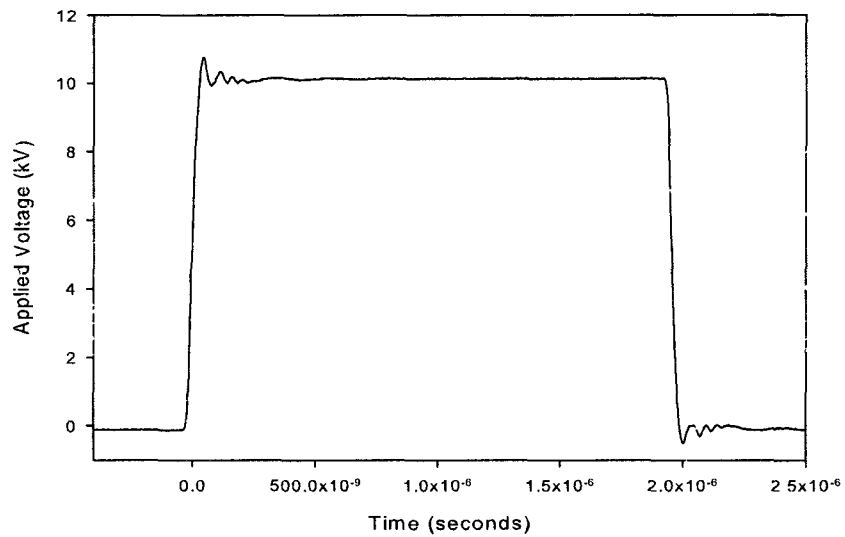


FIG. 11: An example of the high voltage waveform. HV pulse is 10 kV with a 2  $\mu$ s pulse width.

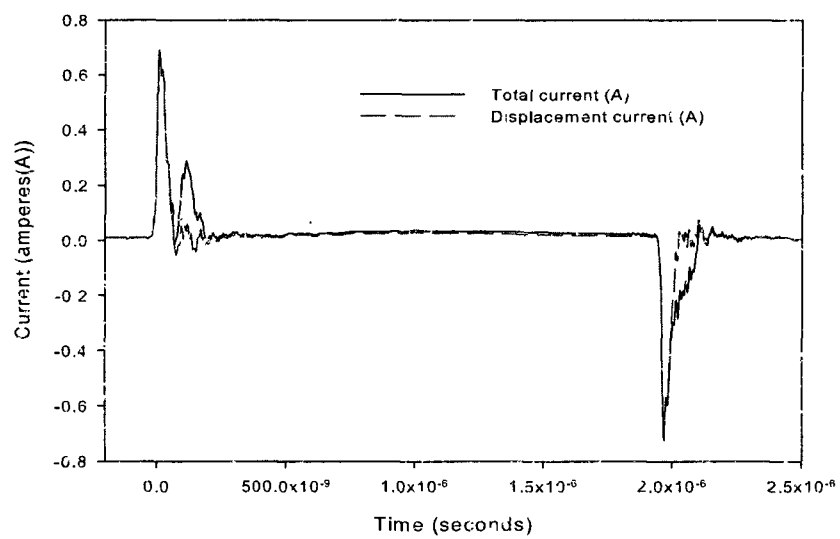


FIG. 12: The total current and displacement current for 10 kV HV amplitude and 2  $\mu$ s pulse width.

This first peak comes to an end 100 ns later. The starting and ending times of this first peak depend on the magnitude of the applied voltage as seen in Figure 13. The shift of this first peak is given in Figure 14 as a function of applied voltage. The second peak, with the negative polarity, is observed at the end of the voltage pulse. This indicates that a secondary discharge occurs even though the applied voltage is very low. This secondary discharge is ignited due to the charged particles accumulated on the surface of the dielectric electrodes during the previous discharge. This phenomenon is already reported in Ref. [37] for the planar-dielectric barrier discharges (DBD). This planar-DBD is a device similar to the plasma pencil but does not emit a plasma plume.

The discharge current waveforms as a function of the applied voltage are also shown in Figure 13. The current amplitude significantly increases with higher applied voltages. The maximum discharge current is 0.22 A for a HV amplitude of 10 kV (i.e. a peak power of 2200 W). Since the applied voltage is very low at the end of the pulse, the power dissipated in the secondary discharge is negligible, and most of the energy is deposited in the jet during the first discharge.

The energy injected into the reactor per pulse as a function of applied voltage is calculated in Figure 15. The energy is relatively low, with a maximum of 0.203 mJ/pulse for a HV amplitude of 10 kV (i.e. a maximum average power of 2.03 W at pulse repetition frequency of 10 kHz). As HV pulse amplitude increases from 4 kV to 10 kV, the energy injected into the reactor per pulse exponentially rises up (Figure 15). Even though no plasma bullet is produced for low applied voltages, a discharge occurs inside the reactor for voltages more than 3.5 kV; therefore, the energy injected could be measured. It is worth noting that the slope of the curve is not significantly influenced by the formation of the plasma bullets. Hence, it can be assumed that the energy necessary for the formation of the plasma bullets comes entirely from the energy injected in the first discharge.

In the plasma pencil configuration, there is another peak (bump) rising to relatively lower values just after the first current peak comes to an end (Figure 16). This observation was already reported in Ref. [10]. It was stated that the time this second peak starts rising corresponds to the launching time of the plasma bullets based on the result of the ICCD camera pictures. This second peak is not observed in the tube reactor and the planar-DBDs [37]. Another interesting difference is the magnitude of the discharge current, which is much higher than that of the tube reactor.

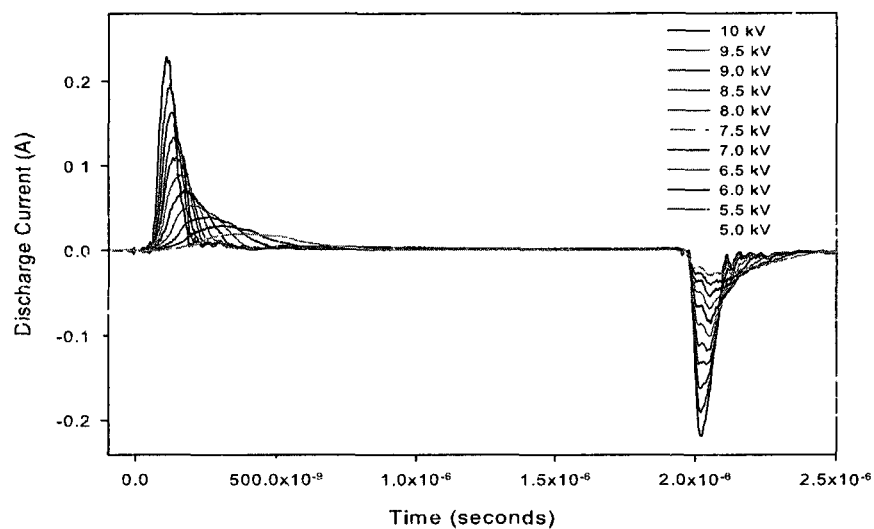


FIG. 13: The discharge current as a function of the applied voltage (pulse width:  $2 \mu\text{s}$ ; repetition Rate: 5 kHz; flow rate: 5.0 L/min).

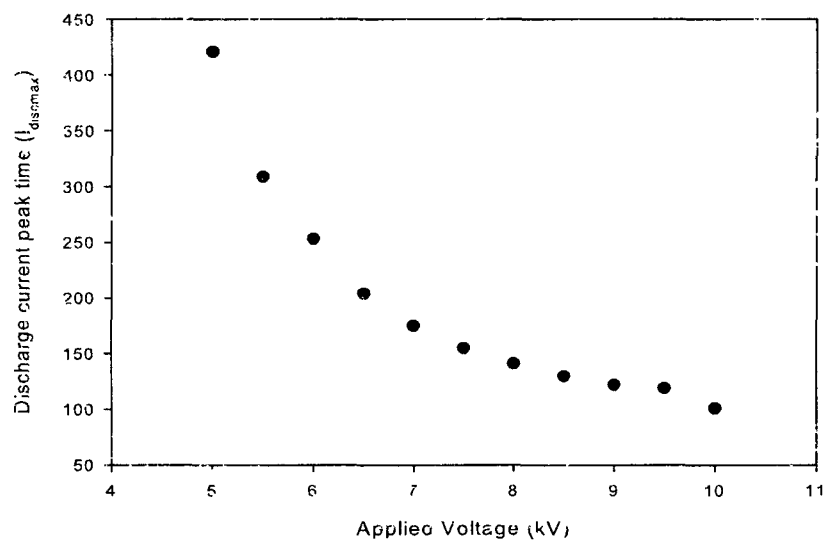


FIG. 14: Time of first peak as a function of applied voltage (pulse width:  $2 \mu\text{s}$ ; repetition Rate: 5 kHz; flow rate: 5.0 L/min).

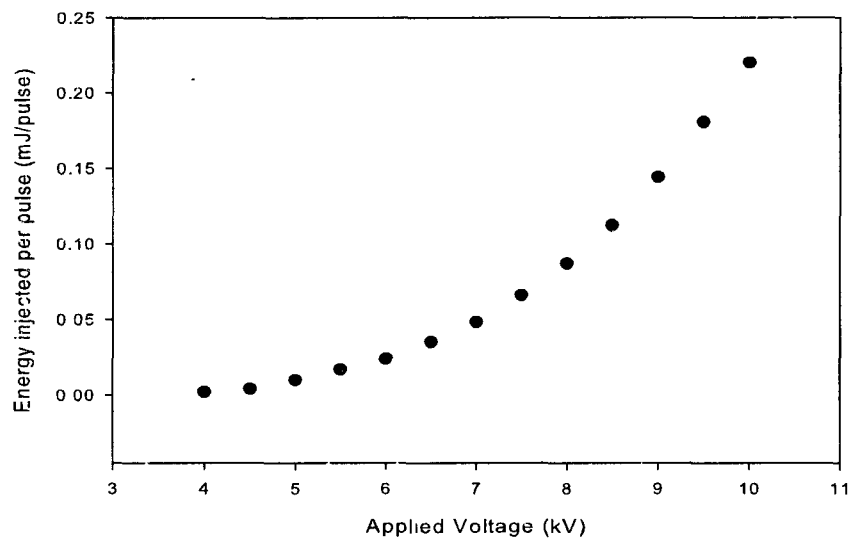


FIG. 15: The energy injected into the reactor per pulse (pulse width:  $2 \mu\text{s}$ ; repetition Rate: 5 kHz; flow rate: 5.0 L/min).

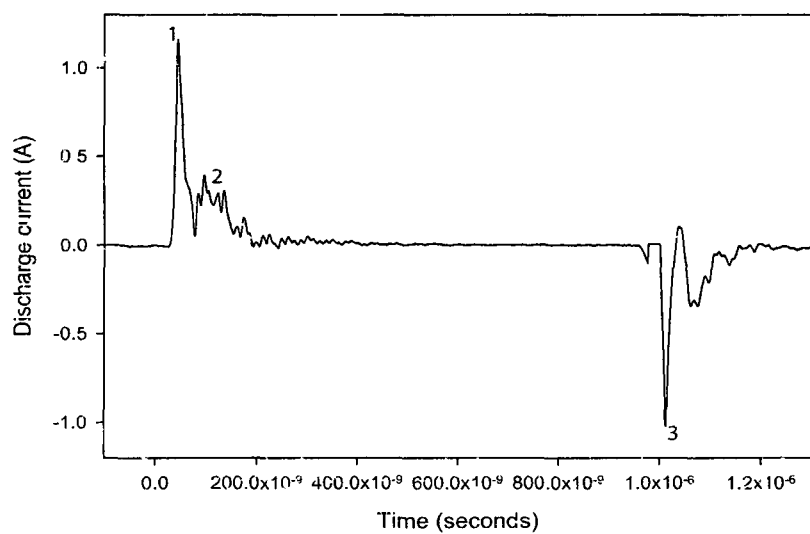


FIG. 16: The discharge waveform for the plasma pencil (applied voltage: 6 kV, pulse width:  $1 \mu\text{s}$ , repetition rate: 5 kHz; flow rate: 5.0 L/min).

### III.2 JET CURRENT MEASUREMENTS

The jet current waveform is obtained from a 4100 Pearson Electronics 1A/1V Rogowski coil. The hole diameter and lateral thickness of the Rogowski coil are 12.52 mm and 25.4 mm, respectively. Both high voltage probe and Rogowski coil outputs are connected to a 1 GHz Tektronix TDS 784D wideband digital oscilloscope. During experiments, the pulse width of the applied voltage is adjusted to 2  $\mu$ s, and the downside edge of the Rogowski coil is placed along the plasma jet at 0 mm (just after the reactor), 10 mm, 20 mm and 30 mm locations.

The APLTPJs are very sensitive to external effects. This causes difficulties for jet current measurements. Therefore, there is a need for a non-intrusive technique. In this manner, using the magnetic field induced by the plasma jet current is a practical diagnostics technique for jet current measurement. A Rogowski coil method, which has been used for more than a century, for high speed current pulse measurements is employed.

Since the APLTPJs are being operated by high voltage pulses, we need to deal with relatively high electromagnetic noise arising from the pulse generator and the reactor. For jet current measurements, the electromagnetic noise level is relatively high. Therefore, in order to eliminate this noise, the pulse generator is placed into a well-shielded Faraday cage. Unfortunately, the electromagnetic noise coming from the tube reactor still exists because the plasma jet passes through the Rogowski coil. This caused the time domain measurements to have relatively low resolution in this study.

Figure 17 shows the plasma plume current and the applied voltage pulse waveforms for different locations along the plasma plume/jet. The most interesting point in this figure is that the jet current waveform has a positive peak during the propagation of the plasma bullet, and a negative peak at the end of the applied voltage pulse. Both peaks include very important information about the dynamics of the plasma bullet. The positive current peak states that the electrons flow is towards the tube reactor. The evolution of the jet current peak is interpreted as follows: the plasma bullet first launches from the tube reactor and then goes through the lateral thickness (25.6 mm) of the Rogowski coil. Therefore as the ionization front of the plasma bullet passes through the Rogowski coil, the current peak starts increasing exponentially. When the plasma bullet is completely enveloped by the Rogowski coil, the jet current waveform experiences its highest point. Eventually, the plasma bullet

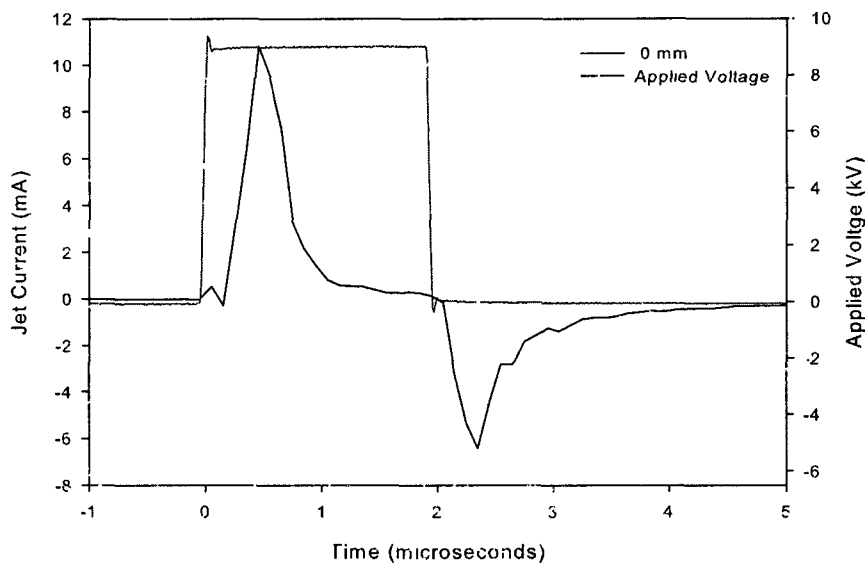


FIG. 17: The jet current measurements along the trajectory of the plasma bullets (applied voltage: 10 kV; pulse width:  $2 \mu\text{s}$ ; repetition rate: 5 kHz; flow rate: 5.0 L/min).

starts coming out from the Rogowski coil causing an exponential decrease.

A few hundred nanoseconds later after the applied voltage pulse ends, an opposing current “negative current”. is observed in Figure 17. This opposing current is created by the acceleration of the secondary discharge electrons towards the plasma bullet due to charge accumulated on the dielectric electrode surfaces established by the primary discharge. The detailed physical mechanism of this phenomena will be discussed in the next chapter.

### III.3 ARGON ADMIXTURE EFFECT ON THE DISCHARGE CURRENT

Argon admixture has an important role to play in enhancing plasma chemistry in applications. The effect of argon admixture on the plasma chemistry will be discussed in section V.1.3. As a summary of this section, small amount of argon admixture to helium flowing gas significantly enhances SPS line of  $N_2$  at 337 nm,  $OH(A-X)$  line

at 308 nm, and argon line at 750 nm while FNS line of  $N_2^+$  line at 391 nm, helium line at 706.5 nm, and oxygen line at 777.1 nm decrease.

Argon admixture does not change the shape of the discharge current waveform; however, it affects discharge current magnitude and its peak time. Figure 18 shows the argon admixture effect on the discharge current. Accordingly, 5% argon admixture little increases the current from 0.183 A to 0.203 A, and then the current value decreases to 0.063 A. At 40% argon admixture, the discharge current experiences a sudden increase, and then it keeps rising as argon admixture increases in the flowing gas.

Overall, the discharge current peak increases from 0.2 A to 0.5 A with argon admixture. In pure helium jet, an increase in discharge current leads to earlier the discharge current peak times (i.e. breakdown time) (Figure 14). However, in helium/argon mixtures, when argon admixture increases, the breakdown occurs later even though the discharge current values are higher.

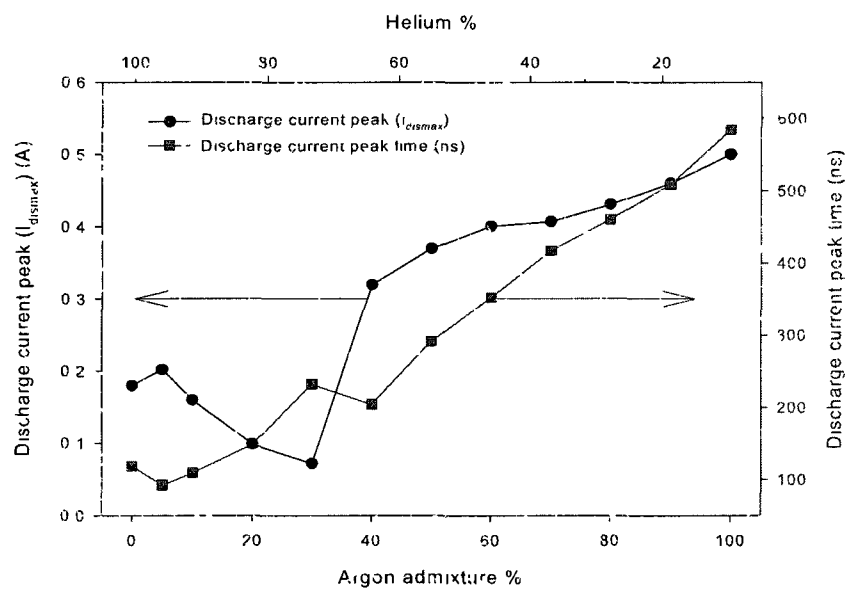


FIG. 18: Argon admixture effect on the discharge current and its peak time (applied voltage: 8 kV; pulse width: 2  $\mu$ s; repetition rate: 5 kHz; flow rate: 5.0 L/min).

### III.4 SUMMARY

Our low temperature plasma jets use dielectric electrodes and microsecond order HV pulses. These properties make them different than other regular discharges; especially, the secondary discharge ignition due to the charge accumulation on the electrodes during the main discharge is only found in these devices. The success in generation of such stable and cold plasmas in the open air originates from these properties. Basically, the dielectric electrodes control the current delivered between electrodes; therefore, the power applied to the jet remains at lower values. On the other hand, the presence of plasma is limited to the width of the pulse (a few microsecond order); hence, there is not enough time to heat up the gas temperature.

In this chapter, the characteristics of the current waveform were explained in detail for different HV values. The energy injected into the plasma jet per pulse was calculated for different high voltages. It was found that the maximum average power is 2.03 W for a HV amplitude of 10 kV (repetition rate: 10 kHz). It was noteworthy that the current waveforms of the tube reactor and plasma pencil are slightly different. In the plasma pencil, there is another peak just after the first discharge comes to an end. This point corresponds to the time the plasma bullet starts propagating in the ambient air.

The plasma bullet traveling in the surrounding air also delivers a current. This current was measured by a Rogowski coil. Difficulties regarding these jet current measurements were mentioned in the text.

Helium/argon mixture plasma jets are usually used to obtain chemically-rich plasmas in applications. Discharge current peak and breakdown time were given in section III.3. It was revealed that the discharge current becomes higher as the argon admixture gets higher. On the other hand, the breakdown occurs later with higher argon admixtures.



## CHAPTER IV

### DYNAMICS, FORMATION, AND PROPAGATION

In 2006, Laroussi and Lu proposed a photo-ionization based model [10] in order to explain the plasma bullet behavior. Their experimental results and explanations regarding the plasma bullet velocity and its propagation were in good agreement with that of the streamer theory. However, to date, a discussion always exists: Does the plasma bullet really behave like streamers? Streamers are usually unstable and inhomogeneous and have relatively thin structures but the APLTPJs consisting of plasma bullets do not share these characteristics. In this chapter, we seek to shed some light on these questions and issues.

#### IV.1 PLASMA BULLET DYNAMICS AND ITS FORMATION

The jet current measurements were presented in the previous chapter. These measurements (done by a Rogowski coil) offer great insight into the understanding of the APLTPJs dynamics. Figure 19 has two peaks, at the rising and falling edge of the HV pulse. The first peak has a positive polarity; therefore, it states that the electron flow is towards the tube reactor since the current and the electron flow directions are opposite. The second peak has a negative polarity, indicating that the secondary discharge, which is ignited because of the charge accumulation on the dielectric surface, plays a role at that time in time. In Figure 19, it is also observed that the magnitude of the jet current peak decreases as the Rogowski coil is moved further away along the plasma jet. It was noted in section III.2 that these jet current peaks quantitatively give insight into the electron number density inside the plasma bullet since ions are usually assumed to be immobile particles for atmospheric pressure low temperature plasmas. Figure 19 also shows that the electron number in a plasma bullet becomes less and less as it propagates forward. This is related to the power dissipation of the plasma bullet and the electron attachment to air molecules during its propagation at atmospheric pressure.

##### IV.1.1 Secondary discharge ignition

A few hundred nanoseconds after the applied voltage ends, an opposing current, "negative current", is observed (Figure 19). This opposing current is created by

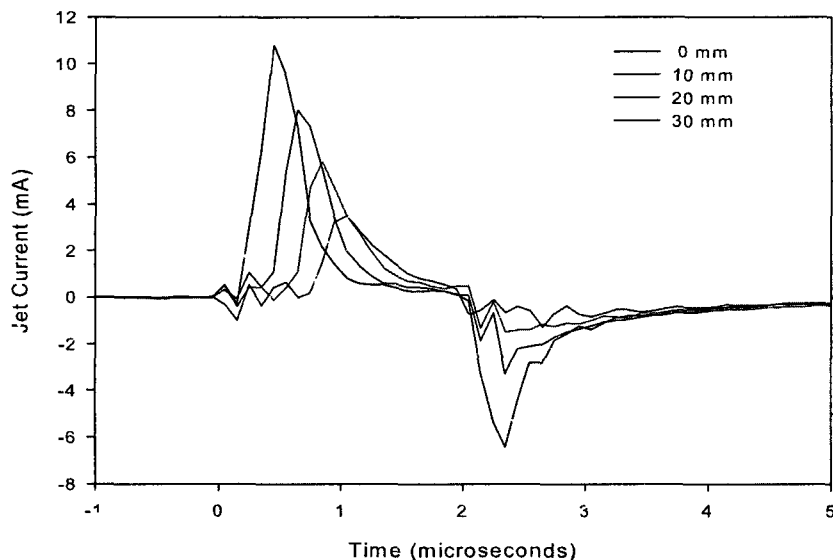


FIG 19: Jet current measurements as a function of the distance to the reactor.

the charge accumulation on the dielectric surface established by the main discharge on the dielectric electrode surface. This discharge, called the “secondary discharge” was previously reported by Laroussi et al. [37] in the case of pulsed DBDs. The most important point is that an effect of the secondary discharge ignition is clearly observed in the ionization channel even though it was previously believed that the effect of this secondary discharge effect are only confined between the electrodes. In order to make our interpretation more clear, the secondary discharge ignition is investigated by an ICCD camera. As seen in Figure 20, the secondary discharge is first ignited from the positive dielectric electrode and then creates propagation through the ionization channel. Based on these ICCD camera pictures, the charges accumulated on the positive dielectric electrode surface are mainly responsible for the secondary discharge ignition. No emission is observed from the ground dielectric electrode side (Figure 20). More importantly, the secondary discharge goes through the ground electrode. It is also worth noting that the plasma bullet propagation stops in an abrupt manner just after the secondary discharge ignition. The illustration of this interesting phenomenon will be given in the following section.

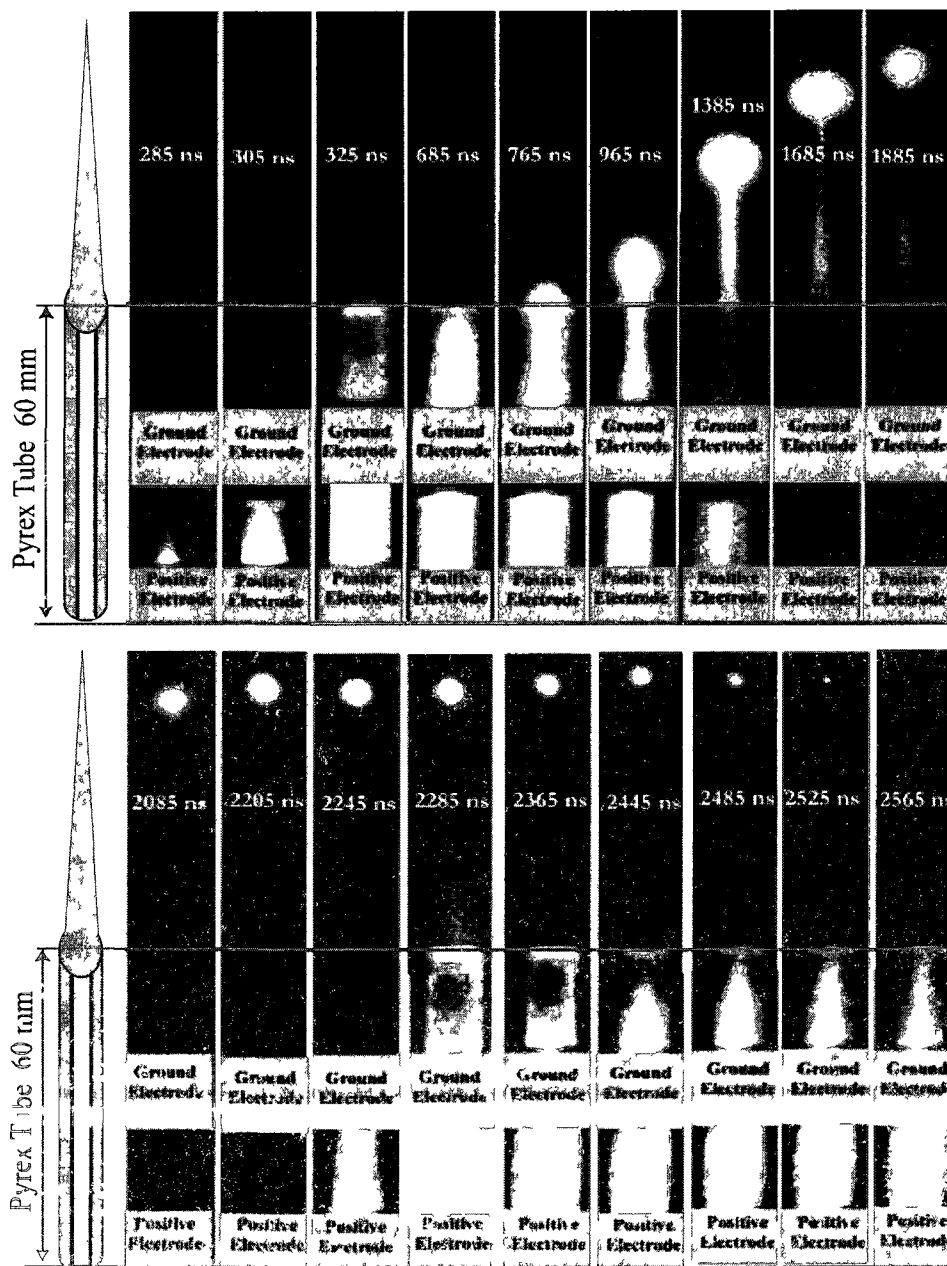


FIG. 20 ICCD camera photographs showing the secondary discharge arising from the positive electrode side when propagating along the ionization channel. After the secondary discharge ignition (2200 ns), the plasma bullet first slows down, and then no longer propagates further (2245 ns) (applied voltage 9 kV, pulse width 2  $\mu$ s, repetition rate 5 kHz, flow rate 5.0 L/min)

### IV.1.2 Electron density estimation in a plasma bullet

The electron density is estimated using Ohm's law from the jet current measurements. Based on Ohm's law, the current ( $I$ ) is equal to  $-nAve$ , where  $n$  is the density of charge carriers,  $A$  is the cross-sectional area,  $v$  is the drift velocity, and  $e$  is the electron charge. Since we assume that the ions are immobile,  $n$  represents the electron density. The highest peak of the jet current waveform ( $I_{max}$ ) is used for the electron density estimation. Therefore, the electron density calculated stands for the maximum electron density ( $n_{max}$ ) on the plasma bullet. The cross-sectional area of the jet is approximately determined based on the ICCD camera pictures. It is assumed that the drift velocity of the electrons is in the same order of magnitudes as the plasma bullet velocity. The plasma bullet velocity is measured along the plasma jet by means of a technique using the optical emission spectroscopy (Figure 21). The details of this new technique are discussed in Section IV.3. Therefore, the maximum electron number density ( $I_{max}$ ) is tabulated in Table 1 and is graphically shown in Figure 22.

TABLE 1: The maximum electron number density.

Position (mm)	$I_{max}$ (mA)	$A$ ( $m^{-2}$ )	$v$ (m/s)	$n_{max}$ ( $m^{-3}$ )
0	10.8	$3.85 \times 10^{-5}$	56278	$3.11 \times 10^{16}$
10	7.99	$3.42 \times 10^{-5}$	45146	$3.23 \times 10^{16}$
20	5.79	$3.02 \times 10^{-5}$	39780	$3.01 \times 10^{16}$
30	3.48	$2.65 \times 10^{-5}$	38299	$2.15 \times 10^{16}$

The magnitudes of the jet current and secondary discharge current peaks are measured as a function of the applied voltage in Figure 23 at 0 mm. These figures show that the magnitude of these peaks becomes larger as the higher voltages are applied to the electrodes. It is also noted that there is only a little difference between the order of magnitude of the jet current, related to the electron propagation, and the order magnitude of the secondary discharge current, caused by the charge accumulation during the applied voltage pulse.

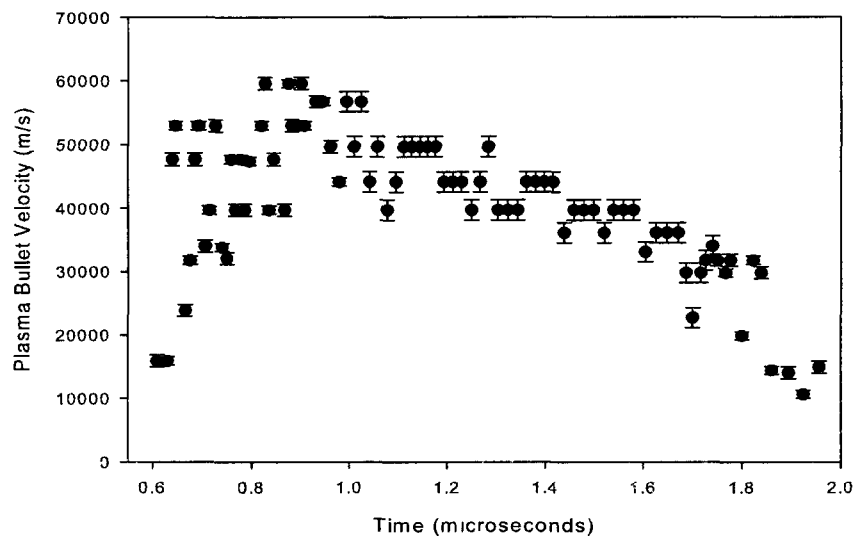


FIG. 21: The plasma bullet velocity during a high voltage pulse (applied voltage: 9 kV; pulse width:  $2 \mu\text{s}$ ; repetition rate: 5 kHz; flow rate: 5.0 L/min).

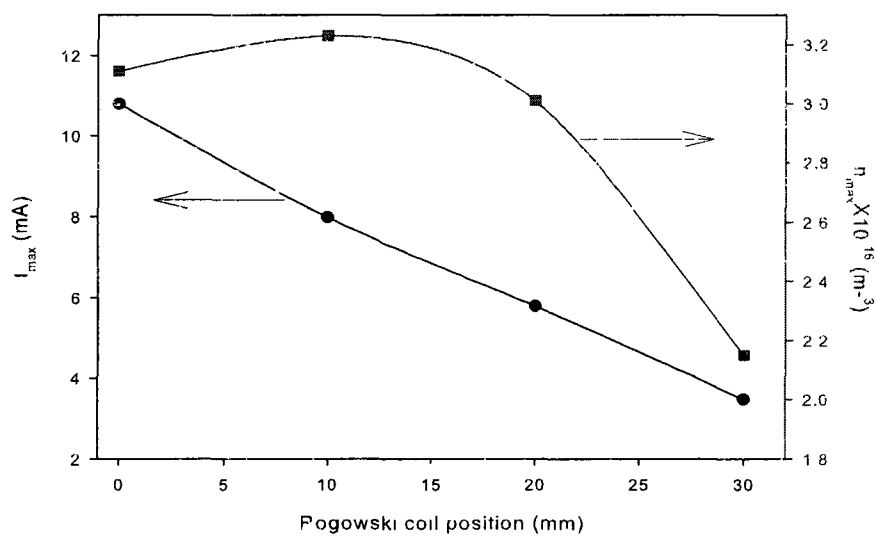


FIG. 22: The maximum electron density ( $I_{max}$ ) estimation along the plasma jet axis (applied voltage: 9 kV; pulse width:  $2 \mu\text{s}$ ; repetition rate: 5 kHz; flow rate: 5.0 L/min).

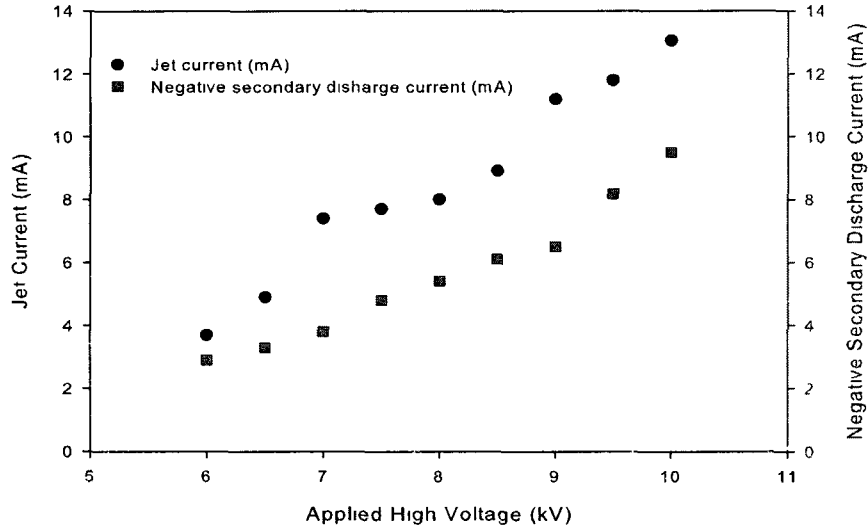


FIG. 23: The plasma bullet velocity during a high voltage pulse (applied voltage. 9 kV; pulse width: 2  $\mu$ s; repetition rate. 5 kHz; flow Rate: 5.0 L/min).

#### IV.1.3 Streamer theory for the plasma bullet propagation

In the 1930s and 1940s, early investigators made a great effort to explain the behaviors of the streamers after the initial theory of the spark mechanism at low pressures was established by Townsend [38, 39, 40, 41, 42, 43, 44]. Basically, they showed that photo-ionization plays a key role in streamer formation and its propagation [45, 46, 47].

The positive jet current peak of Figure 19 can be explained using the cathode-directed streamer mechanism. This positive peak states that the electron flow is towards the anode as the direction of the bullet propagation is opposite, similar to the streamer theory.

The voltage applied between the electrodes initiates an electron avalanche as follows: a single electron creates  $\alpha$  new electrons and positive ions in the direction of the field. The increase in the number of the ions ( $dn$ ) caused by  $n$  electrons in a distance  $dx$  is expressed by

$$dn = \alpha n dx. \quad (1)$$

Let Eq. 1 from  $n = n_0$  at  $x = 0$  to  $n = n$  at  $x = x$ ,

$$\int_{n_0}^n \frac{dn}{n} = \alpha \int_0^x dx \quad (2)$$

$$\ln \frac{n}{n_0} = \alpha x \Rightarrow n = n_0 e^{\alpha x} \quad (3)$$

where  $\alpha$  is called the first Townsend coefficient, which stands for the number of new electrons and ions created by a single electron per centimeter.

After enough space charges are developed by the avalanche itself, the avalanche goes into the streamer phase. During this process, the avalanche produces excited atoms (or molecules) and ions. Some of these excited atoms or molecules emit short ultraviolet (UV) radiation. This short UV radiation is highly absorbed by helium (or argon) atoms and air molecules. Such photons were observed by several researchers as early as the 1930s [44, 48]. In 1965, Dawson and Winn [49] developed a model for the streamer propagation: the photon emission from the streamer head creates photoelectrons at a suitable distance (ionization front). These photoelectrons form an avalanche towards the streamer head under the influence of the electric field. A new streamer head will be formed during this avalanche acceleration. Therefore, the streamer propagates ahead in discrete steps not continuously. It is worth noting that the streamer velocity is limited to the drift velocity of the electrons [49].

In the Dawson and Winn's model, each discrete step is considered as a sphere with a diameter ( $r_0$ ) having  $n_0$  positive ions. Based on their approximation, a single electron at a distance  $r_1$  is accelerated towards the sphere. This acceleration creates a new avalanche from  $r_1$  to  $r_2$  (Figure 24). The avalanche multiplication from  $r_1$  to  $r_2$  is given by

$$n = \exp \int_{r_2}^{r_1} \alpha dr + n^m \quad (4)$$

where  $\alpha$  is a Townsend ionization coefficient, and  $n^m$  represents the electron production due to the Penning Ionization mechanism:  $He^m + N_2 \Rightarrow N_2^+ + He + e$ . The diffusion radius (sphere radius) of the avalanche is also given by

$$r_0 = \left( 6 \int_{r_2}^{r_1} \frac{D}{v_d} \right)^{1/2} \quad (5)$$

where  $D$  is the diffusion coefficient, and  $v_d$  is the drift velocity. The following three conditions need to be satisfied [49]:

- The number of the ions inside the new sphere ( $n_1$ ) created by the electron avalanche is equal to the number of the ions inside the original sphere ( $n_0$ ).

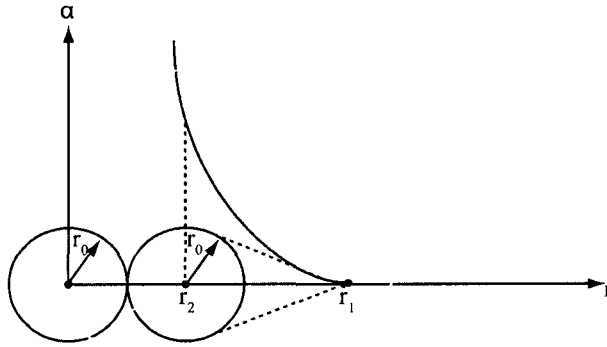


FIG. 24: A single electron is accelerated towards the original sphere [49].

- The diffusion radius of the avalanche cannot be larger than the radius of the original sphere,
- The avalanche should reach enough multiplication before the original sphere and new created sphere begin to overlap ( $2r_0 \leq r_2$ ).

The plasma bullet formation and its propagation mechanism, which was adopted from the streamer theory by Lu and Laroussi [10], is sketched in Figure 25. As in streamers, the accelerated space charges create an avalanche just after the high voltage is applied to the dielectric-covered electrodes (Figure 25 a). After a certain point, the avalanche itself goes into the plasma bullet formation (streamer) phase (Figure 25.b and 25.c). First, the electrons are accelerated towards the positive ions, and then the photons are emitted (Figure 25.b) (i.e. an electron avalanche occurs). These photons produce new photoelectrons and positive ions at a suitable distance; therefore, the plasma bullet's ionization front starts propagating with the successful completion of the events (Figure 25.c). As the plasma bullet travels to further distances, it leaves behind an ionization channel consisting of the short-lived and long-lived species (Figure 25.d). A secondary discharge is ignited at the end of the applied voltage pulse. This newly formed discharge interrupts the plasma bullet propagation in an abrupt manner. As shown in the previous section (Figure 19), an opposing jet current, "negative current" occurs at the end of the applied voltage pulse. This is due to the acceleration of the secondary discharge electrons towards the plasma bullet by the electric field established by the charges accumulated on



the dielectric surface. The phenomenon of the plasma bullet inhibition is illustrated in Figure 25.e. Accordingly, the motion of the electrons constitute a current that counters a negative current. This opposing motion of electrons cancels out positive charges of the plasma bullet. Therefore, the electric field between photo-electrons and the head of the plasma bullet becomes almost zero; thus, no more avalanche occurs. Henceforth, the plasma bullet stops propagating further.

#### IV.1.4 Similarities between the streamers and the plasma bullets

The streamer theory explanation for the plasma bullet formation and its propagation is experimentally tested under different conditions. The plasma bullets travel further as in cathode-directed streamers (CDS) when the applied voltage polarization is positive. In order to enhance our confidence regarding similarities between the plasma bullets and the streamers we applied a negative high voltage to the electrodes. It turns out that the plasma bullets behave like anode-directed streamers (ADS) (Figure 26). In the ADSs, the electrons flow is in the same direction as the propagation; therefore, the streamer current (i.e. jet current) has a negative peak (Figure 26). The opposing current due to charge accumulation on the dielectric surface still exists at the end of the applied voltage, and it has a positive peak (Figure 26)

Not only does the jet current waveform show some similarities with the ADS but also the physical dynamics of the plasma bullets are similar to that of the ADSs. An ICCD camera is used to analyze the plasma bullet dynamics during its propagation (Figure 27). In the case of the negative applied voltage, it is observed that the plasma bullet starts forming from the negative electrode side and travels much slower (approximately around 500 m/s for negative 9 kV the applied voltage). In addition, the luminosity of the plasma bullet is dimmer. Similar dynamics are also reported for the anode-directed streamer discharges in Ref. [50, 51].

Another interesting phenomenon of the plasma bullet with the negative voltage polarization is that the secondary discharge ignited by charge accumulation at the end of applied voltage is not visible by the ICCD camera. However, it is already known that a secondary discharge exists for the negative applied voltage as shown in the positive peak (opposing current) of the jet current (Figure 26). This states that the charge accumulation mostly includes positive ions; therefore, they cannot propagate further due to highly collisional medium of atmospheric pressure. In addition, this secondary discharge ignition does not interrupt the plasma bullet propagation (Figure

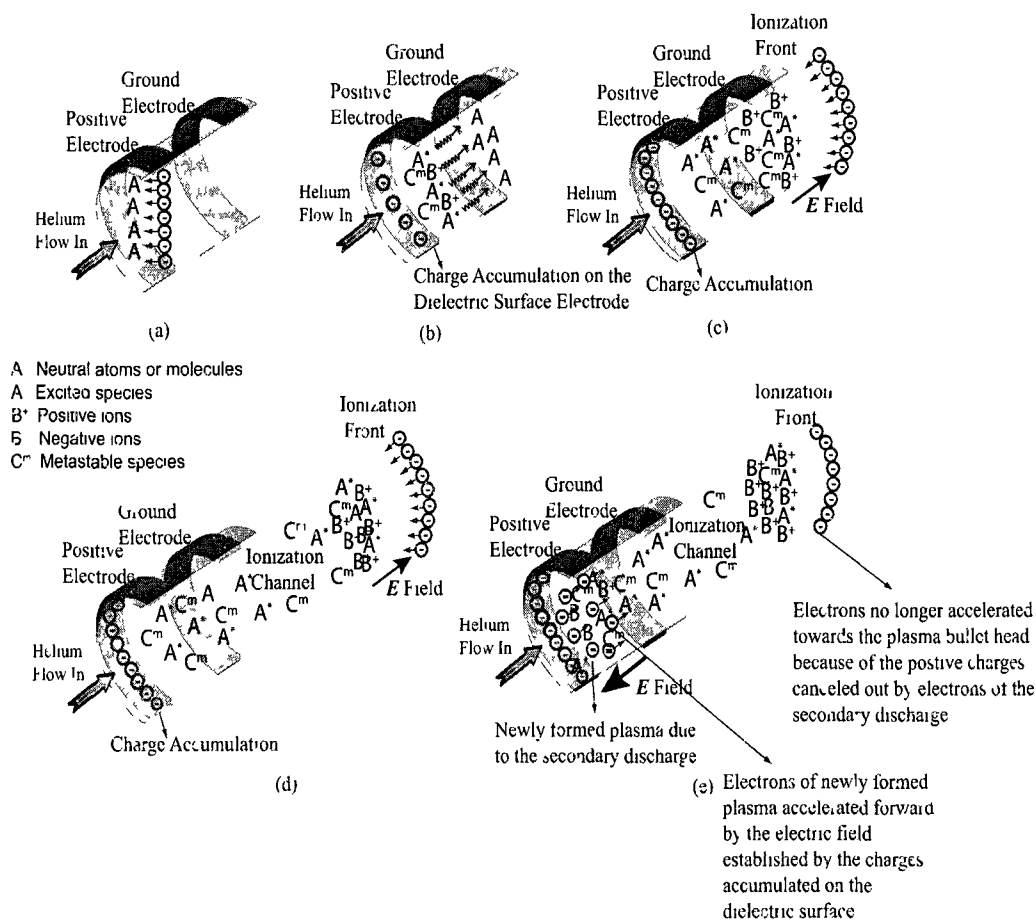


FIG. 25: Plasma bullet formation processes. (a) Ignition of discharge inside chamber by the electron avalanche, (b) photons are emitted from positively charged plasma, and then photo-ionization occurs at a suitable distance, (c) plasma bullet is formed by the acceleration of photo-electrons towards the positively charged plasma head (an electron avalanche occurs). (d) as the plasma bullet propagates further with the normal succession of the events, it leaves behind an ionization channel consisting of excited states and metastables, (e) while the applied voltage pulse is decreasing to zero, the secondary discharge is ignited due to the charges accumulated on the dielectric electrode. The electrons of this secondary discharge are accelerated towards the head of positively charged bullet by the electric field established by the charges accumulated on the dielectric surface. The motion of the electrons constitutes a current that counters a negative current. This opposing motion of electrons cancels out positive charges of the plasma bullet. Therefore, the electric field between photo-electrons and the head of the plasma bullet becomes almost zero, thus, no more avalanche occurs. Henceforth, the plasma bullet stops propagating further.

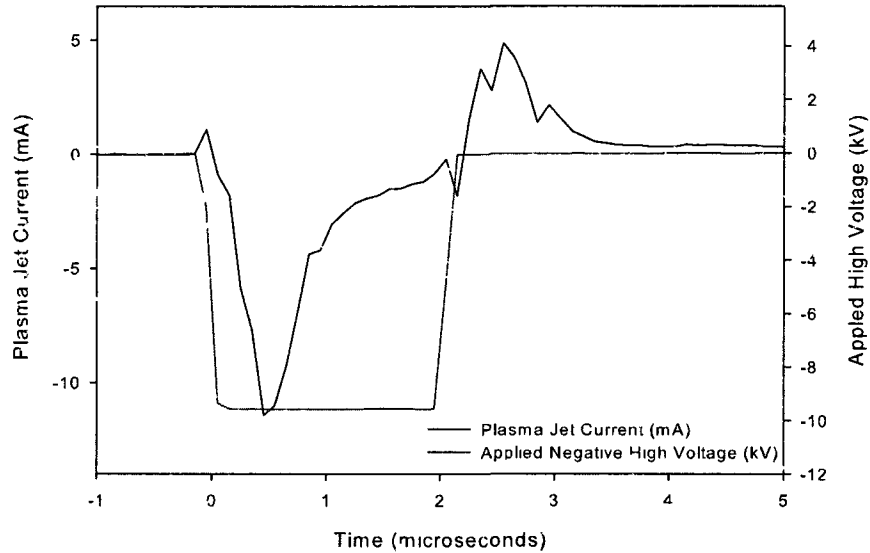


FIG. 26: Negative applied voltage and the measured plasma jet current by Rogowski coil. The current is negative as in the anode-directed streamers.

27) (i.e. the plasma bullet keeps travelling after the secondary discharge is ignited at the falling edge of the negative applied voltage).

In Ref. [51], an empirical formula is reported between the streamer velocity and the streamer head diameter:  $v = 0.5d^2 \text{ mm}^{-1}.\text{ns}^{-1}$ . We found a similar relationship for the plasma bullets. The average plasma bullet velocity is first measured for different positive applied voltages by means of optical emission spectroscopy (OES). The experimental procedure for the measuring average plasma bullet velocity ( $v_b$ ) is detailed in the section IV.3. We used the plasma bullet area ( $A$ ) instead of the diameter in our empirical formula since the plasma bullet is not perfectly circular during its propagation. The measuring procedure of the plasma bullet area is as follows: the picture of the plasma bullet is consecutively taken by the ICCD camera for every 40 seconds, and then from the beginning to the end of its propagation the plasma bullet area is averaged for each applied voltage. As seen in Table 2, the plasma bullets also exhibit a similar relationship for different applied voltages:  $v_b = 1.46A \text{ m}.\text{ns}^{-1}$ . For less than 8 kV applied voltages (where the plasma bullet

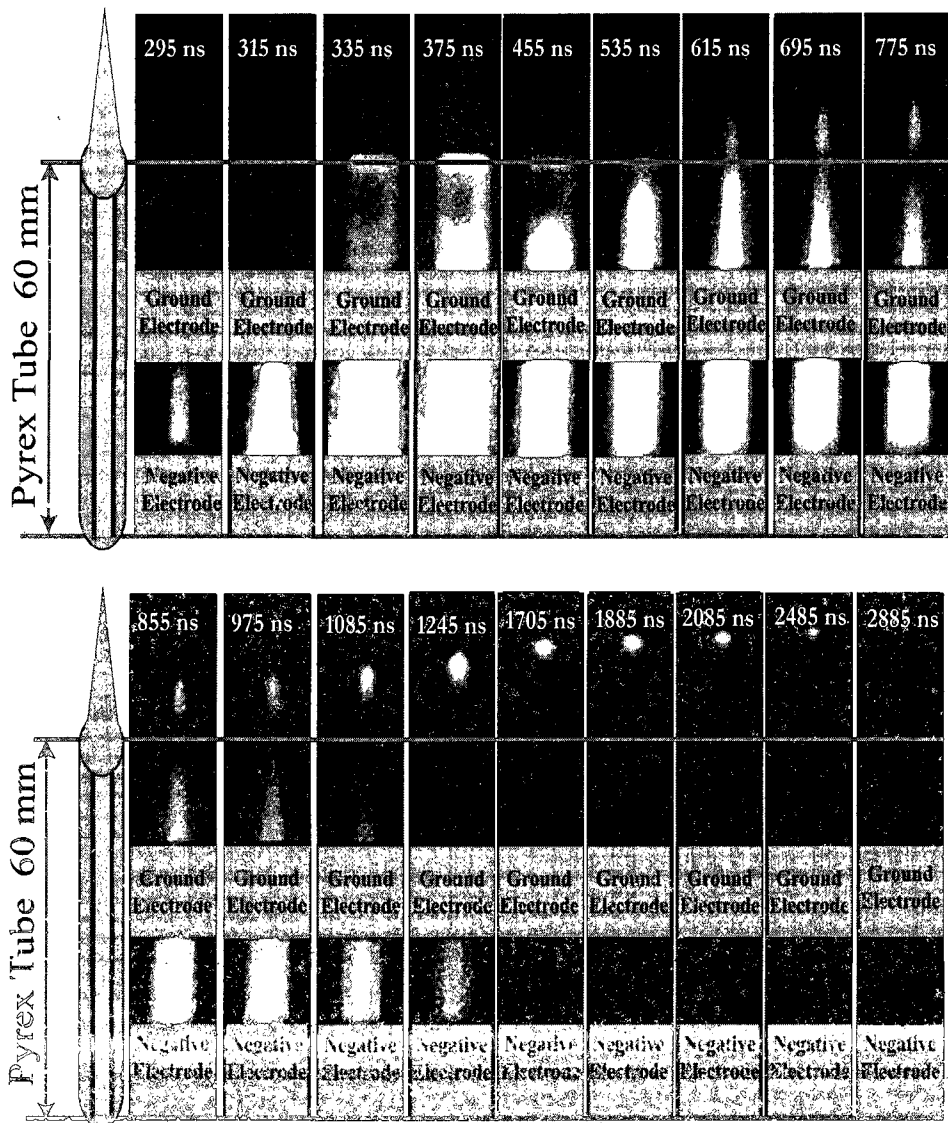


FIG. 27: The plasma bullet propagation in the case of the negative applied voltage (applied voltage: -9 kV; pulse width: 2000 us; repetition rate: 5 kHz; flow rate: 5.0 L/min).

only propagates a few millimeters long), this empirical formula is invalid.

TABLE 2: The empirical formula calculation between the plasma bullet velocity and the plasma bullet area for different applied voltages.

Applied Voltage (mm)	$v_b$ (m/s)	$A \times 10^{+5}$ ( $m^2$ )	$C \times 10^{-9}$ ( $m^{-1}s^{-1}$ )
8	25385.01	1.75	1.45
8.25	28236.89	1.94	1.45
8.5	31089.39	2.15	1.45
8.75	33177.28	2.26	1.47
9.0	34819.5	2.37	1.47
9.25	36089.31	2.44	1.48
9.5	37739.49	2.59	1.46
9.75	39041.33	2.68	1.46
10.00	39939.75	2.71	1.47

#### IV.1.5 Observation of the plasma bullet early formation

The formation process of the plasma bullets will be discussed in this section. The APLIPJs usually use dielectric-covered plate-shaped electrodes. However, the streamer discharges are usually formed around the sharp needle or thin wire electrode configurations using metal materials. This dissimilarity especially makes the observation of early discharge formation noteworthy.

For the purpose of the early stage observation, the ICCD camera is placed onto the head-on and side-on positions of the tube reactor (Figure 28). The ICCD camera, the high voltage probe, and the current probe are fully optimized to determine the exact timing of the discharge. The exposure time of the ICCD camera is adjusted to 3 ns. As shown in Figure 29.b, a discharge homogeneously starts forming inside the reactor at around 20 ns after the high voltage applied. At around 40 ns, the electron avalanche created by the seed charges becomes more visible, and spreads out from the central point of the reactor to the interior surface of the dielectric tube (blue color). In this time period, the discharge current is still very low (i.e. no breakdown occurs yet). It is important to note that in Figure 29 colors represent the magnitude of the photon emission from the reactor (black: the weakest emission, white: the strongest emission). In addition, the photon emission in each picture is averaged the wavelength range of 200 ns to 900 ns (the photo-diode material of our ICCD camera can almost uniformly track emissions for this wavelength range). Figure 29 shows that the plasma goes from one dominant phase into another dominant phase every 20

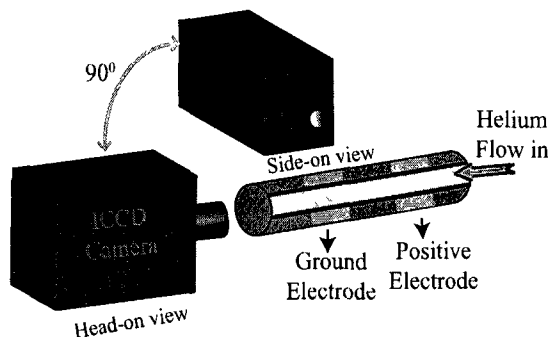


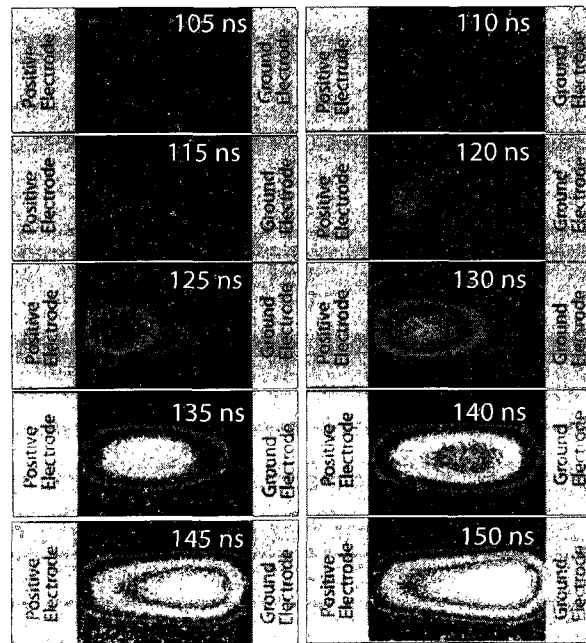
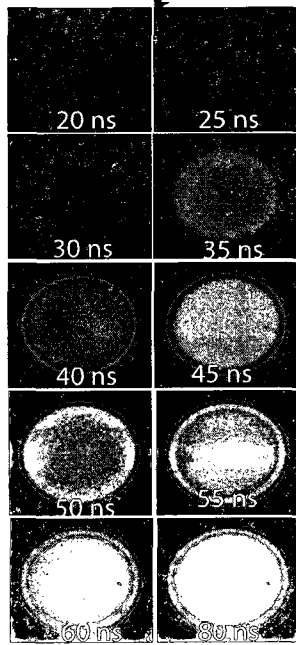
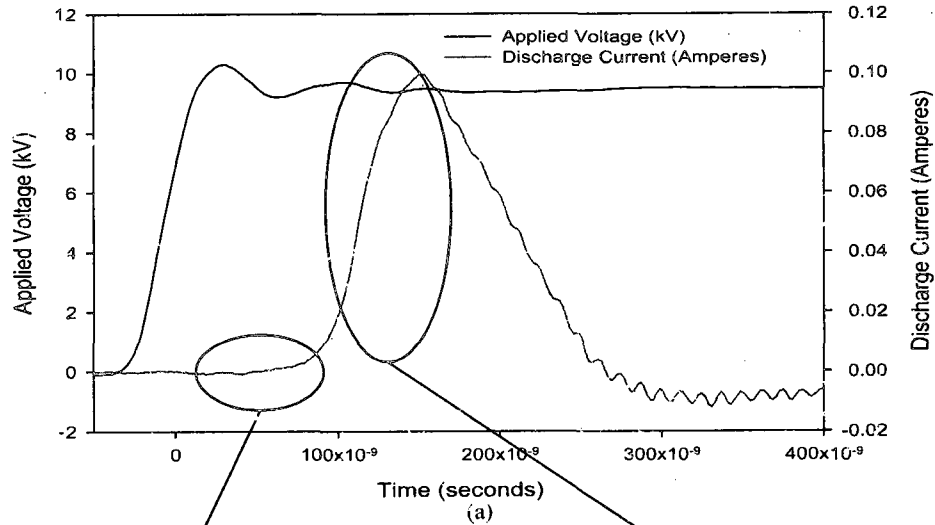
FIG. 28. Experimental setup for the head-on and side-on view ICCD pictures.

ns (for instance, blue color to the green color). A dark blue region, which represents the plasma sheath due to the voltage drop on the dielectric surface, exists around the core discharge for each picture.

In summary, Figure 29 provides understanding of two important points regarding the plasma bullet formation at the early stage of the discharge:

- The plasma bullet is initially created at the center region of the tube reactor,
- A sheath region clearly exists due to voltage drop established by the charge accumulation on the dielectric surface during at all times

The head-on view pictures are controlled by side-on view pictures to make sure that the discharge is still inside the wrapped positive electrode during the early stage. As seen in Figure 29.c, the plasma bullet has not been formed and not started propagating yet at the early stage. Around 100 ns, the plasma bullet starts propagating between the positive and ground electrodes. 100 ns corresponds to the point that the discharge current begins rising. When the plasma bullet reaches the ground electrode around 150 ns, the discharge current experiences the highest peak. The interpretation of the emission intensity for the side-on view pictures is not as easy as that for the head-on view pictures because the emission in the radial-direction of the tube reactor is not uniform. However, it still can be observed from the central point of the reactor that the formation of the plasma bullet develops from the center to the interior side of the tube reactor (Figure 29.c).



(b)

(c)

FIG. 29: The early formation of the plasma bullet: a) applied voltage and discharge current waveforms at the early beginning of the discharge; b) head-on view: early formation inside the wrapped positive electrode (i.e. no propagation started yet); c) side-on view: plasma bullet formation between two electrodes.

In the case of the negative applied voltage, every phase of the early formation of the plasma bullet is similar to that of the positive applied voltage but the formation process is much slower as in its propagation. The seed charges are able to produce enough avalanches at around 140 ns (Figure 30).

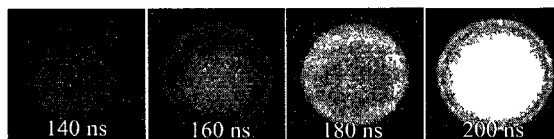


FIG. 30: The plasma bullet early formation generated by a negative applied voltage pulse.

There is another interesting observation for the negative applied voltage. In the case of the positive applied voltage, the avalanche keeps growing gradually. However, for the negative applied voltage, the discharge collapses towards its center for about 1 ns, and then keeps developing for the next 10 ns (Figure 31). This mechanism repeats for every 10 ns. This is probably due to different mechanism of the anode-directed streamers. However, it still needs further investigation.

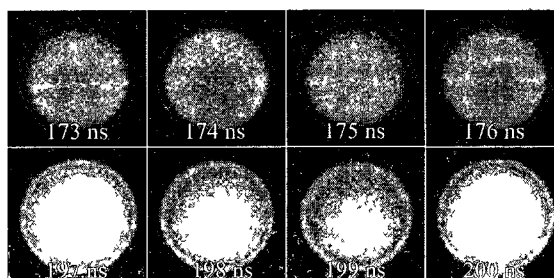


FIG. 31: The plasma bullet collapsing toward its center for only 1 ns in every 10 ns in the case of a negative applied voltage pulse.

#### IV.1.6 Photo-ionization vs. helium metastables

In spite of several findings regarding similarities between the plasma bullets and streamers, there are important questions that still need to be answered: which reactions supply the energetic photons for the photo-ionization process? What is the role of the helium metastables for the plasma bullet propagation?



In streamers, early investigators [52, 53, 54] showed that  $O_2$  molecules emit the extreme ultraviolet radiation that is short enough to ionize the molecules. Accordingly, the electrons dissociate in a single collision the molecules into atoms, excited atoms, or ions:  $O_2 + e = O + O^* + e + h\nu$ , or  $O_2 + e = O + O^+ + 2e + h\nu$ .

Plasma bullets exhibit little different behavior due to the contribution of helium metastables to the plasma bullet propagation. The important role of the helium metastables has been previously discussed [55, 56, 57]; the ionization wave only propagates along the helium channel. It is worth noting that a helium atom has two metastable levels at 19.5 eV and 21.6 eV; therefore, radiations of energies in excess of 5 eV will cause the ionization of helium atom (ionization potential of helium is 24.5 eV). Moreover, these metastables will interact with air molecules (Penning Ionization) and then produce excited nitrogen molecules, nitrogen ions and penning electrons.

On the other hand, the role of air molecules for the photo-ionization process in the plasma bullets is still as important as that of streamers since the plasma bullet propagates in the surrounding air. However, a discharge still occurs inside the reactor when only helium flow is present. One important remark here is that the helium gas has industrial grade purity during our experiments, and a small amount of air always leaks from our connectors. Another point is that helium atom also may emit short UV radiation [58, 59]. These photons also may help photo-ionization process inside the reactor. However, further investigations are needed to figure out which are reactions associated with the short UV photon production by helium atoms.

## IV.2 PLASMA BULLET PROPAGATION AND ITS INHIBITION

The main aim of this section is to determine the plasma bullet lifetime as a function of different operating conditions\*. Note that the plasma bullet lifetime is related to the plasma jet length since the plasma jet is the footprint of the plasma bullets (i.e. if the plasma bullet travels to further distances, the plasma jet appears longer). In this section, the plasma pencil is used as an APLTPJ reactor.

The plasma bullet lifetime depends on the helium mole fraction along the propagation path, the magnitude of the applied voltage, and the secondary discharge ignition time. In dielectric barrier discharge (DBD) sources that are driven by short high voltage pulses, Laroussi et al [37] showed that in addition to the main discharge

---

\*This section was published in *J. Appl Phys* Vol. 108, p. 063305 2010.

a secondary discharge is self-ignited during the fall-time of the applied high voltage pulse. The secondary discharge occurs at the end of the applied high voltage pulse due to the charge accumulation established by the primary main discharge on the surface of the dielectric [37].

For a pulse width less than a certain value, the plasma bullet stops propagating just after the secondary discharge ignition. The reason for this interesting phenomenon was already investigated earlier. The ionization channel contains short-lived, such as  $He^*$ ,  $N_2^*$ ,  $N_2^+$ , and long-lived, such as  $He^m$  (helium metastables),  $O_3$ ,  $NO$ ,  $NO_2$ , reactive species. The zones, where the propagation of the plasma bullet is inhibited by low helium mole fraction or secondary discharge ignition, are shown in Figure 32. If the pulse width is long enough, the plasma bullet propagation is inhibited before the ignition of the secondary discharge due to quenching by air molecules (mostly by oxygen) diffusing into the ionization channel. This limit is called the transition point that separates the plasma bullet inhibition zones (the secondary discharge ignition zone from low helium mole fraction zone) as seen in Figure 32. This transition point shifts as a function of the applied voltage from 1300 ns to 425 ns (Figure 33) since the plasma bullet is able to arrive to this transition point earlier at higher applied voltages due to its higher velocity.

This transition point is important for the optimum operating conditions of the plasma pencil. How the plasma bullet comes to an end affects the structure of the tip of the plasma plume. If the secondary discharge ignition inhibits the propagation of the plasma bullet, the plasma plume tip is shaped as a sharp and homogenous structure. In contrast, in the case of low helium mole fraction, the plasma jet tip seems inhomogeneous and is unstable. In applications such as material processing or biomedicine, the condition of the tip of the plasma plume is very important since it is the part that comes in contact first with the surface under treatment.

#### IV.2.1 Correlation between helium mole fraction and plasma bullet propagation<sup>†</sup>

A helium flow dynamics simulation is performed along the propagation region of the plasma bullet to determine the minimum helium mole fraction value necessary to sustain its propagation<sup>†</sup>. The plasma bullet launches from a plasma jet device called the 'Plasma Pencil' driven by unipolar square nanosecond high voltage pulses, and

---

<sup>†</sup>This subsection was published in *J. Phys. D: Appl. Phys.*, Vol. 43, p. 155202, 2010

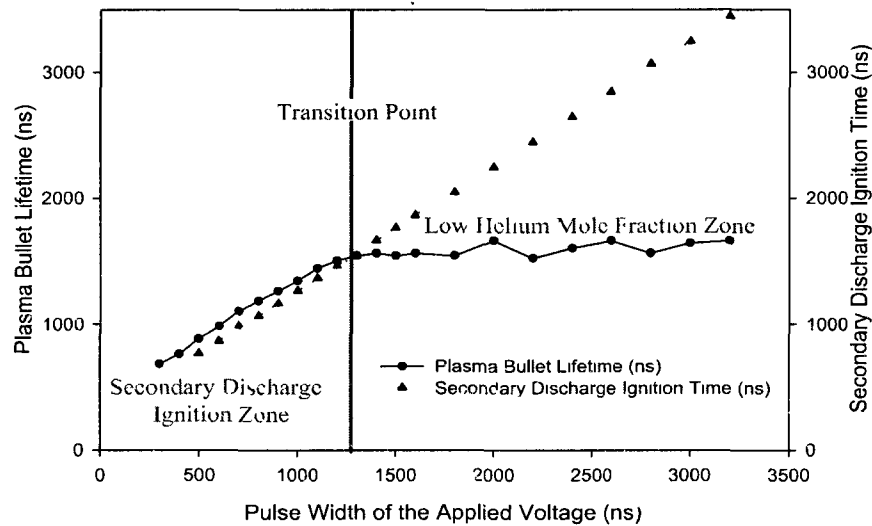


FIG. 32: Plasma bullet lifetime as a function of the pulse width (applied voltage: 4 kV; repetition rate: 5 kHz; flow rate: 5.0 L/min).

propagates in the surrounding air. During its propagation, air molecules diffuse into the path/helium channel of the plasma bullet. It is found that if the ratio of air molecules to helium atoms exceeds a certain limit, the plasma bullet propagation is inhibited. In this study, the helium mole fraction limits are estimated for different operating conditions of the plasma pencil.

Ionization and attachment processes dominate the formation of the plasma bullets. Since the plasma bullet travels in the air, electron attachment by oxygen molecules plays a key role. The Townsend first ionization coefficient  $\alpha$  must be larger than the attachment coefficient  $\beta$  [7]; therefore, the electron avalanche (initiated by photoionization) leads to the formation of the plasma bullet and its propagation. The electron number density  $n_e$ , based on the Townsend coefficients  $\alpha$  and  $\beta$  along the x-axis can be given by

$$\frac{dn_e}{dx} = (\alpha - \beta)n_e \implies n_e(x) = n_{e0} \exp[(\alpha - \beta)x] \quad (6)$$

where  $n_{e0}$  is the number of primary electrons. If the plasma bullet propagation

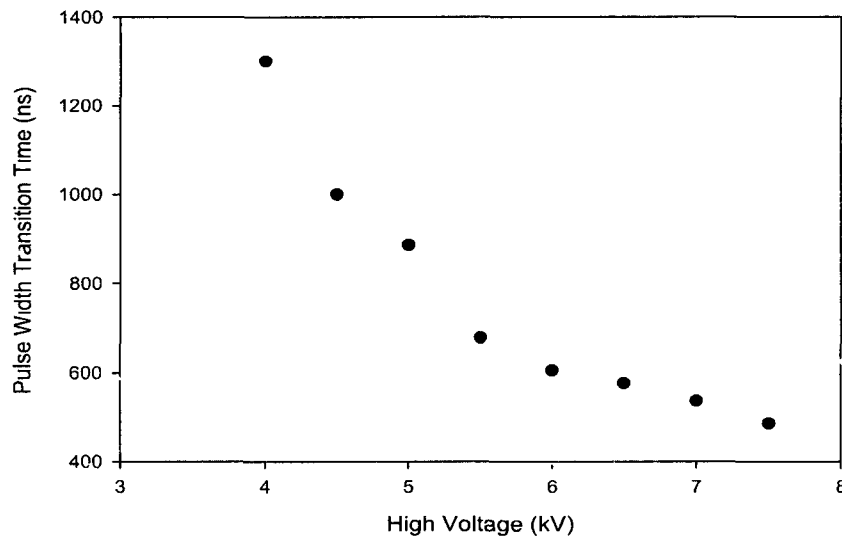


FIG. 33: The pulse width transition time as a function of the applied voltage (repetition rate: 5 kHz; flow rate: 5.0 L/min).

starts due to primary electrons. the number of positive and negative ions in the plasma bullet can be found by

$$\frac{dn_+}{dx} = \alpha n_e \implies n_+(x) = \frac{\alpha}{\alpha - \beta} (n_e - 1) \quad (7)$$

$$\frac{dn_-}{dx} = \beta n_e \implies n_-(x) = \frac{\beta}{\alpha - \beta} (n_e - 1) \quad (8)$$

where  $n_e = \exp[(\alpha - \beta)x]$  is the number of electrons in the plasma bullet. In order to maintain this ionization process, in addition to energy, the propagation channel should always be fed by a new volume of helium gas.

Although the main excited species are  $N_2^*$  and  $N_2^+$  due to the surrounding air diffusing into the plasma bullets [26], helium atoms play a key role in initiating many chemical reactions inside the plasma jet. Helium atomic lines are observed at 501.6 nm ( $3^1P \rightarrow 2^1S$ ), 587.6 nm ( $3^3D \rightarrow 2^3P$ ), 667.8 nm ( $3^1D \rightarrow 2^1P$ ), 706.5 nm ( $3^3S \rightarrow 2^3P$ ), and 728.1 nm ( $3^1S \rightarrow 2^1P$ ) in the visible-infrared regions of the spectra. A helium atom naturally has 2 metastable levels, the  $2^1S$  (singlet) and  $2^3S$  (triplet). In our plasma jet,  $3^1P \rightarrow 2^1S$  at 501.6 nm is an important transition

populating electrons to the singlet metastable level of helium atom. This helium metastable ( $He^*$ ) is especially noteworthy because recent experimental results [56] and theoretical calculations [57] indicate that the helium metastables mainly sustain the plasma bullet propagation by Penning ionization mechanism as shown in Table 3.

TABLE 3: Penning ionization mechanism

Reactions
$He + e \rightarrow He^*(excited) + e$ (excitation)
$He + e \rightarrow He^*(metastable) + e$ (excitation)
$He^* + N_2 \rightarrow N_2 + He + e$ (Penning Ionization)

According to these processes, the electron avalanche causes excited and metastable level helium atoms by colliding with the background helium gas. Hence, the helium metastables excite  $N_2$  in the air, and produce  $N_2^*$  and  $N_2^+$  by Penning ionization mechanism. In this manner, the role of the helium mole fraction becomes important along the plasma bullet propagation path. A new volume of helium gas is necessary to maintain the above reactions. This important role of helium flow during the plasma bullet propagation is also verified by optical emission spectroscopy and intensified CCD (ICCD) camera observations. Due to the important contribution of the helium metastables to the propagation of the plasma bullets, the helium transition of ( $3^1P \rightarrow 2^1S$ ) at 501.6 nm is investigated at 20 mm away from the cathode for different helium exit velocities. As shown in Figure 34, the intensity of 501.6 nm helium atomic line increases as the helium exit velocity increases. The slope of this increase is almost the same as the slope of the increase of the length of the plasma jet. It is also noted that the behaviors of the other helium emissions are also similar to the 501.6 nm helium line. This observation proves that the helium mole fraction (i.e. amount of helium atoms) along the plasma bullet propagation path is directly related to the existence of the plasma jet (i.e. the propagation of the plasma bullet).

Our second observation indicates that the plasma bullet is only able to propagate where the helium mole fraction is more than a certain limit. If the plasma pencil is horizontally positioned and the helium exit velocity is adjusted to as low as 3 m/s the buoyancy force becomes easily visible. As seen in Figure 35, the plasma bullet follows the trajectory of the helium flow. This clearly shows that the plasma bullet only propagates where the helium mole fraction is high enough to sustain the above reactions.

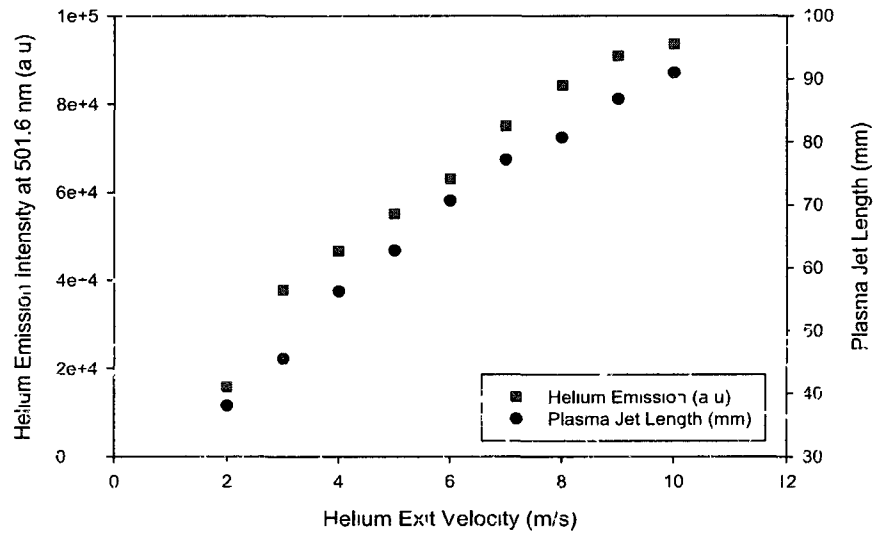


FIG. 34. Helium emission intensity at 501.6 nm and plasma jet length versus helium exit velocity.

In this study, the characterization of the helium mole fraction along the plasma bullet propagation path (i.e. streamer or ionization channel) is determined for different applied high voltages (from 5 kV to 7 kV) and gas flow velocities (from 3 m/s to 10 m/s) with a constant pulse width (1  $\mu$ s) and repetition rate (5 kHz). Experimental and simulation results are compared for the propagation region of the plasma outlets. The creation of a helium gas channel through the surrounding air prevents quenching by oxygen molecules in the air allowing an ionization front to propagate forward. As a result, if the gas channel is not fed by enough helium atoms, the plasma bullet will stop propagating even at higher voltages due to the presence of abundant amount of oxygen molecules in air. Therefore, the determination of helium mole fraction along the propagation path plays a critical role.

The helium flow passing through the electrodes controls the length and homogeneity of the plasma jet. In this paper, the plasma jet length for different helium velocities is first measured, then the minimum corresponding helium mole fraction at the tip of the plasma jet is extracted from the helium flow simulation results. The experiments were carried out at a laboratory environment at sea level with a

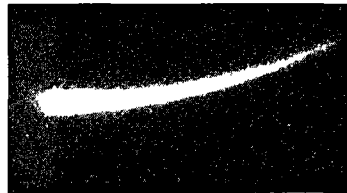


FIG. 35: An ICCD camera photograph when the plasma pencil is horizontally positioned with 3 m/s low helium flow velocity.

relative humidity of 40 % and a room temperature of 23 °C. Figure 36 demonstrates the variation of the plasma jet length with respect to the helium flow velocity. The trend is similar to that observed by Qing Li et al. [60]. The laminar, transition, and turbulence flow regimes shown in Figure 36 are determined by experimental observations using ICCD camera photographs. Transition regime is labeled in Figure 36 according to the helium flow velocity that the vortex structure appears at the tip of the plasma jet (around 8 m/s). At faster velocities (more than 13 m/s) this vortex structure of the helium flow becomes dominant along the plasma jet and causes the plasma bullet inhibition at much shorter distances. The length of the plasma jet is measured by using an ICCD camera with a 1.3  $\mu$ s exposure time for different helium velocities. A constant 6 kV high voltage having a 1  $\mu$ s pulse width and 5 kHz repetition rate is applied. For each helium velocity, the measurements are repeated 20 times to obtain an average plasma jet length. For our simulations, the helium flow is assumed to be laminar theoretically. This is verified experimentally at lower gas flow velocities. However, at higher velocities the helium flow experiences turbulence even though the Reynolds number remains smaller than the critical value. However, for the buoyant helium jets inside ambient air, it has been shown both numerically and experimentally that turbulence is present even at a low Reynolds number in conjunction with a Richardson number [61]. In the laminar regime, an increase in the helium velocity results in a direct increase in the plasma jet length, which reaches up to 95 mm. However, in the transition and turbulent regimes, the plasma jet first starts fluctuating, then becomes unstable and smaller. Therefore, a proper ratio of the helium flow velocity and hole size for optimum operating conditions is needed to establish a laminar flow and avoid turbulence.

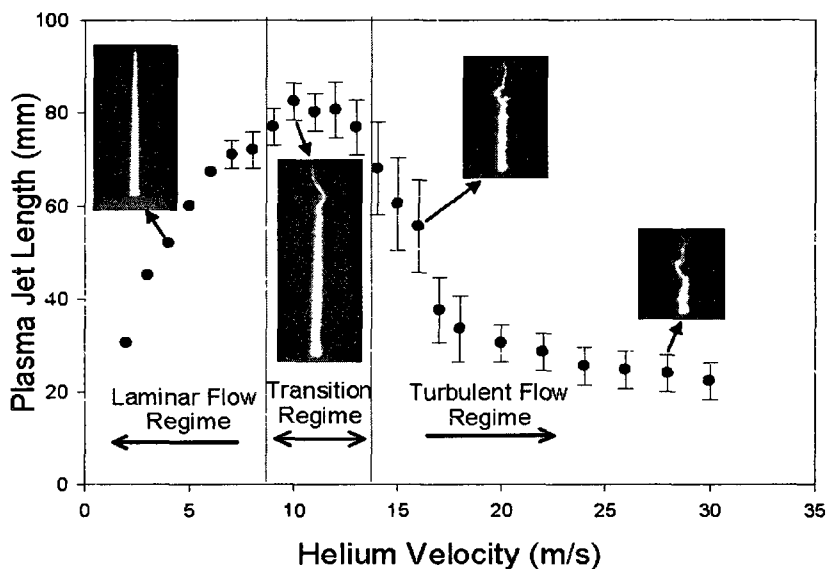


FIG. 36: Plasma jet length versus helium velocities for a constant 6 kV, applied high voltage, 1  $\mu$ s pulse width, and 5 kHz repetition rate. Flow regimes are determined by experimental observations using ICCD camera photographs.

Computational fluid dynamics simulation for the plasma bullet propagation region is performed by a commercially available partial differential equation solver (COM-SOL Multiphysics 3.4). The governing equations consist of the steady Navier-Stokes, continuity, and convection - diffusion equations as follows:

$$-\nabla[\eta(\nabla u + (\nabla u)^T)] + \rho(u \cdot \nabla)u + \nabla p = F \quad (9)$$

$$\nabla \cdot (\rho u) = 0 \quad (10)$$

$$\nabla(\rho D \nabla c - c \rho u) = 0 \quad (11)$$

where  $u$  is the velocity field,  $\rho$  is the total density,  $p$  is the pressure,  $\eta$  is the dynamic viscosity (  $1.94 \times 10^{-5}$  Pa.s for He and  $1.82 \times 10^{-5}$  Pa.s for air),  $D$  is the diffusion coefficient (  $7.2 \times 10^{-5}$   $m^2 \cdot s^{-1}$  for He in air),  $c$  is the helium mole fraction  $mol \cdot m^{-3}$ , and



$F$  is the body force field (buoyancy). It is worth noting that even though the buoyancy force is small, it is noticeable when the plasma pencil is horizontally positioned, and flow velocities are small.

Since the plasma jet as well as the diffusion of helium into the surrounding air takes place on the outside of the plasma pencil, the simulation domain extends to 200 mm in height and 100 mm in diameter in order to eliminate the boundary effects. Because of the cylindrical structure of the plasma pencil, there is no variation in the radial direction. Hence, a two-dimensional axisymmetric assumption can be made. The simulation domain consists of 5800 triangular elements (Figure 37). Mixture gas density depends on the helium mole fraction, which is computed from the ideal gas law using local pressure and mixture composition. The difference between the gas mixture density and the air density accounts for the buoyancy force in the axial direction. The dynamic viscosity of the mixture also depends on the local variations of mixture composition. Therefore, it is computed using the helium mole fraction and mixture averaging formula. A grid convergence study is also performed in order to obtain a grid independent solution. Grid size is refined near the plasma pencil exit as well as near the symmetric plane to capture sharp gradients. As mentioned earlier, the flow is assumed to be laminar. In addition, the effect of the charged particles was not taken into account because the lifetime of charged particles is very short in comparison to the repetition rate of the high voltage: the high voltage is only applied to the electrodes for 1  $\mu$ s, and the system will be at rest during the next 200  $\mu$ s until another pulse arises.

TABLE 4: The computational boundary conditions.

Boundary	Navier-Stokes	Convection-Diffusion
AB	Inlet Velocity	Unit Mole Fraction
HA	No Slip	Insulation
GH	No Slip	Insulation
FG	No Slip	Insulation
EF	Inlet Velocity	Zero Mole Fraction
DE	Open Boundary	Convection Flux
CD	Open Boundary	Convection Flux
BC	Axial Symmetry	Axial Symmetry

The boundary conditions used in our numerical simulations are as follows. At the plasma pencil exit, the inlet velocity ( $u_0$ ) profile is laminar and fully developed, and the helium mole fraction is unity. No slip conditions are imposed on the inner

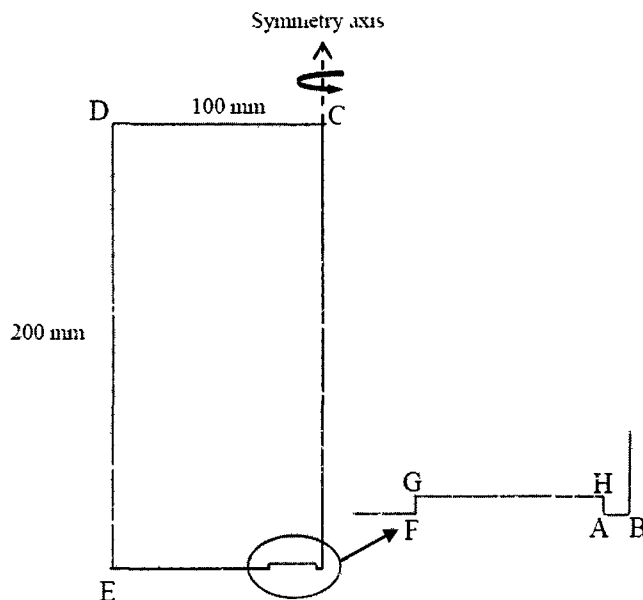


FIG. 37: The computational mesh domain.

and outer walls of the plasma pencil which corresponds to the insulation boundary condition for convection-diffusion equation. An inlet velocity ( $2\%$  of  $u_0$ ) is prescribed at the EF boundary in Table 4 in order to increase the convergence of the solver. At this boundary, zero helium mole fraction is imposed. The remaining boundaries are specified as open boundaries, where helium is transported out of the domain by convection. The initial conditions for both axial and radial velocities as well as helium mole fraction are set to be zero

The simulation is only performed for helium exit velocities ( $u_0$ ) from 3 m/s to 10 m/s. The fluid dynamics simulation in the turbulent regime has not been employed due to the complex physical mechanism of turbulence. In addition, as shown in Figure 36, the turbulent regime is not a case for optimum operating conditions. The simulation results are extracted to determine the corresponding minimum helium mole fraction value at the tip of the plasma jet (Figure 38), which stands for a point where the plasma bullet stops propagating. As discussed earlier, in order to sustain the plasma bullet propagation, a certain magnitude of power and amount of helium flow should always be maintained in the ionization channel with a constant pulse

width and repetition rate.

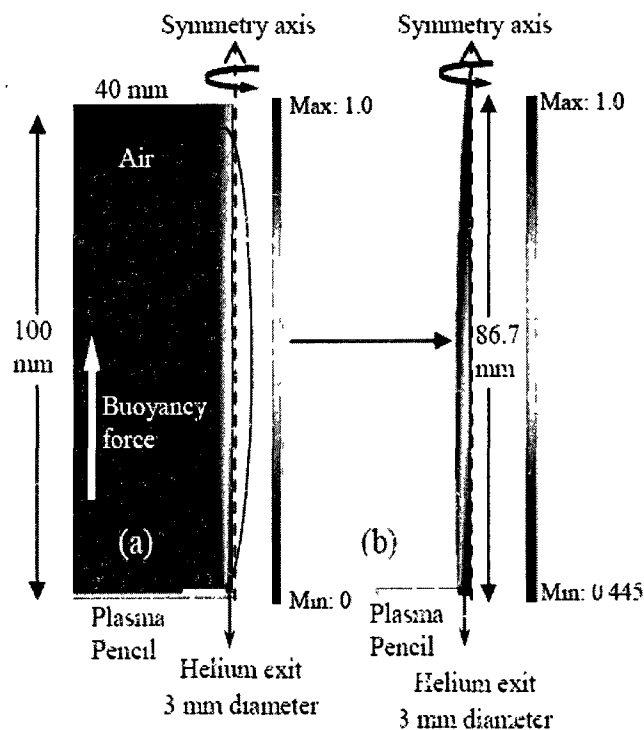


FIG. 38: (a) The helium mole fraction simulation near the helium exit for 8 m/s helium velocity, 6 kV applied high voltage, 1  $\mu$ s pulse width, and 5 kHz repetition rate, (b) Extracted simulation corresponding to the real plasma jet length and structure. For this case, the plasma jet length is 86.7 mm, and the helium mole fraction at the end of plasma jet is 0.445.

The minimum helium mole fraction in Figure 39 and Figure 40 is obtained from the calculated one at the distance corresponding to the measured plasma jet length. Figure 39 shows the minimum corresponding helium mole fraction values along the plasma jet as a function of the helium exit velocity based on computational results. These results are provided to show how much helium mole fraction is necessary to sustain the plasma bullet propagation under different helium exit velocities. According to this figure, as the helium exit velocity increases, the corresponding helium mole fraction value also increases. It is important to note that there is no 1:1 ratio between the plasma jet length and the helium exit velocity. In terms of Figure 36, when the helium exit velocity increases from 1X m/s to 2X m/s, the plasma jet

length does not increase from 1X mm to 2X mm for the laminar flow regime, and it remains at relatively shorter lengths. However, it is important to note that faster helium exit velocities correspond to the same helium mole fraction values at further distances than for slower velocities.

The magnitude of the applied high voltage is also a key parameter affecting the plasma jet length. Figure 40 represents the effect of high voltage on the helium mole fraction for a constant 8 m/s flow velocity, 1  $\mu$ s pulse width, and 5 kHz repetition rate. According to this figure, an increase in high voltage leads to smaller minimum corresponding helium mole fraction needed to sustain the bullet propagation (i.e. longer plasma jet length). Stated differently: as the high voltage increases, more energy is transferred into the ionization channel; thus, a longer plasma jet is possible with smaller helium mole fraction.

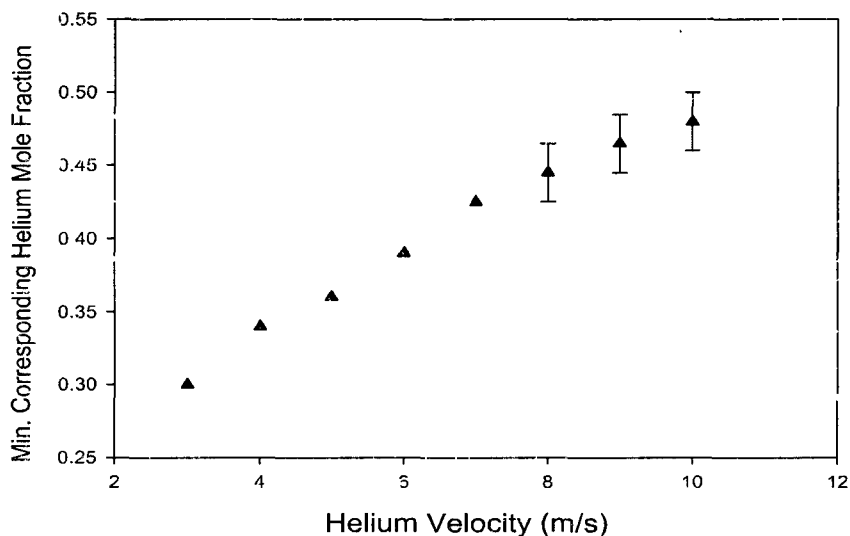


FIG. 39: The minimum corresponding helium mole fraction at the tip of the plasma jet as a function of different helium velocities for a constant 6 kV applied high voltage, 1  $\mu$ s pulse width, and 5 kHz repetition rate.

The importance of feeding a new volume of helium gas along the ionization channel is demonstrated by optical emission spectroscopy and ICCD camera observations. These findings prove that the plasma bullet propagation path directly depends on

the structure of the helium flow channel. Electron avalanches colliding with the background helium gas initiate chemical reactions leading to Penning ionization mechanism. In order to determine the limits of the helium mole fraction along the ionization channel, a fluid dynamics simulation is performed with the helium exit velocity as a variable. In conclusion, it is found that the helium mole fraction should be more than a critical value along the plasma bullet propagation path in order to sustain the necessary chemical reactions in the plasma bullets.

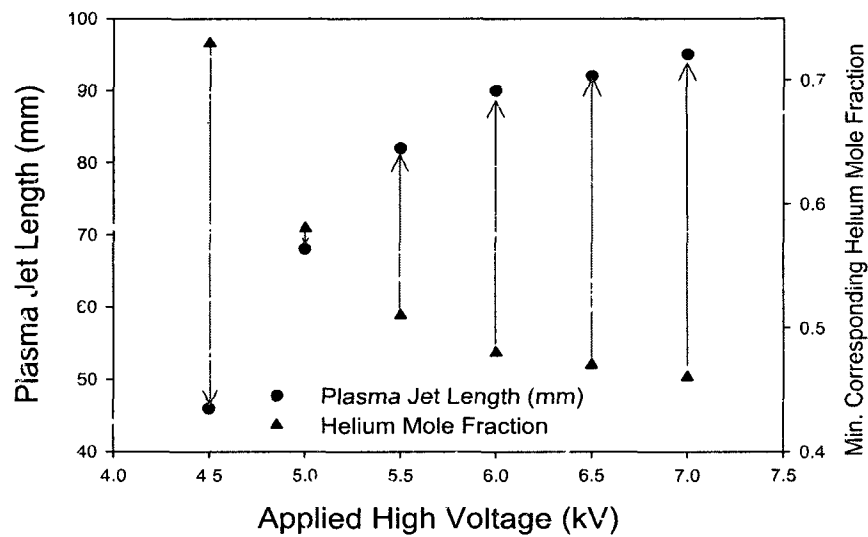


FIG. 40. The plasma jet length and the minimum corresponding helium mole fraction at the tip of the plasma jet as a function of applied high voltage for a constant 10 m/s helium flow, 1  $\mu$ s pulse width, and 5 kHz repetition rate.

### IV.2.2 Secondary discharge ignition effect

As the plasma bullet propagates further, it leaves behind an ionization channel consisting of short-lived and long-lived reactive species. This is supported by ICCD camera photographs shown in Figure 41 and temporal OES data shown in Figure 42

Our current experimental setup allows identifying only emitting species associated with short-lived species along the ionization channel. The temporal evolution of the emitting species provides an insight into the constituents of the channel. During experiments, the focal point of our lens is 20 mm away from the plasma pencil. Basically, as the plasma bullet passes through this focal point, the distribution of the emitting species is recorded by the monochromator. The emitting species distribution at the ionization front is relatively low. As the plasma bullet propagates a little forward, the magnitude of the emission increases and eventually reaches its highest value. Then, the emission decreases exponentially until it reaches low emission levels (Figure 42). This proves that even though the ionization front moves 50-60 mm away from the plasma pencil, it leaves behind short-lived reactive species which remain at low concentration values along the ionization channel.

The channel initially appears as an extension of the plasma bullet. If the applied voltage is sufficiently high, the plasma bullet eventually breaks off this extension. The time when the plasma bullet breaks off is determined as a function of the applied voltage. This break-off time corresponds to a point when the short-lived reactive species are at very low concentrations making them invisible to the ICCD camera (The ICCD camera can track emissions between 200 nm - 900 nm wavelengths). It is found that the plasma bullet breaks off faster at higher voltages (Figure 43). This is due to faster velocity of the plasma bullet at higher voltages. However, this break-off time is independent of the pulse width.

Even when the plasma bullet breaks off, the secondary discharge ignition (initially occurring inside the device) is still able to inhibit the propagation of the plasma bullet. This supports the idea that long-lived species exist throughout the ionization channel along with low concentrations of short-lived species, which helps the outward expansion of the secondary discharge. Therefore, the secondary discharge initially ignited at the dielectric electrode surface propagates along the ionization channel, and then stops the plasma bullet from propagating in an abrupt manner. In order to observe the secondary discharge propagation, the operating conditions of the plasma pencil are set to 7 kV applied high voltage and 2800 ns pulse width, which allow for

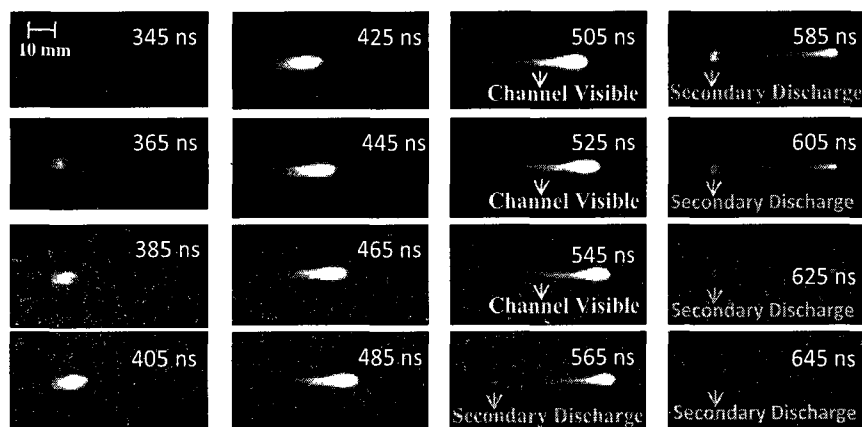


FIG. 41: The plasma bullet propagation showing the channel consisting of emitting species along the ionization channel. Secondary discharge ignition causing the plasma bullet inhibition (applied voltage: 5.5 kV; pulse width: 300 ns; repetition rate: 5 kHz; flow rate: 5.0 L/mm).

an easy observation of the secondary discharge during its propagation. In addition, the 2800 ns pulse width provides for a good separation of this propagation from that of the plasma bullet, and eliminates the contribution of the short-lived species along the ionization channel.

Figure 44 shows that the secondary discharge also travels in the air up to 40 mm away from the reactor. Therefore, it is deduced that the secondary discharge ignition creates another propagation in the surrounding air

The secondary discharge effect on the plasma bullet inhibition can be explained by our very recent experimental observations. Based on these observations, it is confirmed that the plasma bullets adopt the streamer propagation mechanism as was proposed in Ref [10]. These observations show that the plasma bullets generated by positive applied voltages travel similarly as in the case of the cathode-directed streamers. In this streamer mechanism, the electron flow is opposite to the direction of propagation of the plasma bullet. It is also found that during the propagation a number of the electrons accumulate onto the positive electrode dielectric surface. The electron number in this accumulation is almost equal to the electron number in the

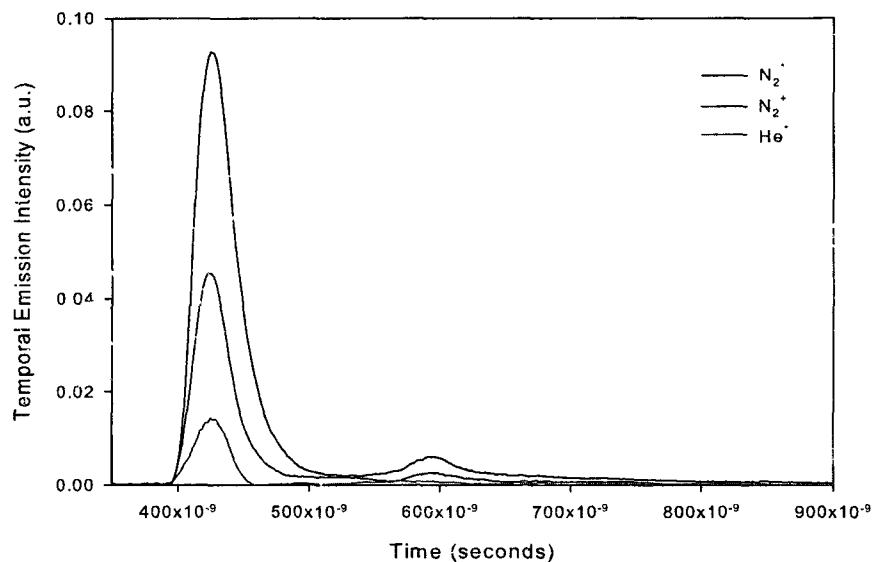


FIG 42. Temporal evolution of the reactive species at 20 mm away from the plasma pencil (applied voltage: 5.5 kV; pulse width: 1000 ns; repetition rate: 5 kHz; flow rate: 5.0 L/min)

plasma bullet. When these electrons are released from the dielectric surface at the end of the applied voltage pulse, they create an opposing current along the ionization channel. Therefore, this “negative current”, acting against the normal succession of events during the bullet propagation, leads to slowing down of the plasma bullet and then eventually its inhibition. This phenomenon was already discussed in the previous section.



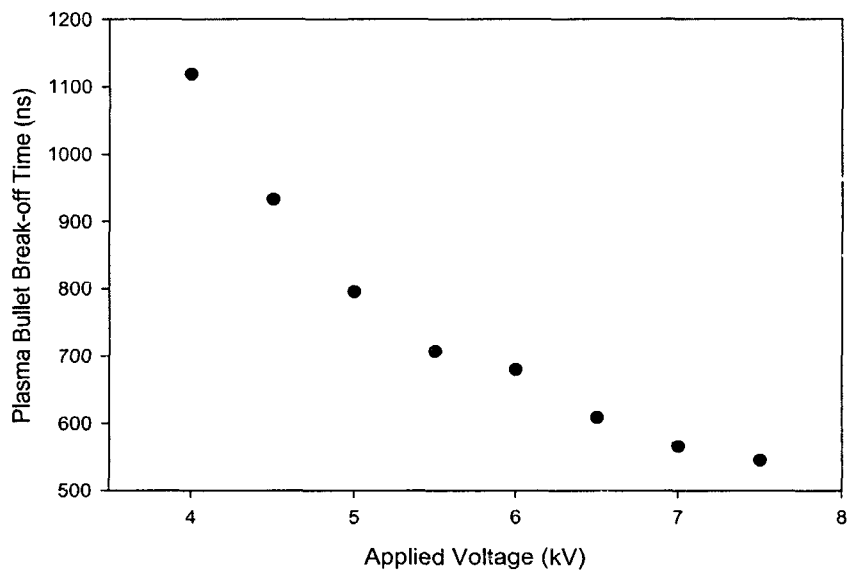


FIG. 43: Plasma bullet break-off time for different applied voltages (pulse width: 2000 ns; repetition rate: 5 kHz; flow rate: 5.0 L/min).

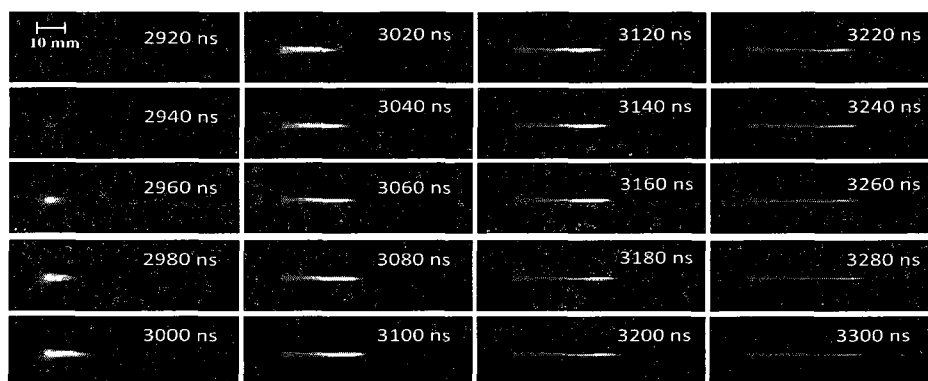


FIG. 44: Secondary discharge propagation at 7 kV applied voltage and 2800 ns pulse width.

### IV.3 ACCURATE MEASUREMENT OF THE PLASMA BULLET VELOCITY BY OPTICAL EMISSION SPECTROSCOPY

Measurement of the plasma bullet velocity is an important and necessary task for the investigations of the dynamics of the plasma bullet propagation. In several studies [10, 11, 25, 28], the plasma bullet velocity was measured using ICCD camera images. High-speed photography based on the ICCD cameras allows observing the plasma dynamics in time domain with resolutions as low as a few nanoseconds. Even though this technique is unique, the resolution of the ICCD cameras is not high enough for the plasma bullet velocity to be measured in detail.

In our previous work, the instantaneous plasma bullet velocity was determined by an ICCD camera with a resolution of 20 ns [11]. This resolution is not enough to elucidate the detailed behavior of the plasma bullet during its propagation in the surrounding air. In previous work, it was reported that the plasma bullet starts its propagation with relatively lower velocities, and then it reaches its maximum. As it travels further, its velocity decreases. Finally, at the end of the applied voltage pulse, the plasma bullet stops propagating. Unfortunately, fluctuations in the instantaneous plasma bullet velocity plagued the measurements in that study.

Although the resolution of the ICCD cameras could be as low as 3 ns in theory, an exposure time of around 20 ns is usually needed to collect a sufficient amount of photons in order to observe the plasma bullet. In addition, a precise protocol is necessary to identify a reference point in order to measure the distance from the plasma bullet to the reactor. This rendered the task particularly difficult and required the use of advanced image processing technique.

In the present study, a time-resolved OES is applied to the measurement of the plasma bullet velocity with a resolution as good as 0.5 ns. Figure 42 shows the temporal evolution of the reactive species at 20 mm away from the plasma pencil for the applied voltage of 5.5 kV with a 1  $\mu$ s pulse width. Spectral lines for these reactive species are as follows:  $N_2^*$  (second positive system (SPS)): 337.1 nm line of  $C^3\Pi_u \rightarrow B^3\Pi_g$ ,  $N_2^+$  (first negative system (FNS)): 391.4 nm line of  $B^2\Sigma_u^+ \rightarrow X^2\Pi_g^+$ , and  $He^*$ : 706.5 nm line. The chosen lines are determined in terms of the magnitude of emissions in their spectral systems.

Based on Figure 42, the reactive species emit their highest peaks at around 430 ns. The occurring time of these peaks depends on the magnitude of the applied voltage and the focusing position of the lenses along the plasma jet. For example, at

further spatial points the highest peak occurs later, or with higher applied voltages the highest peak occurs earlier. The former is illustrated in Figure 45. In this technique, these shifts will be basically utilized for the measurement of the plasma bullet velocity.

The average and instantaneous plasma bullet velocities are measured from the temporal evolution of the reactive species. The emitted light is collected along the plasma jet, and is monitored on a wideband oscilloscope. The time that the plasma bullet propagates in the air (i.e. time of the highest peak of the reactive species emission) is measured at the peak of the temporal evolution of the reactive species. The distance to the plasma pencil is precisely measured by an adjustable micrometer.

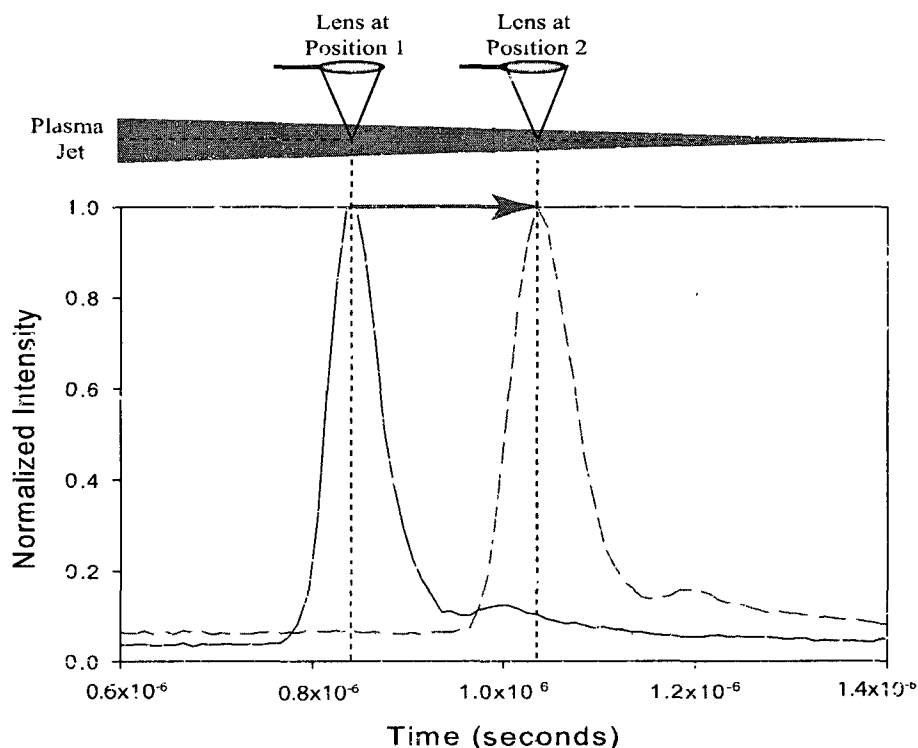


FIG. 45: Showing a shift of the highest emission peak for the plasma bullet velocity measurements

The average plasma bullet velocity is calculated at the peaks of  $N_2^*$ ,  $N_2^+$ , and  $He^*$  temporal emissions as a function of the applied voltage. The launching time of the plasma bullet is determined by an ICCD camera, and then it is subtracted from

the time of the highest peak in order to calculate the average plasma bullet velocity more accurately. It is found that the average plasma bullet velocity increases as the applied voltage increases (Figure 46). In addition, identical average plasma bullet velocity is obtained from the emission of different reactive species for each applied voltage.

The instantaneous plasma bullet velocity is calculated from the consecutive temporal emissions of  $N_2^*$  (SPS) at 337.1 nm along the plasma jet since  $N_2^*$  (SPS) at 337.1 nm is one of the strongest emissions along the plasma jet. Each consecutive measurement is done by only one PMT (only the focal point is displaced by a micrometer). The oscilloscope output is averaged 500 times in order to obtain more accurate data. Therefore, the resolution of the oscilloscope allows decreasing the time error to 0.5 ns for each acquisition. As shown in Figure 47, the instantaneous plasma bullet velocity does not follow a smooth velocity curve due to the highly collisional medium of air at atmospheric pressure. However, the numerous experimental observations show a consistent pattern. The instantaneous plasma bullet velocity experiences three different phases during its travel: launching, propagation, and ending (Figure 47). The plasma bullet launches from the plasma pencil with relatively lower velocities, and then it reaches its maximum at  $1.1 \times 10^5$  m/s. This increase is due to an excessive amount of nitrogen molecules in the air [11]. After that, the plasma bullet enters the propagation phase. During the propagation, its velocity remains almost constant. At the end of the pulse, the applied high voltage starts decreasing, and the plasma bullet comes to an end at around 70 mm in an abrupt manner. These three phases can be seen from the ICCD camera photographs in Figure 48. It is worth noting that the velocity measurements at the early beginning and late ending of the propagation are unstable (grey regions in Figure 47). In these regions, the plasma bullet is not propagating or seems to oscillate back and forth. For the early beginning, the reason of this instability is that the plasma bullet just starts being formed, and is still in contact with the reactor (i.e. the dielectric surface of the electrode). And, as stated in Ref. [11], air molecules start playing an important role in the plasma bullet propagation mechanism. For the late ending, as discussed in previous section, the plasma bullet cannot sustain the chemical reactions due to quenching of excited states by air molecules after a certain spatial point. This quenching phenomenon causes the plasma emission to faint, undergoing electron attachment and ion recombination at the end of the pulse. That point corresponds to the late ending of the plasma bullet

propagation.

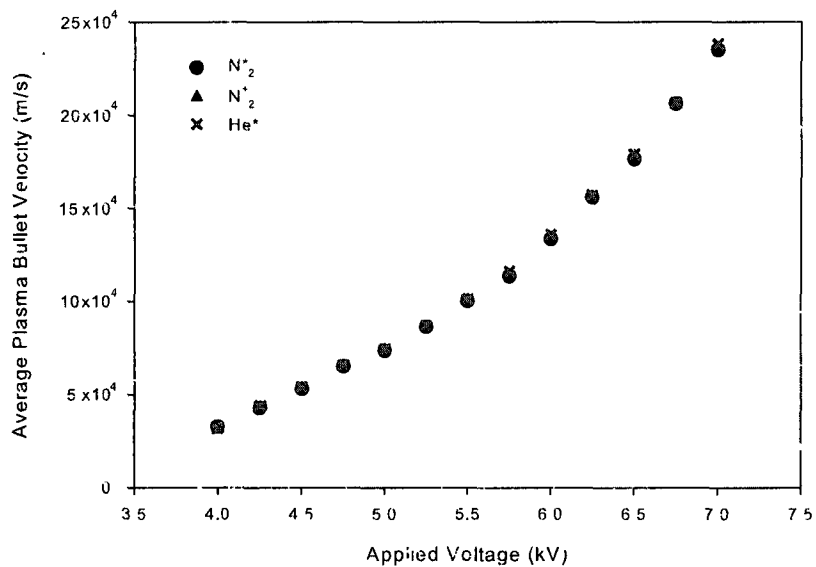


FIG 46: The average plasma bullet velocity for different reactive species as a function of the applied voltage (pulse width: 2000 ns; repetition rate: 5 kHz; flow rate: 5.0 L/min).

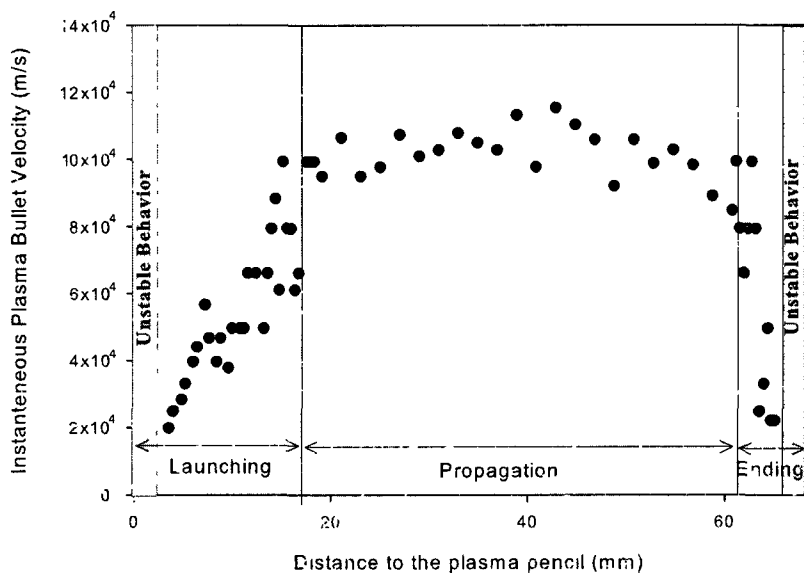


FIG. 47: The instantaneous plasma bullet velocity from the emission of SPS by a time-resolved OES applied voltage: 5.5 kV; pulse width: 2000 ns; repetition rate 5 kHz; flow rate: 5 L/min).

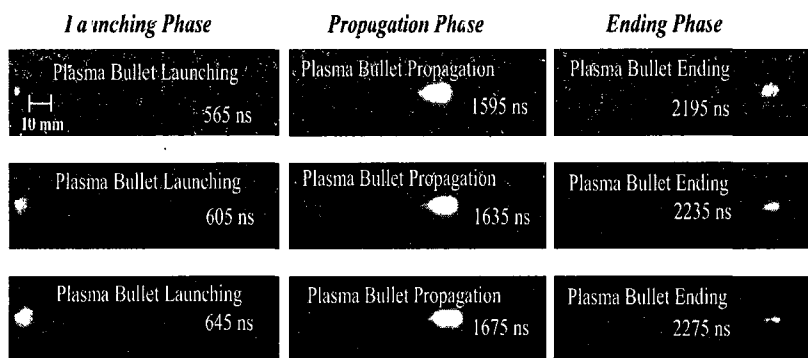


FIG. 48. Plasma bullet experiences three different phases: launching, propagation, and ending (applied voltage: 5.5 kV; pulse width: 2000 ns; repetition rate: 5 kHz; flow rate: 5 l./min).

#### IV.4 SUMMARY

The jet current of the APLTPJ generated by the tube reactor was measured by a Rogowski coil for different applied voltages and axial positions. These jet current measurements indicated that the propagation characteristics of the plasma bullets are similar to that of streamers. Therefore, an ionization wave exists and propagates along the plasma jet. This similarity to the streamers was not only limited to the positive applied voltages (cathode-directed streamers) but also for the negative applied voltages (anode-directed streamers). This is especially important for adequate explanations of the plasma bullet propagation. The secondary discharge, ignited by the charge accumulation on the dielectric electrode surfaces at the end of the applied voltage pulse, interrupts the plasma bullet propagation due to an opposing current along the ionization channel. The reason for this phenomenon was also discussed.

Maximum electron density of the plasma bullet was estimated by using the jet current information. It was found that the maximum electron density of the plasma bullet is in the order of  $10^{16} \text{ m}^{-3}$ . An empirical relationship between the plasma bullet velocity and the plasma bullet area was also adopted from the streamer discharges:  $v_b \cong 1.46A \text{ m.ns}^{-1}$ .

The plasma bullet lifetime depends on helium mole fraction along the ionization channel, the width of the applied voltage pulse and its magnitude, and the secondary discharge ignition time. The plasma bullet follows the trajectory of the helium gas channel, indicating that the helium mole fraction value along the ionization channel should be more than a critical limit to sustain the propagation. This critical value was determined. The width of the applied voltage pulse was also important. For pulse widths less than a limit the plasma bullet stops propagating just after the secondary discharge ignition, which occurs at the end of the applied voltage pulse. For longer pulses the diffusion of air into the helium channel extinguishes the plasma bullet before the arrival of the secondary discharge. In addition, how much energy is transferred into the ionization channel is an important parameter because the plasma bullet dissipates its energy as it propagates forward.

A new technique using time-resolved OES was employed for the accurate determination of the plasma bullet velocity. The velocity of the plasma bullet is an important parameter for understanding its behavior. It is worth noting that this velocity is in the supersonic region without any externally applied electric field. It was found that the average plasma bullet velocity increases as the energy transferred into

the ionization channel increases; also, different reactive species travel with similar velocities. Our previous results regarding the instantaneous plasma bullet velocity have been greatly improved by increasing the resolution of our measurements. This new high resolution enabled us to observe a pattern along the plasma jet covering three different phases: launching, propagation, and ending.



## CHAPTER V

### SPECTROSCOPIC INVESTIGATIONS

Optical emission spectroscopy (OES) has unique capabilities for the investigation of atmospheric pressure low temperature plasma jets (APLTPJs) as a non-intrusive technique. OES is able to determine the evolution of the chemical species over the plasma bullet/plume/jet for different operating conditions.

The spectral data is recorded by an Acton Research PD-471 photomultiplier tube (PMT) mounted on a 0.5 m Acton Research Spectra-Pro 500i monochromator. The dimension of adjustable slits is 4 mm in height and 10  $\mu\text{m}$  to 3 mm in width. Gratings are 3600 g/mm for ultraviolet (UV) spectrum (200-466 nm) and 1200 g/mm for visible-infrared (visible-IR) spectrum (467-1400 nm). Spectra are recorded on a computer using NCL electronic interface and SpectraSense software. The detailed information about the OES system was given in chapter II.

The tube reactor is employed during the OES acquisitions. Its simple geometrical structure makes a homogeneous helium gas channel possible leading to an axisymmetric plasma chemistry along the plasma jet. The width of the spectrometer slit, the measurement step, and integration time are usually adjusted to 50  $\mu\text{m}$ , 0.001 nm, and 200 ms, respectively. A double-convex UV-grade filter is used for visible-IR spectra to prevent higher order dispersion due to intense emissions of the second positive system (SPS) of  $N_2$  and the first negative system (FNS) of  $N_2^+$ .

In this chapter, the chemical makeup of the APLTPJs is investigated for different operating conditions. Ambient air around the inert gas channel makes plasma chemistry complicated. This complicated plasma chemistry will be temporally and spatially explored along the plasma jet.

#### V.1 GENERAL VISIBLE-IR AND UV SPECTRA FOR DIFFERENT WORKING GASES

The presence of an inert gas is required for the generation of a low temperature plasma jet in the ionization channel. Most APLTPJs are usually fed by helium or argon flows, or a mixture of them, such as He/Ar, He/O<sub>2</sub>, or He/Air. The targeted application and the device geometry determine the suitability of the chosen gas type. The excitation and ionization levels of chosen inert gas are also important. As discussed

in the previous chapter, the production of the metastable atoms in the ionization channel is key to sustaining the plasma bullet propagation. It was recently found that Penning ionization is mainly responsible for the generation of helium fed APLTJs [15, 56, 57, 60, 62].

The general spectra for the helium gas and helium/oxygen and helium/argon mixtures were taken to identify the emitting species at 20 mm away from the nozzle of the tube reactor. Experimental parameters were as follows: 9 kV applied voltage, 2  $\mu$ s pulse width, 5 kHz repetition rate, and 5 L/min flow rate. The entrance and exit slit widths were adjusted to 10  $\mu$ m. Photomultiplier tube (PMT) voltage was set to 900 V for the UV spectrum and 1200 V for the visible-IR spectrum. The monochromator step size was 0.05 nm.

The main kinetic mechanisms for pure helium and helium/argon mixtures are summarized in Table 5 and Table 6. Reaction rates are taken from Ref. [63, 64, 65]. Kinetic mechanism of helium/oxygen mixture will not be elaborated here since it resembles that of pure helium. At a glance, excitation and ionization by electron impact, Penning ionization mechanism by helium metastables, and charge and excitation transfers mainly sustain kinetic mechanisms of the plasma jet.

Metastable energy levels of helium and argon atoms,  $C$  level of  $N_2$ , and  $X$  and  $B$  levels of  $N_2^+$  are given in Table 7. Since the metastable energy levels of helium are higher than the ionization energy level of nitrogen molecules, Penning ionization mechanism of RH7 reaction plays a dominant role to sustain the discharge in the presence of air. Excimer molecules can be produced by three-body collisions as seen in RH8. These molecules, before self-radiative decay, can dissociate through Penning ionization of RH9 and RA15 and OH radical production of RH10 and RA16.

Although metastable energy levels of the argon atom are much lower than those of helium (Table 7), the roles of argon metastables and excimers are also important to sustain the discharge mechanism in helium/argon mixture. Accordingly, argon metastables and excimers can be de-excited by Penning ionization of RA5 and RA6 and OH radical production of RA9. When argon is mixed with nitrogen, nitrogen metastables are also highly produced due to energy levels of argon atoms and nitrogen molecules [62, 68]. Therefore, stepwise ionization reactions of RA12 and RA13 could be effective [62, 68].

TABLE 5: Kinetics mechanisms in the plasma jet fed by pure helium

Label	Reactions	Reaction Rate [63, 64, 65]
RH1	$e + He \rightarrow He^* + e$	$3.88 \times 10^{-16} \exp(-1.40 \times 10^6/E) m^3 s^{-1}$
RH2	$e + He \rightarrow He^+ + 2e$	$4.75 \times 10^{-16} \exp(-2.31 \times 10^6/E) m^3 s^{-1}$
RH3	$e + He^m \rightarrow He^+ + 2e$	$2.02 \times 10^{-13} \exp(-3.10 \times 10^5/E) m^3 s^{-1}$
RH4	$e + N_2(X) \rightarrow N_2^+(B) + 2e$	
RH5	$e + N_2(X) \rightarrow N_2^+(C) + 2e$	
RH6	$e + N_2^m \rightarrow N_2^+(X) + 2e$	
RH7	$He^m + N_2(X) \rightarrow N_2^+(B) + He + e$	$5.0 \times 10^{-17} m^3 s^{-1}$
RH8	$He^+ + 2He \rightarrow He_2^+ + He$	$1.1 \times 10^{-43} m^6 s^{-1}$
RH9	$He_2^+ + N_2(X) \rightarrow N_2^+(B) + He_2^n$	$1.4 \times 10^{-15} m^3 s^{-1}$
RH10	$He_2^+ + H_2O \rightarrow OH(A) + HeH^+ + He$	
RH11	$N_2^+(B) \rightarrow N_2^+(X) + h\nu(391nm)$	
RH12	$N_2^+(C) \rightarrow N_2(B) + h\nu(337.1nm)$	$3.0 \times 10^7 s^{-1}$ [66]
RH13	$He^*(n \geq 3) + He \rightarrow He_2^+ + e$	$1.5 \times 10^{-17} m^3 s^{-1}$
RH14	$He_2^+ + e \rightarrow He^* + He \rightarrow 2He + h\nu$	$8.9 \times 10^{-16} (T_e/T_g)^{-1.5} m^3 s^{-1}$
RH15	$He^m + 2He \rightarrow He_2^m(B) + He$	$2.0 \times 10^{-46} m^6 s^{-1}$
RH16	$2He^m \rightarrow He_2^+(B) + e$	$1.5 \times 10^{-15} m^3 s^{-1}$
RH17	$2He_2^m \rightarrow He_2^+(B) + 2He + e$	$1.5 \times 10^{-15} m^3 s^{-1}$
RH18	$He_2^m + N_2 \rightarrow N_2^+ + 2He + e$	$3.0 \times 10^{-17} m^3 s^{-1}$
RH19	$N_2^+ + e \rightarrow N_2$	$4.8 \times 10^{-13} (T_e/T_g)^{-0.5} m^3 s^{-1}$

### V.1.1 Visible-IR spectra

The spectral identity of the working gas usually appears in the visible-IR spectrum (Figure 49). UV filters are highly important to prevent higher order diffraction.

Figure 49 shows the visible-IR spectrum for pure helium, helium/oxygen (0.05%  $O_2$ ) and helium/argon (10% Ar) mixtures. As seen in Figures 49.a and 49.b, helium emission lines are dominant for pure helium and He/ $O_2$  mixture. Even this small amount of  $O_2$  admixture quenches 522 nm peaks of SPS and remarkably intensifies 615 nm and 777.1 nm peaks of the oxygen atom. On the other hand, argon admixture completely differs in the plasma chemistry. The reason for this distinction is due to different ionization and metastable levels of helium and argon atoms. As previously stated, helium atoms sustain the plasma jet with the Penning ionization mechanism. However, in the case of argon atoms, the stepwise ionization [62] also plays a key role along with Penning ionization mechanism. These are two main reasons why the

TABLE 6: Kinetics mechanisms in the plasma jet fed by helium/argon mixture.

Label	Reactions	Reaction Rate
RA1	$e + Ar \rightarrow Ar^* + e$	$1.0 \times 10^{-17} T_e^{0.75} \times \exp(-11.6/T_e) m^3 s^{-1}$ [67]
RA2	$e + Ar \rightarrow Ar^+ + 2e$	$4.0 \times 10^{-12} T_e^{0.5} \times \exp(-15.8/T_e) m^3 s^{-1}$ [67]
RA3	$e + Ar^m \rightarrow Ar^+ + 2e$	
RA3	$e + Ar \rightarrow Ar^m + e$	
RA4, RH7	$He^m + N_2(X) \rightarrow N_2^+(B) + He + e$	$5.0 \times 10^{-17} m^3 s^{-1}$ [63, 65]
RA5	$Ar^m + N_2 \rightarrow N_2(C) + Ar$	
RA6	$Ar_2^* + N_2 \rightarrow N_2(B) + 2Ar$	
RA7	$He^m + Ar \rightarrow He + Ar^+ + e$	
RA8	$Ar^+ + N_2(X) \rightarrow N_2^+(X) + Ar$	
RA9	$Ar^m + H_2O \rightarrow OH(A) + H + Ar$	
RA10, RH4	$e + N_2(X) \rightarrow N_2^+(B) + 2e$	
RA11, RH5	$e + N_2(X) \rightarrow N_2^+(C) + 2e$	
RA12	$e + N_2(A^3 \Sigma_g^+) \rightarrow N_2^+(X) + 2e$	
RA13	$N_2(A^3 \Sigma_g^+) + N_2(a^1 \Sigma_u^-) \rightarrow N_2^+ + N_2$	
RA14, RH8	$He^+ + 2He \rightarrow He_2^+ + He$	$1.1 \times 10^{-43} m^6 s^{-1}$ [63, 65]
RA15, RH9	$He_2^+ + N_2(X) \rightarrow N_2^+(B) + He_2^m$	$1.4 \times 10^{-15} m^3 s^{-1}$ [63, 65]
RA16, RH10	$He_2^+ + H_2O \rightarrow OH(A) + HeH^+ + He$	
RA17, RH11	$N_2^+(B) \rightarrow N_2^+(X) + h\nu(391nm)$	
RA18, RH12	$N_2^+(C) \rightarrow N_2(B) + h\nu(337.1nm)$	$3.0 \times 10^7 s^{-1}$ [66]

chemistry of helium/argon mixture exhibits different behavior.

We will first discuss the most intense line of helium at 706.5 nm. The effect of argon admixture on the plasma chemistry will be detailed in the next section.

### He $3^3S_1 \rightarrow 2^3F_{0,1,2}$ transition at 706.5 nm

The helium  $3^3S_1$  state can be populated [69] by electron collisions with the helium ground state ( $E_{threshold} = 22.72$  eV), helium metastable state ( $E_{threshold} = 2.9$  eV), and reactions of RH9, RH13, and RH14

- RH9:  $He^+ + 2He \rightarrow He_2^+ + He$
- RH13:  $He^*(n \geq 3) + He \rightarrow He_2^+ + e$
- RH14:  $He_2^+ + e \rightarrow He^* + He \rightarrow 2He + h\nu$

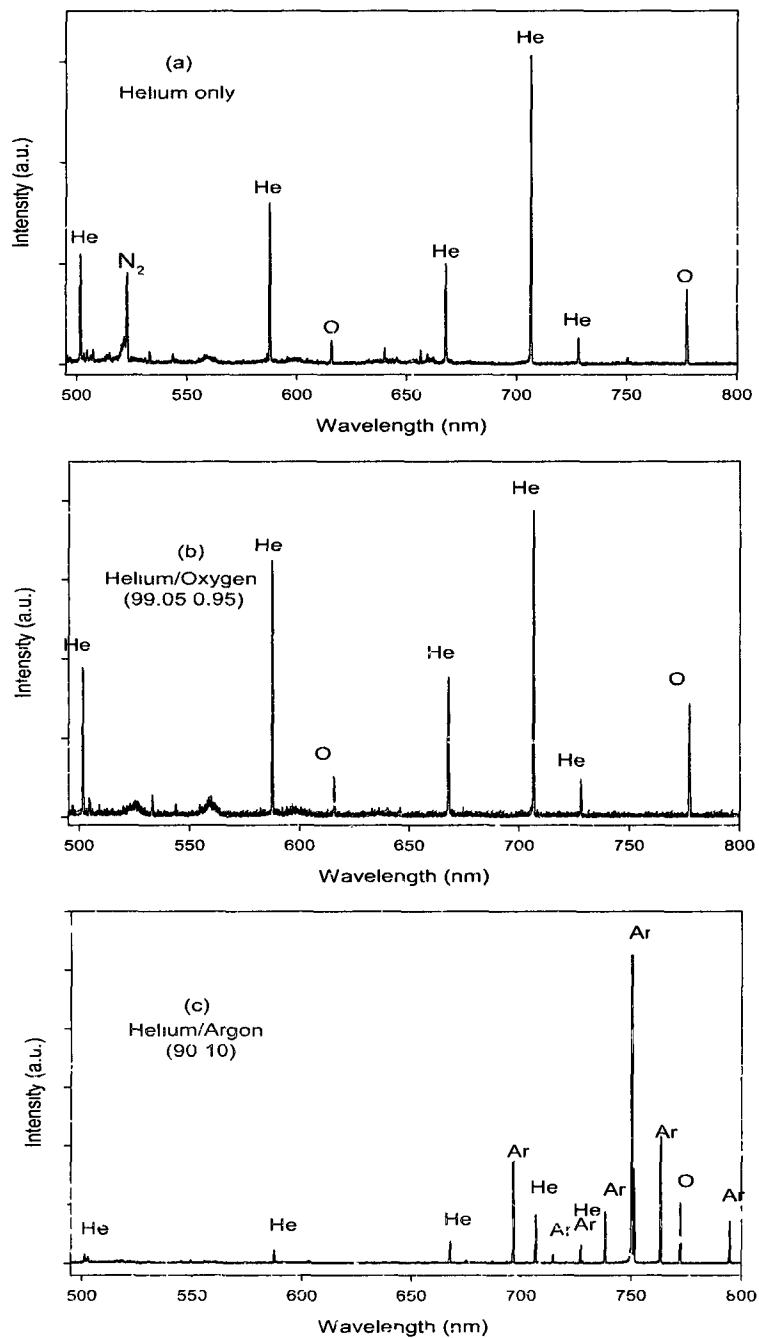


FIG. 49: General spectra of visible-IR wavelength range for pure helium, helium/oxygen, and helium/argon mixtures.

TABLE 7: Energy levels of helium and argon metastables,  $C$  level of  $N_2$ , and  $X$  and  $B$  level of  $N_2^+$ .

Species	State	Level (eV)
$He^m$	$^3S_1, ^1S_0$	19.8, 20.6
$Ar^m$	$^3P_2, ^3P_0$	11.5, 11.7
$N_2$	$C$	11.1
$N_2^+$	$X$	15.6
$N_2^+$	$B$	18.7

where RH9, RH13, and RH14 are  $He_2^+$  production via three-body collision, associative ionization, and dissociative recombination, respectively. As seen in reactions above, excited helium atoms and ions that are produced by the inelastic collisions of electrons with helium atoms at high pressures are rapidly converted into the excimer molecules and molecular ions [70]. The reaction rates of these conversions are  $5 \times 10^8$  and  $5 \times 10^7$  in RH8 and RH13, respectively. Therefore, the time of breakdown (of the order of  $10^{-6}$ s) is much higher than the characteristic time scales of these conversions [70]. For this reason, these reactions are usually considered as instantaneous phenomena.

In the case of low pressure helium discharges, the electron impact excitation plays a key role in the production of excited  $He^*$  atoms with relatively higher temperatures. At atmospheric pressures, the multi-step processes appear as the main excitation mechanism [69, 71]. This is especially true for the 706.5 nm line of helium atom [69]: He ( $3^3S_1$ ) upper state transition is resonantly generated in RH14 if  $He_2^+$  is vibrationally excited with  $\nu = 2$  and exothermically if  $\nu > 2$ . In addition, a highly excited vibrational state ( $\nu \sim 15$ ) produces  $He_2^+$  ions [72], and then vibrational relaxation rapidly occurs by ion-atom collisions [73]:  $He_2^+(\nu) + He \rightarrow He_2^+(\nu' < \nu) + He$ . On the other hand, if 706.5 nm emission line of excited helium is mostly populated by the dissociative recombination mechanism, this is a good indication of the presence of either electrons with energies more than 2.9 eV or  $He_2^+(\nu^*)$  and low energy electrons [69].

### V.1.2 UV spectra

General characteristics of the UV spectrum for all working gases give almost similar emissions with different intensities (Figure 51). No obvious evidence can be found

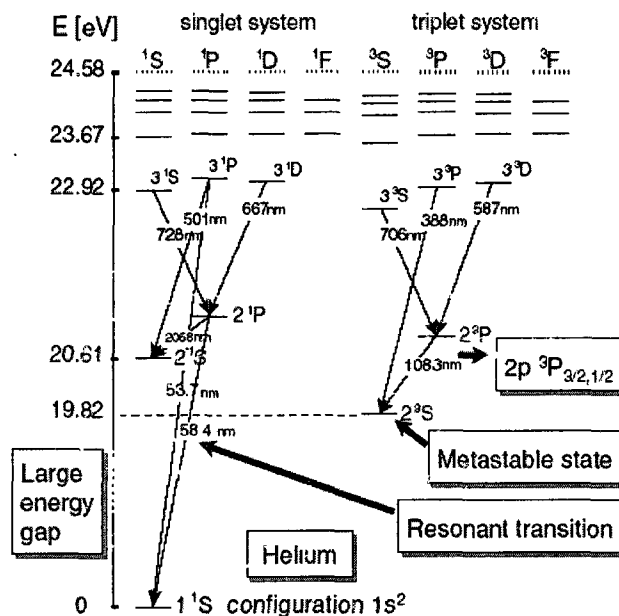


FIG. 50: An example energy level diagram of helium.

from UV spectra about the identity of the working gas.

Since an APLTPJ is operated in the ambient air, the intense emissions of the second positive system (SPS) of  $N_2$  and the first negative system (FNS) of  $N_2^+$  are present along with  $NO$  and  $OH$  bands covering UV spectrum between 200 nm to 466 nm for all working gases (Figure 51). This air entertainment of the plasma jet always plays an important role. The intensity level of these peaks could be controlled (stronger or weaker depending on the application perspective) by changing the gas composition, the magnitude of the applied voltage pulse, the pulse width, the repetition rate, and the flow rate. Although helium has a transition at 389 nm, this peak is overlapped by the rotational levels of FNS in pure helium. This peak only appears when the FNS of  $N_2^+$  becomes weaker, such as in helium/oxygen mixture (Figure 51.b)

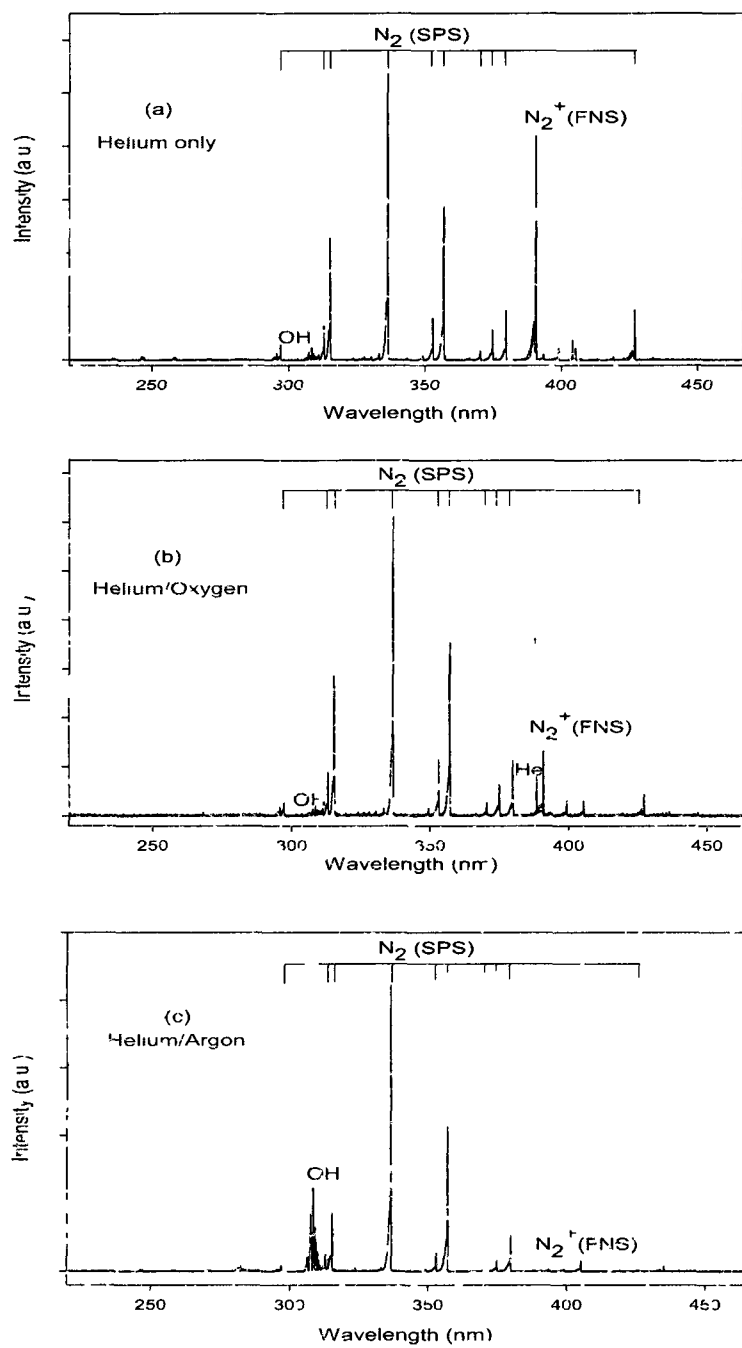


FIG 51 General spectra of UV wavelength range for pure helium, helium/oxygen, and helium/argon mixtures



### 391 nm transition of the $N_2^+$ first negative system (FNS)

The presence of this transition is the most important evidence showing the crucial role of helium metastables. 391 nm transition of FNS appears due to Penning ionization and the charge transfer reactions of RH7 and RH9 in Table 5 [69, 71, 74]:

- RH7:  $He^m + N_2 \longrightarrow N_2^+(B^2\Sigma_u^+) + He + e$
- RH9:  $He_2^+ + N_2 \longrightarrow N_2^+(B^2\Sigma_u^+) + 2He.$

These reactions are known to be almost resonant. For direct electron excitation of  $N_2^+$ , electron energies need to be more than  $E_{threshold} = 18.7$  eV and  $E_{threshold} = 3.17$  eV for the ground state of  $N_2$  and  $N_2^+$ , respectively [75]. However, the electron energies are found to be in the order of 1-3 eV in low temperature plasma jets [76]. The presence of  $N_2^+$  states that helium metastables undergo collisions with molecular nitrogen.

The metastable levels of helium ( $He^m$ ) can be produced by direct electron-atom collisions ( $E_{threshold} = 19.52$  eV), cascade transitions from higher lying states, and dissociative recombination of RH14 between molecular helium ions and low energy electrons [69]. Accordingly, 391 nm line of  $N_2^+$  is most likely populated by the collisions between helium metastables and  $N_2$  molecules.

391 nm line of  $N_2^+$  is clearly visible for both helium only and helium/oxygen mixtures (Figure 51.a and 51.b). However, in helium/argon mixture  $N_2^+$  emission is almost completely quenched. This is probably due to low energy levels of argon metastables.

### 337.1 nm emission of the $N_2$ second positive system (SPS)

This transition ( $C^3\Pi \rightarrow B^3\Pi$ ) of  $N_2$  exists for all working gas compositions (Figure 51). This state can be populated through electron collision ( $E_{threshold} = 11$  eV) or radiative decay of  $N_2^+$ .

### $OH(X-X)$ radical transitions around 310 nm

$OH$  radical emission lines can be observed between 306 nm and 312 nm. The dissociation of water molecules forms these  $OH$  radicals around the plasma jet environment in the ambient air. In order to study  $OH$  emission lines, the relative humidity and

temperature of the room should be controlled since the concentration of water vapor could vary in time.

#### ***NO<sub>γ</sub>* emission lines between 230 nm and 290 nm wavelength ranges**

*NO<sub>γ</sub>* emission bands can be seen between 230 nm and 290 nm along the plasma jet (Figure 52). The intensity levels of these *NO<sub>γ</sub>* lines remain very low in comparison with SPS and FNS. Usually *NO<sub>γ</sub>* systems are usually very intense due to their high transition probabilities. However, in our plasma jets, *NO* concentration level seems to be very low due to these very low intensities of *NO<sub>γ</sub>* lines. *NO* concentration is estimated to below 1 ppm based on a dedicated gas detector measurement. It is interesting to note that oxygen admixture completely quenches *NO<sub>γ</sub>* bands (Figure 52.b) These concentration levels are unlike that of radio-frequency capacitively coupled plasma jets [77, 78].

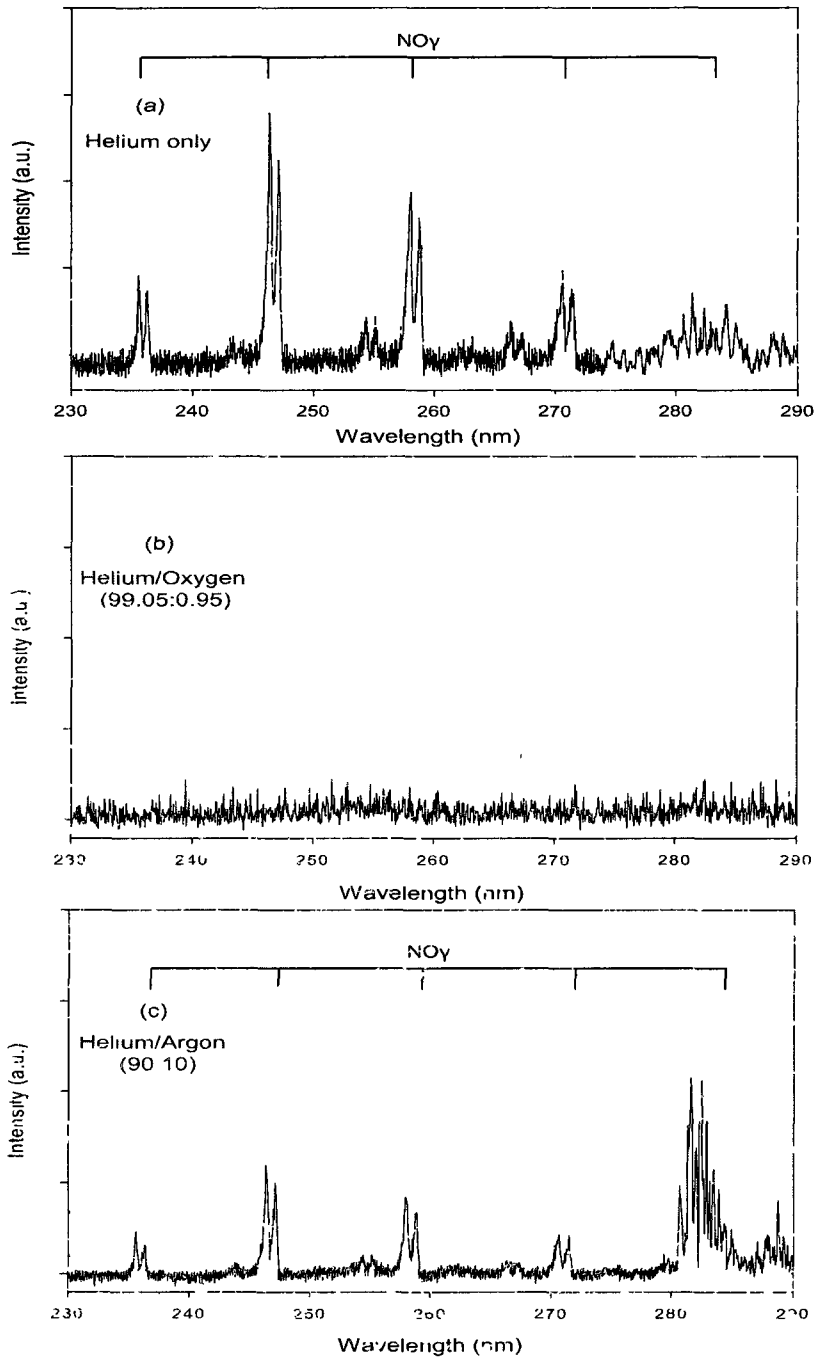


FIG. 52: NO lands between 230 nm and 290 nm for pure helium, helium/oxygen, and helium/argon mixtures

### V.1.3 Argon admixture effect on the helium plasma jet

Argon admixture effect on the helium plasma jet is investigated. It is found that argon admixture dramatically changes the plasma jet chemistry. The total flow rate is kept at a constant value of 5 L/min since higher flow rates bring the gas channel to the turbulent flow regime. Therefore, the experiments are performed in the laminar flow regime. Helium flow rate is decreased from 100% to 0%, and argon flow rate is increased from 0% to 100%, respectively. Experimental parameters were set to 9 kV applied voltage, 2  $\mu$ s pulse width, 5 kHz repetition rate, 5.0 L/min flow rate. The monochromator was focused at 10 mm and 20 mm axial positions of the plasma jet with a 200 ms acquisition time

Figure 53 shows the intensity change of excited species at 10 m and 20 mm axial positions as a function of argon admixture. As seen in this figure, even a small amount of argon admixture completely changes the plasma chemistry. For example, 5% argon admixture significantly intensifies SPS line of  $N_2$  at 337 nm,  $OH(A - X)$  line at 308 nm, and argon line at 750 nm. On the other hand, FNS of  $N_2^+$  line at 391 nm, helium line at 706.5 nm, and oxygen line at 777.1 nm are almost completely quenched by 5% argon admixture. Up to 35% argon, an increase in argon admixture leads to lower values of the emission lines in UV and visible-IR spectra. At 40% argon admixture, SPS line of  $N_2$  at 337 nm and  $OH(A - X)$  line at 308 nm start rising again to relatively lower values of the first maximum while other lines keep decreasing. This especially states that the dissociation of water molecules directly follows SPS line of  $N_2$ . It is worth noting that no increase is observed in the emissions of FNS line of  $N_2^+$  at 391 nm, helium line at 706.5 nm, and oxygen line at 777.1 nm with argon admixtures.

These changes in the chemistry make huge contributions to our knowledge about the chemical behavior of the plasma bullet. As briefly discussed in section V.1.3, due to energy levels of argon atoms and nitrogen molecules, high density of nitrogen metastables, such as  $N_2(A^3\Sigma_g^+)$ ,  $N_2(a^1\Pi_g)$ , and  $N_2(a^1\Sigma_u^-)$  could be formed [68]. In addition, an argon flow system containing argon metastables ( $Ar(^3P_{2,0})$ ) undergoes collisions with nitrogen molecules, and cause the excitation of  $N_2(C^3\Pi_u)$  [79]. Based on Figure 53 an increase in SPS line of  $N_2$  at 337 nm states that the interaction of argon metastables with nitrogen molecules giving the radiative transition of  $N_2$  from  $C(^3\Pi_u) \rightarrow B(^3\Pi_g)$  have a more important role than the stepwise ionization producing nitrogen metastables. This observation is also supported by the reduction of FNS

line of  $N_2^+$  at 391 nm. As seen in Figure 53, even a small amount of argon admixture almost completely depopulates FNS line of  $N_2^+$  at 391 nm. This asserts that the stepwise ionization by nitrogen molecule metastables becomes a weak process in our plasma jet. On the other hand, the energy level of argon metastables is too low to produce FNS of  $N_2^+$  at 391 nm (see Table 7).

Helium line intensity at 706.5 nm decreases as argon admixture increases (Figure 53). The excitation and ionization energy levels of helium are much higher than that of argon. Hence, energy injected into the plasma jet is more likely transferred to argon atoms than helium atoms. Although there is a decrease in helium line, the line intensity does not completely disappear with the argon admixture; rather, it remains at very low values. Oxygen line intensity at 777.1 nm follows this decrease of helium line. This demonstrates that oxygen atoms can be excited by higher energies deposited into helium metastables.

It is worth noting that SPS line of  $N_2$  at 337 nm and  $OH(A - X)$  line at 308 nm decrease with an exception of an increase at 40% argon admixture as argon concentration increases in the flowing gas. More interestingly, the argon line at 750 nm also shows the same pattern. This especially states that more argon atoms do not cause more argon line intensity emissions; however, argon line intensity at 750 nm experiences a maximum at a certain value (in our case 5% argon). In addition, this change in the plasma chemistry does not solely depend on argon concentration in helium flowing gas but also the ratio between argon atoms and nitrogen molecules.

Argon admixture effect experiments are also carried out for different axial positions of 10 mm and 20 mm. This is a required investigation because the ratio between helium/argon mixture and air molecules changes along the axis of the plasma jet. As seen in Figure 53, at 20 mm axial position, even though all emission line intensities follow a similar pattern with 10 mm-axial position, the intensities of the emission lines decay a little faster than those of 10 mm. Accordingly, SPS line of  $N_2$  at 337 nm jumps up to its second maximum from lower values. It is noteworthy that relative intensities of all emitting species at 10 mm are about 2X times more than that of 20 mm.

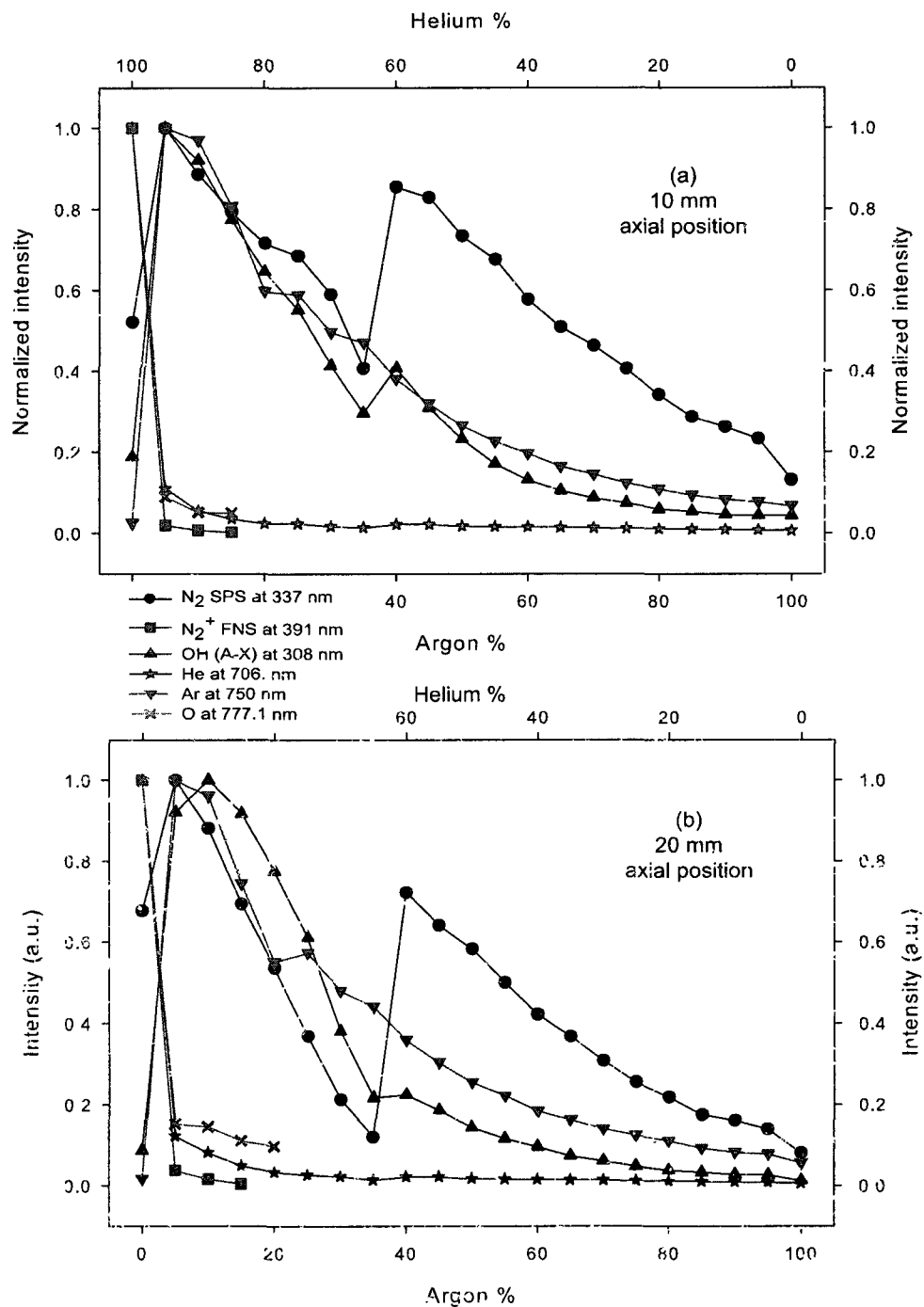


FIG. 53. Argon admixture effect on the intensities of the emitting species. The total flow rate is kept at a constant value of 5 L/min. (applied voltage: 9 kV; pulse width: 2  $\mu$ s, repetition rate: 5 kHz).

## V.2 EFFECTS OF THE EXPERIMENTAL PARAMETERS ON EXCITED SPECIES

In this chapter, the influence of different experimental parameters on excited species for pure helium is investigated by varying the applied voltage, the pulse width, the frequency, and the flow rate. During these experiments, optical emission spectroscopy (OES) is used with appropriate double-convex UV-grade lenses and filters.

The focal point of the monochromator is fixed at 20 mm away from the reactor nozzle. Specifically, the behaviors of five important excited species are studied: SPS of  $N_2$  at 337 nm, FNS of  $N_2^+$  at 391 nm,  $OH(A-X)$  at 308 nm, He ( $2^3P \rightarrow 3^3S$ ) at 706 nm and O ( $3^5S \rightarrow 3^5P$ ) at 777 nm.

Although the OES system is not calibrated for irradiance, the evolution of emission lines provides an estimation on the variation of active species production along the plasma jet. Therefore, the intensity  $I(A^*)$  of a transition from an excited species is proportional to the radiative state density  $n(A^*)$ .

### V.2.1 Applied voltage pulse

The emission intensities of the chosen lines are shown in Figure 54 as a function of different applied voltage (HV) pulse amplitudes. As the HV pulse amplitude increases, the energy injected into the ionization channel increases; therefore, the line intensities of all excited species increase as in the gas discharges. For HV amplitudes less than 6.5 kV, line intensities are close to zero level because the length of the plasma jet is shorter than 20 mm, the focal point of the monochromator. For HV amplitudes higher than 6.5 kV, the line intensities of  $N_2$ ,  $N_2^+$ , and  $He$  especially follow a very similar pattern (almost linear). On the other hand,  $OH(A-X)$  and  $O$  also resemble  $N_2$ ,  $N_2^+$ , and  $He$  with fewer increase ratios.

It is very important to note that the volume of the plasma bullet expands with higher HV amplitudes. Therefore, the power of the light collected from the focal point also increases due to this expansion.

### V.2.2 Pulse width

The pulse width of the HV amplitude is varied from 200 ns to 4  $\mu s$ . The effect of the pulsed width on the radiative properties of the plasma jet is shown in Figure 55. As stated in section IV.2, the plasma bullet comes to an end due to either the

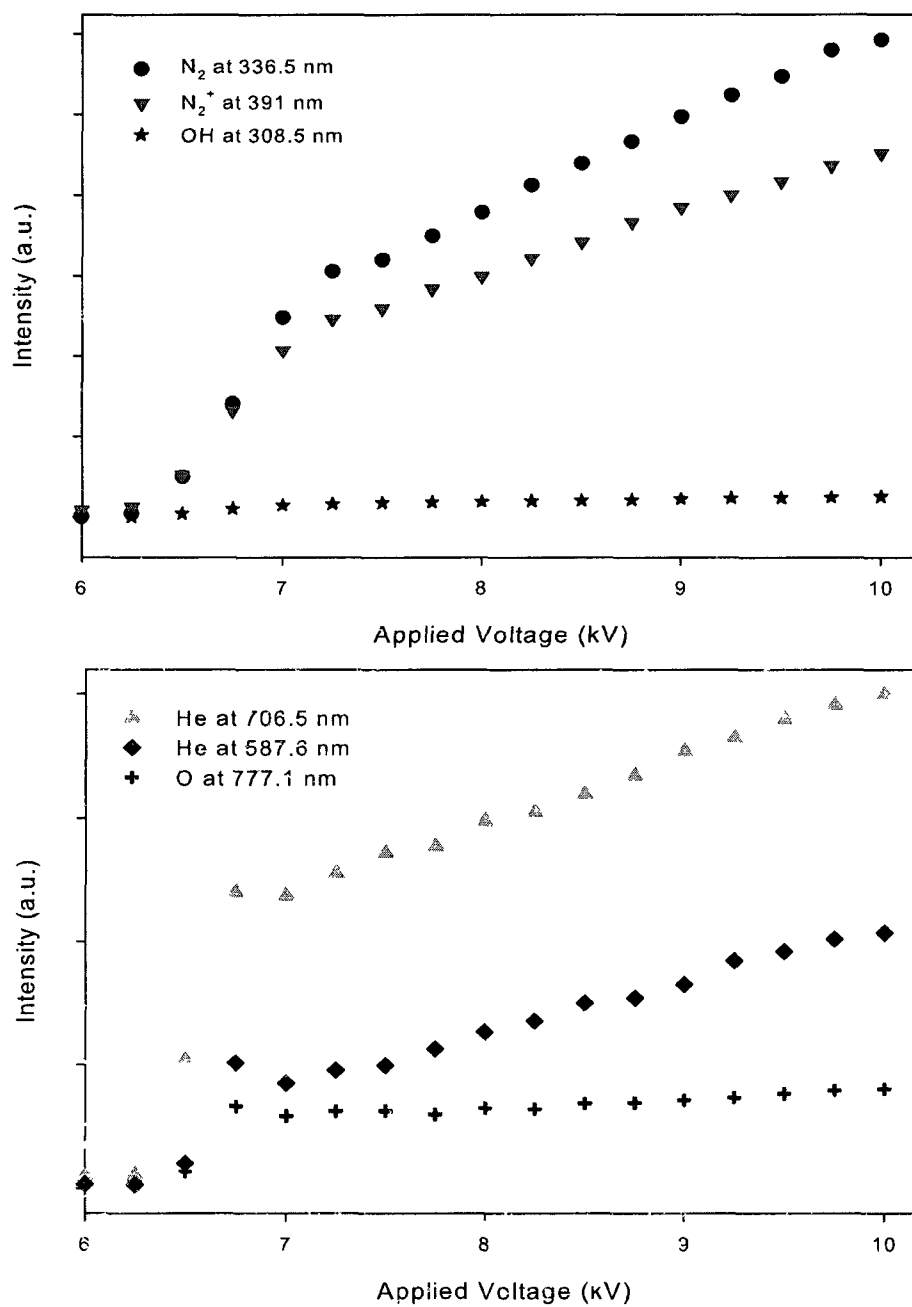


FIG. 54: Emission line intensities of the emitting species as a function of the HV pulse amplitude (pulse width:  $2 \mu s$ ; repetition rate: 5 kHz; flow rate: 5.0 L/min).



secondary discharge ignition or low helium mole fraction in the ionization channel. In order to study the pulse width effect on the radiative properties, the secondary discharge ignition effect should be taken into consideration.

As seen in Figure 55, the intensities of the emitting species quickly go up for the lower pulse width less than 900 ns. This is the zone where the secondary discharge ignition is effective. For this reason, excited states in the plasma bullet emit less intensities for this shorter pulse widths because the plasma bullet extinguishes before the emitting species reach an equilibrium. For pulse width longer than 900 ns, low helium mole fraction in the ionization channel causes the inhibition of the plasma bullet. In this zone, an increase in the pulse width does not affect the line intensities of the emitting species. Indeed, higher pulse width values result in slightly lower radiation values. This is due to the energy loss of the plasma bullet during its propagation and electron attachment by air molecules as it propagates forward.

### V.2.3 Repetition rate (Frequency)

The repetition rate is varied from 1 kHz to 10 kHz. The integration time of the OES system is adjusted to 200 ms during experiments. Therefore, an emission intensity value of a specific repetition rate sums up intensities of all plasma bullets launching from the reactor during 200 ms. Not surprisingly, an increase in repetition rate leads to an increase in emission intensities of the excited species (Figure 56). In the application point of view, the repetition rate value is important to determine the number of plasma bullets that will come into contact with the sample per unit time.

### V.2.4 Flow rate

The emission line intensities of the plasma jet are shown in Figure 57 as a function of the flow rate. The flow rate is varied from 0.2 L/min to 6 L/min. Up to 1.6 L/min, the amount of the feed gas affects linearly the emission intensities of all excited species. For flow rates higher than 1.6 L/min,  $N_2$ ,  $OH$ , and  $O$  intensity levels remain relatively constant. However,  $N_2^+$  and  $He$  emission intensities keep increasing linearly with the flow rate. This observation also supports the Penning ionization mechanism explanation: more helium atoms produce more helium metastables causing the excitation and the creation of  $N_2^+$  ions.

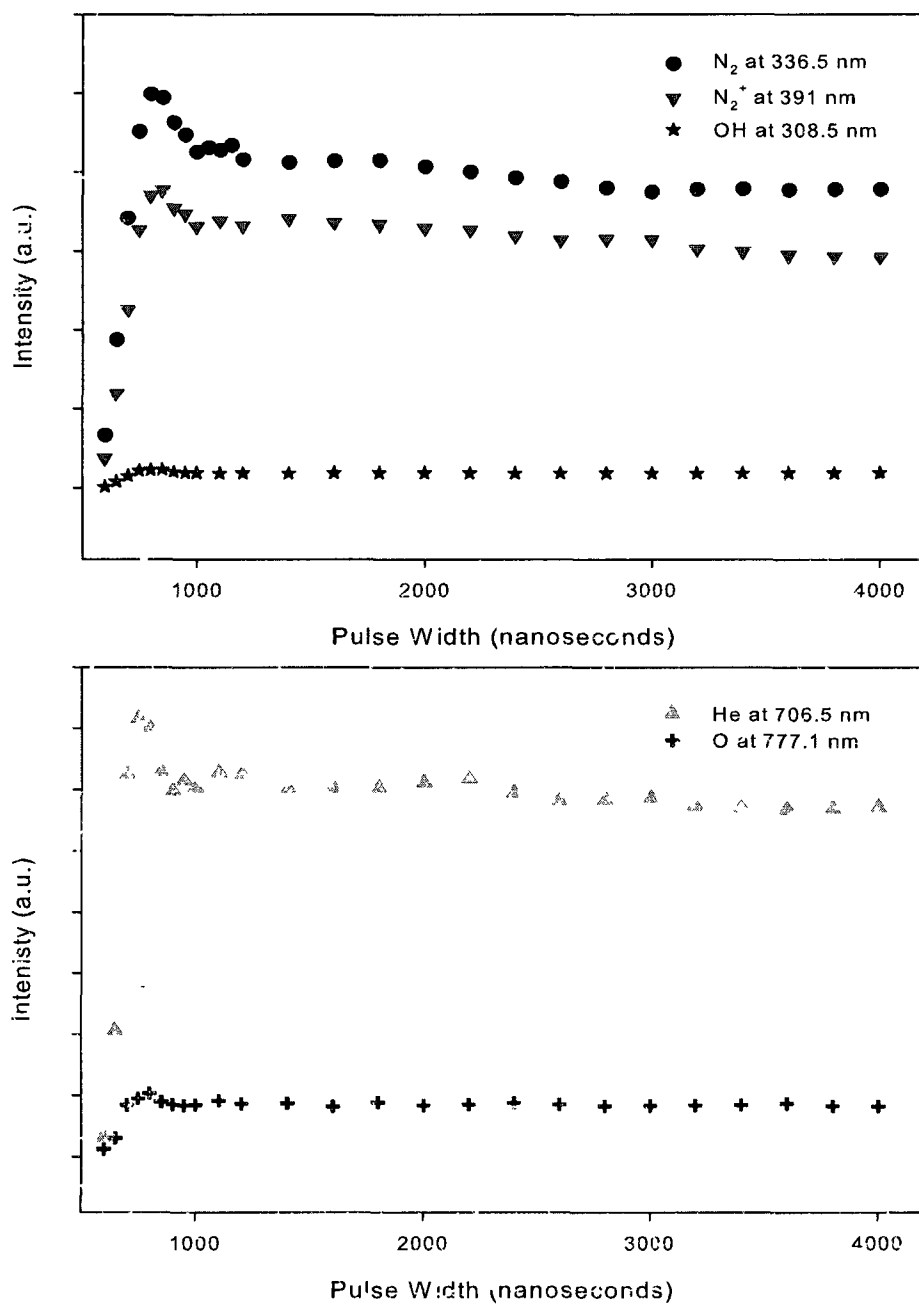


FIG. 55: Emission line intensities of the emitting species as a function of the pulse width (applied voltage: 9 kV; repetition rate: 5 kHz; flow rate 5.0 L/min).

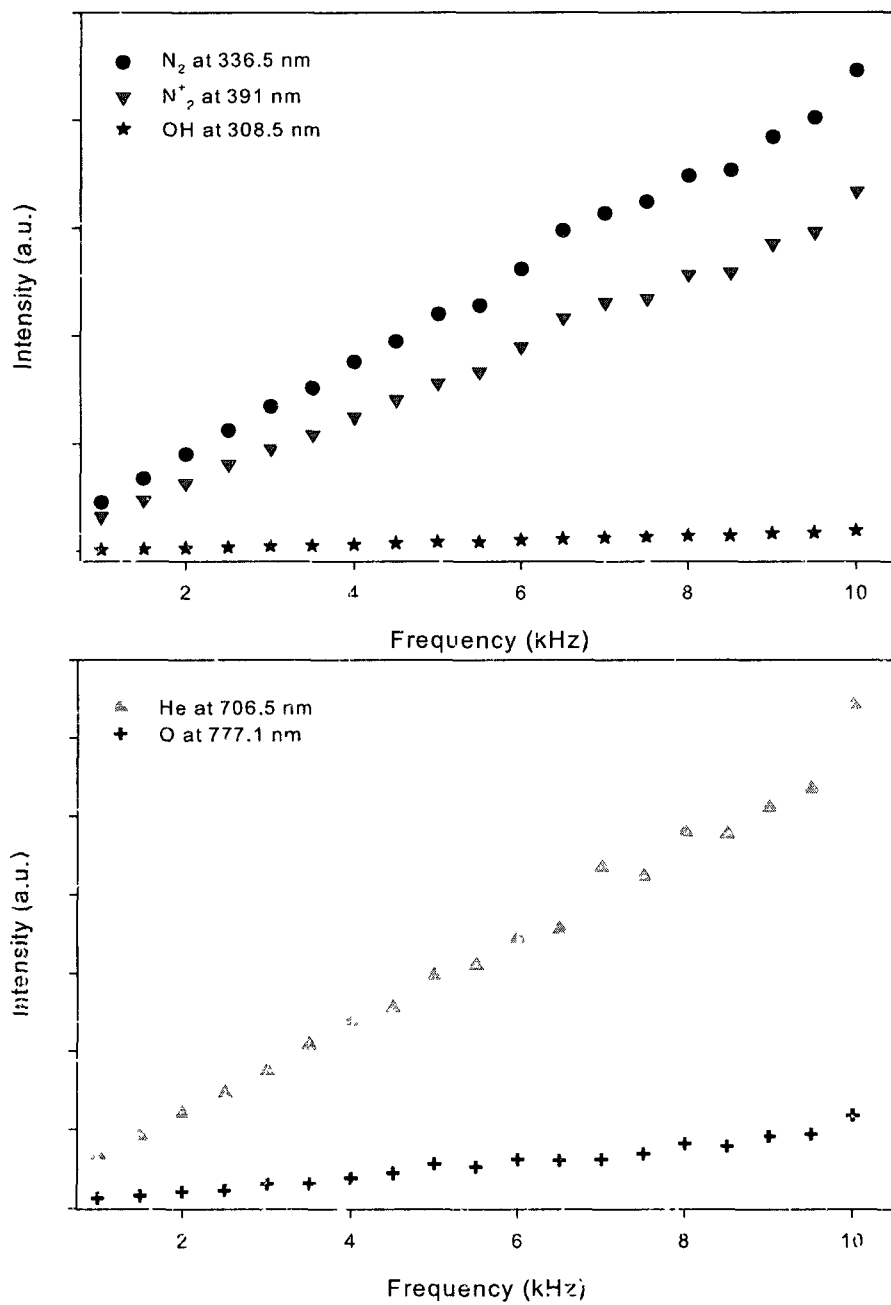


FIG. 56: Emission line intensities of the emitting species as a function of the frequency (applied voltage: 9 kV; pulse width: 2  $\mu$ s; flow rate: 5.0 L/min).

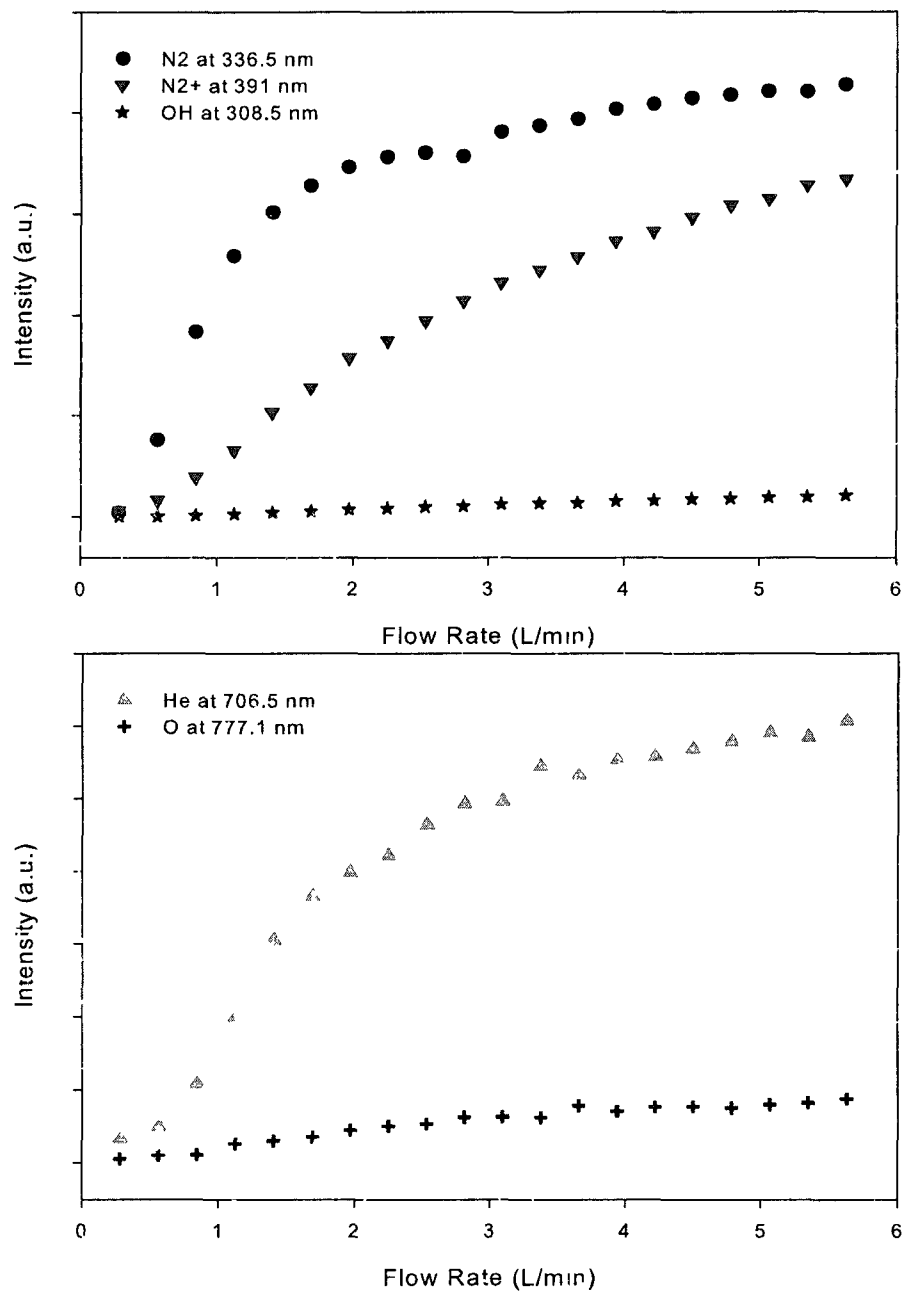


FIG. 57: Emission line intensities of the emitting species as a function of the flow rate (applied voltage: 9 kV; pulse width: 2  $\mu$ s; repetition rate: 5 kHz).

### V.3 SPATIO-TEMPORALLY RESOLVED DISTRIBUTIONS OF EXCITED SPECIES

#### V.3.1 Spatial behavior

The visible appearance of the plasma jet is, in fact, the footprint of the plasma bullet. The variation of the plasma bullet chemical makeup during its propagation, and air diffusing into it are highly important factors in elaborating its structure and dynamics.

Spatially resolved OES spectroscopy along the plasma jet axis is shown in Figure 58. All emitting species experience their maxima around 12 mm.  $N_2^+$  and  $He$  emission lines decay faster while  $N_2$  line almost remains at its maximum point for about 20 mm. On the other hand,  $N_2^+$  and  $He$  emission intensities resemble to each other as explained by Penning ionization mechanism.

Especially,  $N_2^+$  and  $He$  spatially resolved intensities show an interesting pattern. They follow the instantaneous plasma bullet velocity curve (Figure 21) [11]. This finding also indicates that helium metastables play a key role in the plasma bullet propagation.

$OH$  and  $O$  levels remain at relatively lower values during the plasma bullet propagation. The spatially resolved curve of  $OH$  especially resembles that of  $N_2$ ,  $O$ , and  $N_2^+$ .

#### V.3.2 Temporal behavior

The temporal behavior of excited species in the plasma bullet is investigated in Figure 59 for pure helium and helium/argon (95:5) mixture at 20 mm axial position of the plasma jet. This figure provides us an opportunity to better understand the kinetic mechanism of the plasma bullet during its propagation. These excited species include  $N_2$  SPS at 337.1 nm (Figure 59.a),  $N_2^+$  FNS at 391.4 nm (Figure 59.b),  $OH(A-X)$  at 308 nm (Figure 59.c), helium line at 706.4 nm (Figure 59.d), and argon line at 750 nm (Figure 59.e). During these experiments, the PMT output is connected to a wideband oscilloscope after required diffraction grating adjustments are completed using software.

Emission intensities of excited species quickly rise up to their maxima as soon as the plasma bullet arrives to the focal point of the monochromator. The rising time of the emitting species is around 20 ns while their decay times vary remarkably. It

is worth noting that  $OH(A - X)$  radical exhibits different temporal characteristics in comparison with other excited species.

For pure helium working gas, the lifetime of  $N_2$  SPS at 337.1 nm and  $N_2^+$  FNS at 391.4 nm are longer than that of helium at 706.4 nm. This is mainly due to other kinetic mechanisms involved as explained in the previous sections. In addition, this shorter lifetime of helium indicates that  $He(3^3S)$  is only produced for a few nanoseconds in the discharge. After the first peak decays, a second peak arises with relatively lower intensities. This second peak probably occurs due to thin luminous channel left over as the plasma bullet propagates forward. This luminous channel takes place in the ionization channel partly because of SPS of  $N_2$  and FNS of  $N_2^+$ . These species are known to last more than  $1\mu s$ . It is also observed that the lifetime of  $OH$  radical is much longer than that of other species even though the line intensity is much weaker.

The behavior of helium/argon (95:5) working gas mixture completely differs in intensity and lifetime. As seen in Figure 59 the peak times of excited species are 400 ns faster than that of helium gas. This states the propagation velocity of the plasma bullet is about two times faster in helium/argon (95:5) mixtures. As already known in section V.1.3, this increase in the velocity resembles the increase in the emission intensities with argon admixture. On the other hand, the lifetimes of SPS and  $OH(A - X)$  is much longer than that of pure helium (Figure 59.a and Figure 59.b). Especially,  $OH(A - X)$  radical exists in the ionization channel during the entire duration of the pulse width. Even this 5% argon admixture is high enough to significantly quench FNS at 391 nm and helium line at 706.4 nm. In addition, argon line at 750 nm appears in helium/argon mixtures instead of helium line of 706.5 nm in pure helium. It is also found that the second peak (or bump) only exists for argon line at 750 nm in helium/argon mixtures.

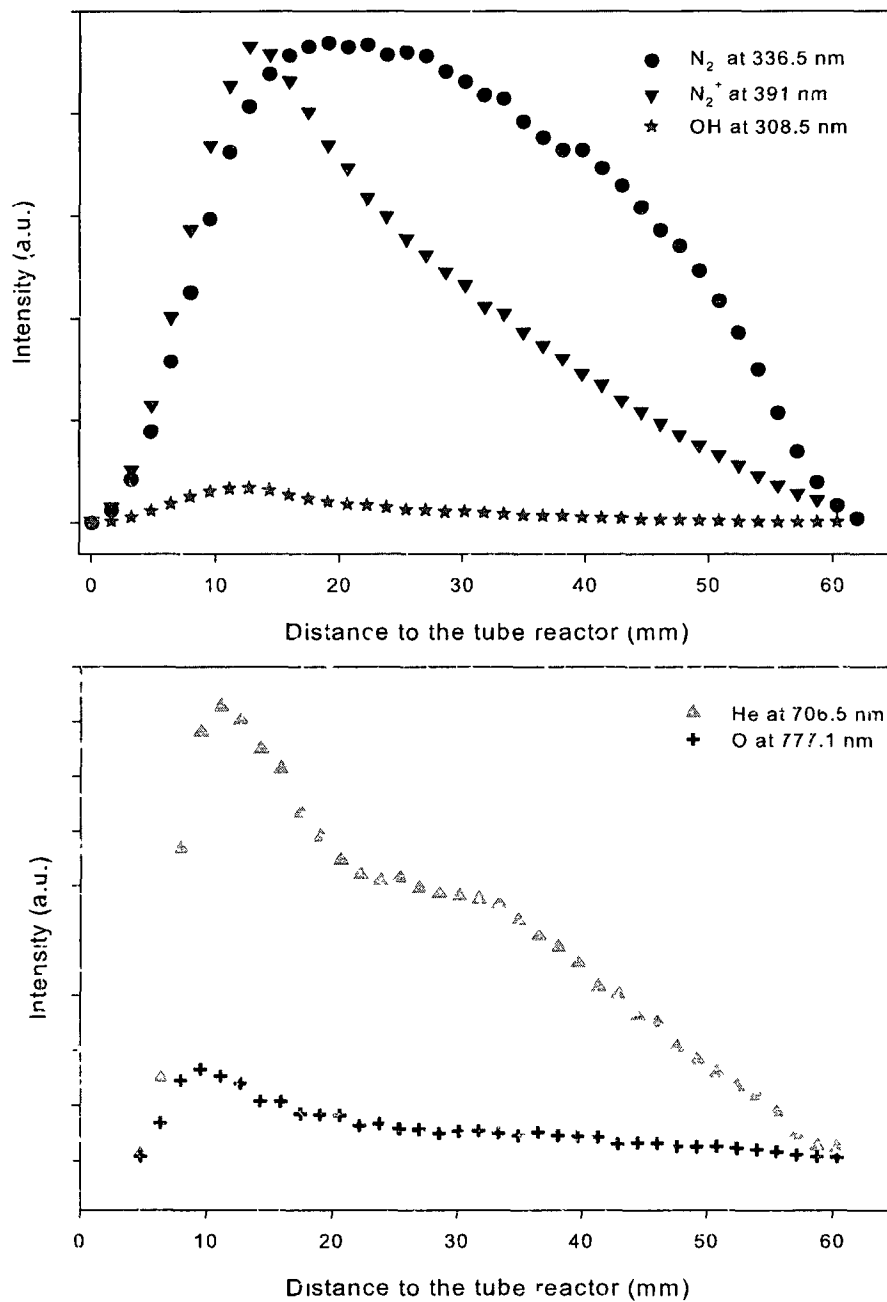


FIG. 58: Spatially resolved emission line intensities of the emitting species. These species reach their maxima around 12 mm away from the reactor nozzle (applied voltage: 9 kV; pulse width: 2  $\mu$ s; repetition rate: 5 kHz; flow rate: 5 L/min).

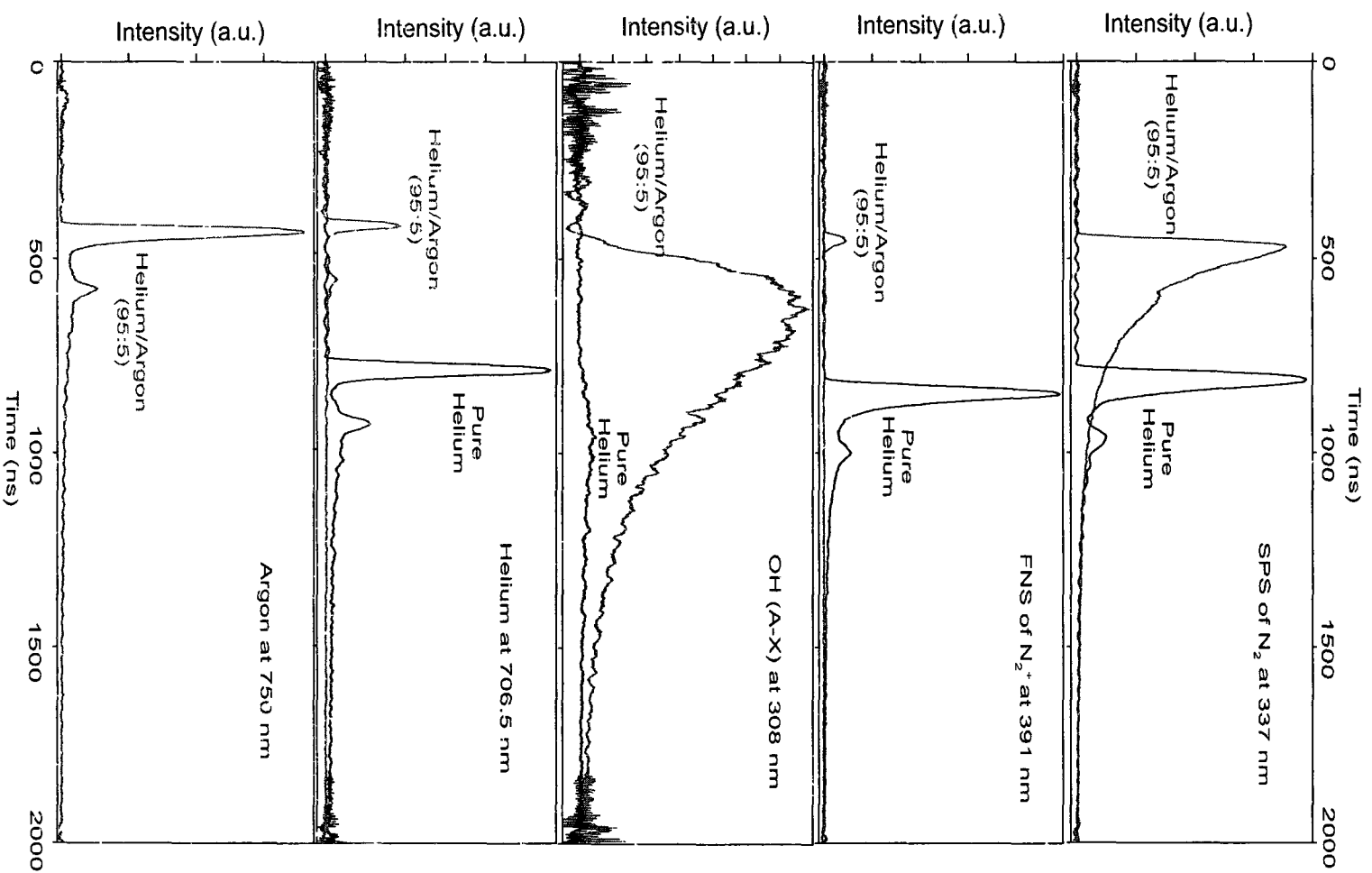


FIG. 59. Temporally resolved emission line intensities of the emitting species (applied voltage: 9 kV; pulse width: 2  $\mu$ s; repetition rate: 5 kHz; flow rate: 5 L/min).



## V.4 RADIAL PROFILES OF THE PLASMA BULLET

Based on several experimental observations, it was revealed that the plasma bullet has a donut-shaped structure [11, 12, 57]. The emitting species of the plasma bullet accumulate more on the edge of the plasma bullet (the perimeter of the plasma bullet). Due to its three dimensional structure, the observation of this donut-shaped plasma bullet is not always an easy task. The cavity at the center of the plasma bullet hides behind the surface emission on the camera direction. However, the radial emission profiles provide insights regarding the donut-shaped structure of the plasma bullet. Emission intensities of the radial profiles indicate that the edge of the plasma bullet has a higher emission intensity than that of the center (Figure 61.a, Figure 62.a, Figure 63.a, Figure 64.a).

Abel inversion is a tool to convert the chordal measurements to the radial distributions. It is worth noting that the emission should be symmetrical across the surface of the plasma bullet in order to apply the Abel inversion. This mathematically indicates that the chordal measurements are independent of  $\theta$  and  $z$  in a cylindrical coordinate system  $(r, \theta, z)$ . Accordingly, the Abel inversion can be described as follows: let the emission intensity across the surface of the plasma bullet be defined as  $F(y)$ :

$$F(y) = \int_{-((a^2-y^2)^{1/2})}^{+((a^2-y^2)^{1/2})} f(r) dx \quad (12)$$

where  $f(r)$  is the radial profile of the plasma bullet. The  $x$  integral can be changed by an  $r$  integral as follows ( $r^2 = x^2 + y^2$ ):

$$F(y) = \int_y^a f(r) \frac{r dr}{(r^2 - y^2)^{1/2}} \quad (13)$$

The inverse transform leads to the radial distribution of the plasma bullet:

$$F(r) = \frac{-1}{\pi} \int_r^a \frac{dF}{dy} \frac{dy}{(y^2 - r^2)^{1/2}}. \quad (14)$$

The radial profiles of the plasma bullets are determined for different experimental parameters as seen in Figure 61.a, Figure 62.a, Figure 63.a, and Figure 64.a. The focal point of the monochromator was first fixed at a constant axial-position on the plasma jet, and then it was radially moved over the surface of the plasma bullet by an adjustable micrometer. Acquisitions were performed for each 0.2 mm interval. The

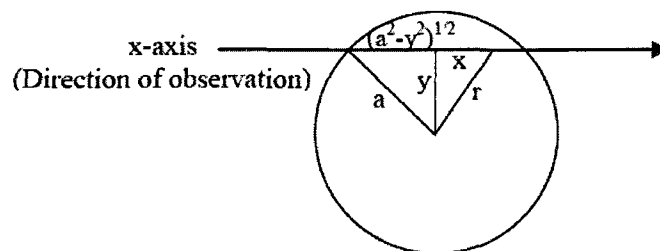


FIG. 60: Chordal measurement in the cylindrical coordinates.

experimental parameters were as follows: 8 kV applied voltage;  $2 \mu s$  pulse width, 5 kHz repetition rate, 5.0 L/min flow rate. The integration time of the monochromator was set to 200 ms (i.e.  $10^5$  plasma bullets for each acquisition). First, the radial distributions of excited species ( $N_2$  SPS at 337.1 nm,  $N_2^+$  FNS, and helium line at 706.4 nm) are investigated, and then  $N_2$  SPS at 337.1 nm are employed to observe the effects of experimental parameters on the radial profiles. This line is chosen due to its strong emission.

Abel inverted profiles are obtained by the Abel integral. The experimental profiles are inserted into a MATLAB code as a matrix, and then the integral is numerically solved in a matrix form.

Figure 61 shows the radial emission profiles of  $N_2$  SPS at 337.1 nm,  $N_2^+$  FNS at 391 nm and helium line at 706.4 nm at 10 mm axial position. Even though these three excited species radially exhibit similar behavior, the emission intensities at the center and on the edge differ in their intensities. This observation is also confirmed by Abel inverted profiles (Figure 61.b). In this figure, SPS emission at the center of the plasma bullet is almost zero while helium line emission reaches relatively higher values (2X). This higher emission of helium line can be easily explained by higher helium mole fraction at the center of the plasma bullet at 10 mm due to the presence of helium gas channel. On the other hand, it is found that FNS emission is 4 times greater than that of SPS. This high intensity of FNS refers the Penning ionization mechanism because the center of the plasma bullet is where helium metastable concentration and the helium atom mole fraction is higher [56] due to the helium gas channel [55].

Radial profiles of  $N_2$  SPS emission intensity at 337.1 nm are given in Figure 62

for axial positions of 10 mm, 20 mm, 30 mm, and 40 mm. These radial profiles show that emission intensities at the center of the plasma bullet are weaker than those of the edges. After Abel inversion is applied to the experimental profiles, it is found that the center of the plasma bullet is, in fact, null at 10 mm and 20 mm axial positions. However, both 30 mm and 40 mm axial positions of radial profiles indicate a stronger emission at the center. This states that the plasma bullet has a donut (or ring)-shaped structure, and it collapses towards its center as it propagates forward. Figure 62 also shows that the diameter of the plasma bullet becomes narrower as the plasma bullet reaches further axial distances.

As discussed in the previous sections, the magnitude of the applied voltage pulse affects the velocity and the diameter of the plasma bullet and the emission intensity of the emitting species. Similar results are also obtained for the radial profiles at 10 mm axial position. As seen in Figure 63.a, the diameter of the plasma bullet and emission intensity of  $N_2$  SPS at 337.1 nm become larger with an increase in the applied voltage pulse. The Abel inverted profiles (Figure 63.b) also show that the center of the plasma bullet develops into a real cavity as the applied voltage increases.

In this chapter, the argon admixture effect was already studied in section V.1.3. It was found that the argon admixture significantly changes the chemistry of the plasma bullet (Figure 53). The argon admixture effect is also investigated for radial profiles of  $N_2$  SPS at 337.1 nm (Figure 64). Accordingly, the Abel inverted profiles show that the argon admixture for 10% has a small effect on the emission intensity of SPS at the center of the plasma bullet. It is worth noting that at 10% argon admixture the emission intensity of SPS almost becomes double (Figure 53). However, 20% and 30% argon admixtures cause the filling up the cavity of the plasma bullet at its center (Figure 64.b).

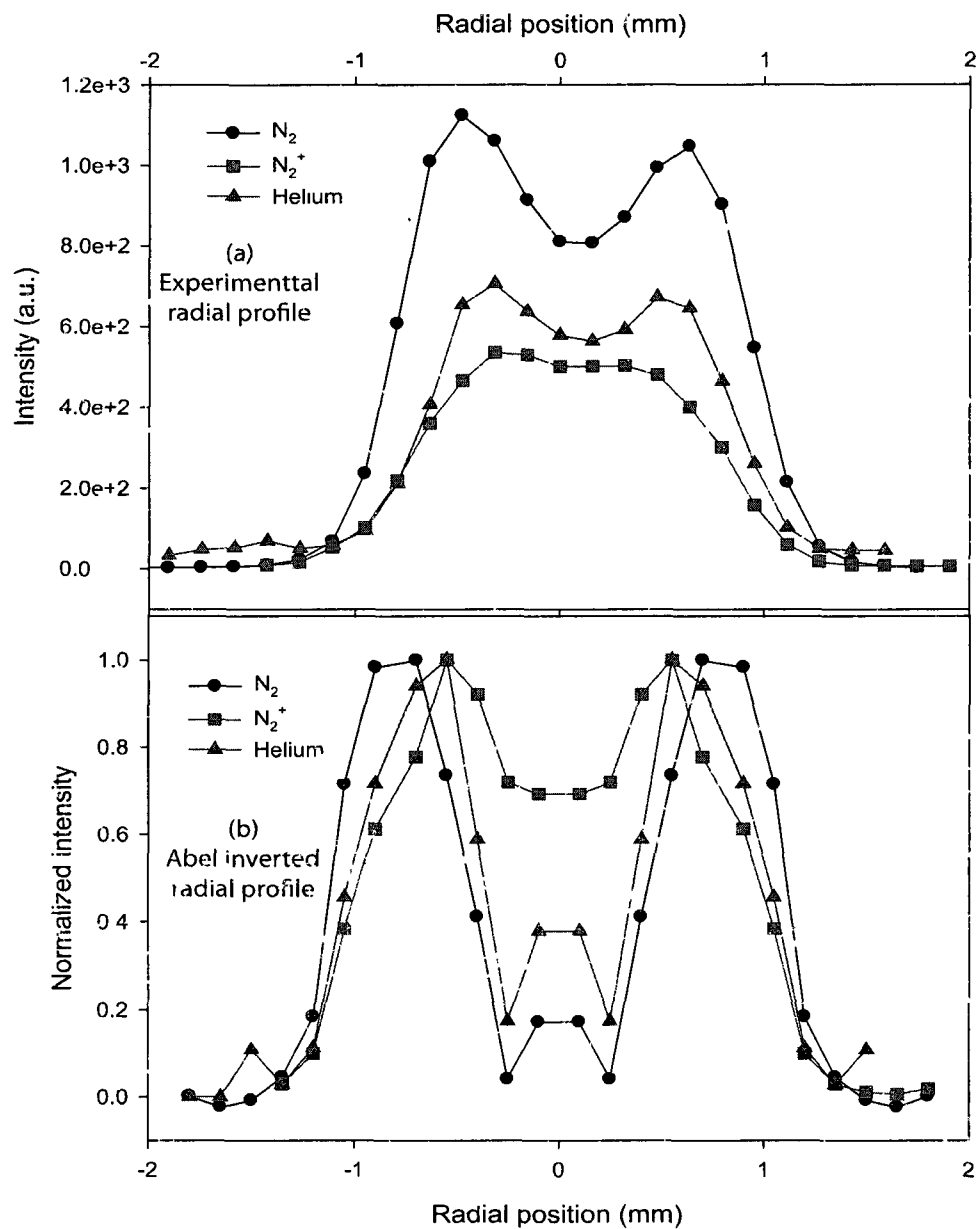


FIG. 61: Radial profiles of excited states for  $N_2$  SPS at 337.1 nm,  $N_2^+$  FNS, and helium line at 706.4 nm at 10 mm axial position: (a) experimental radial profiles; (b) Abel inverted radial profiles (applied voltage: 8 kV; pulse width: 2  $\mu$ s; repetition rate: 5 kHz; flow rate: 5 L/min).  $N_2$  and He lines show almost no emission at the center of the plasma bullet.

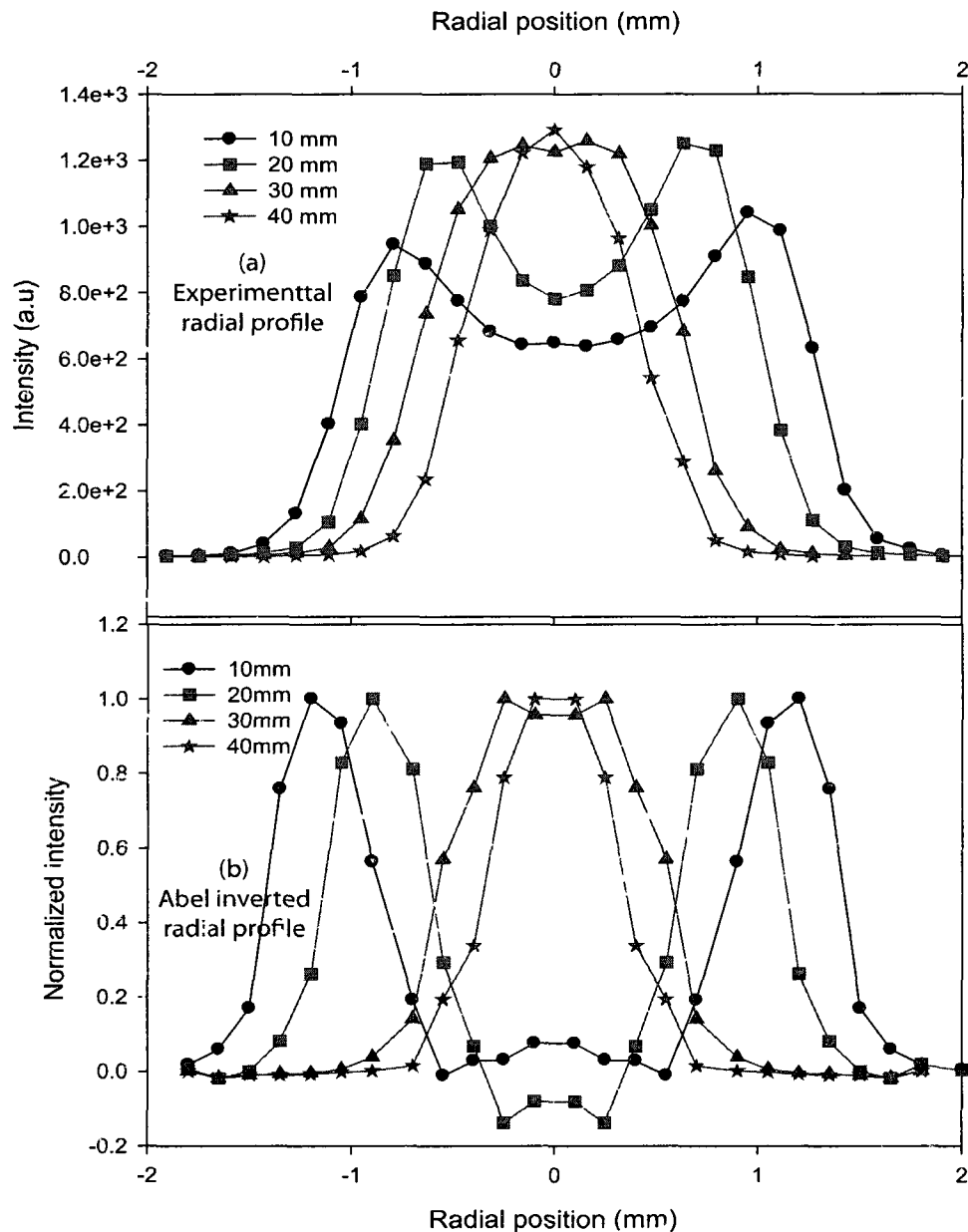


FIG. 62: Radial profiles of  $N_2$  SPS at 337.1 nm for different axial positions (10 mm, 20 mm, 30 mm, and 40 mm) (a) experimental radial profiles; (b) Abel inverted radial profiles (applied voltage: 8 kV; pulse width: 2  $\mu$ s; repetition rate: 5 kHz; flow rate: 5 L/min). The plasma bullet collapses toward its center as it propagates forward.

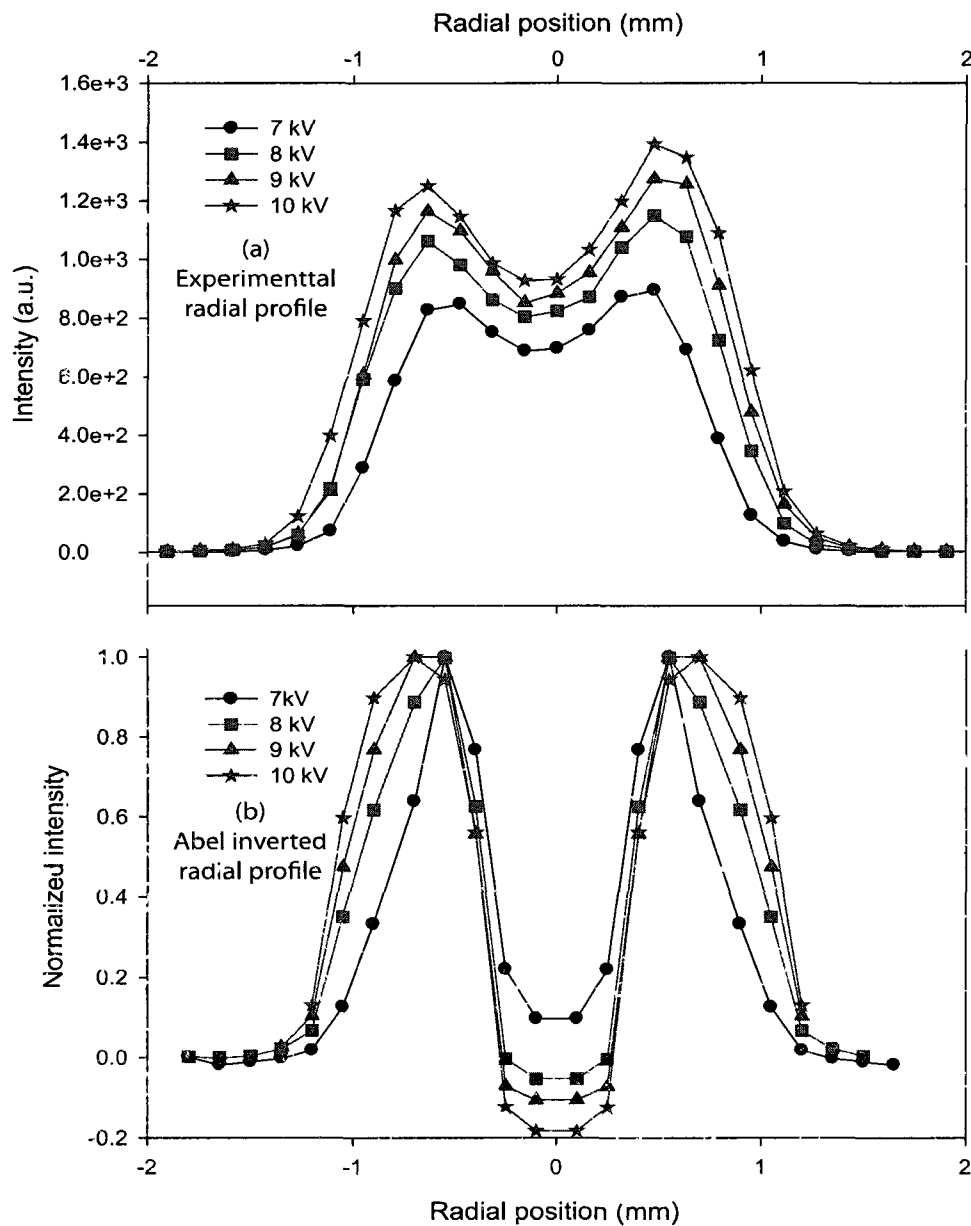


FIG. 63: Radial profiles of  $N_2$  SPS at 337.1 nm at 10 mm axial position for different applied voltages (7 kV, 8 kV, 9 kV, and 10 kV): (a) experimental radial profiles; (b) Abel inverted radial profiles (pulse width: 2  $\mu$ s; repetition rate: 5 kHz; flow rate: 5 L/min). The cavity at the center of the plasma bullet is more distinctive at higher HV pulse amplitudes.

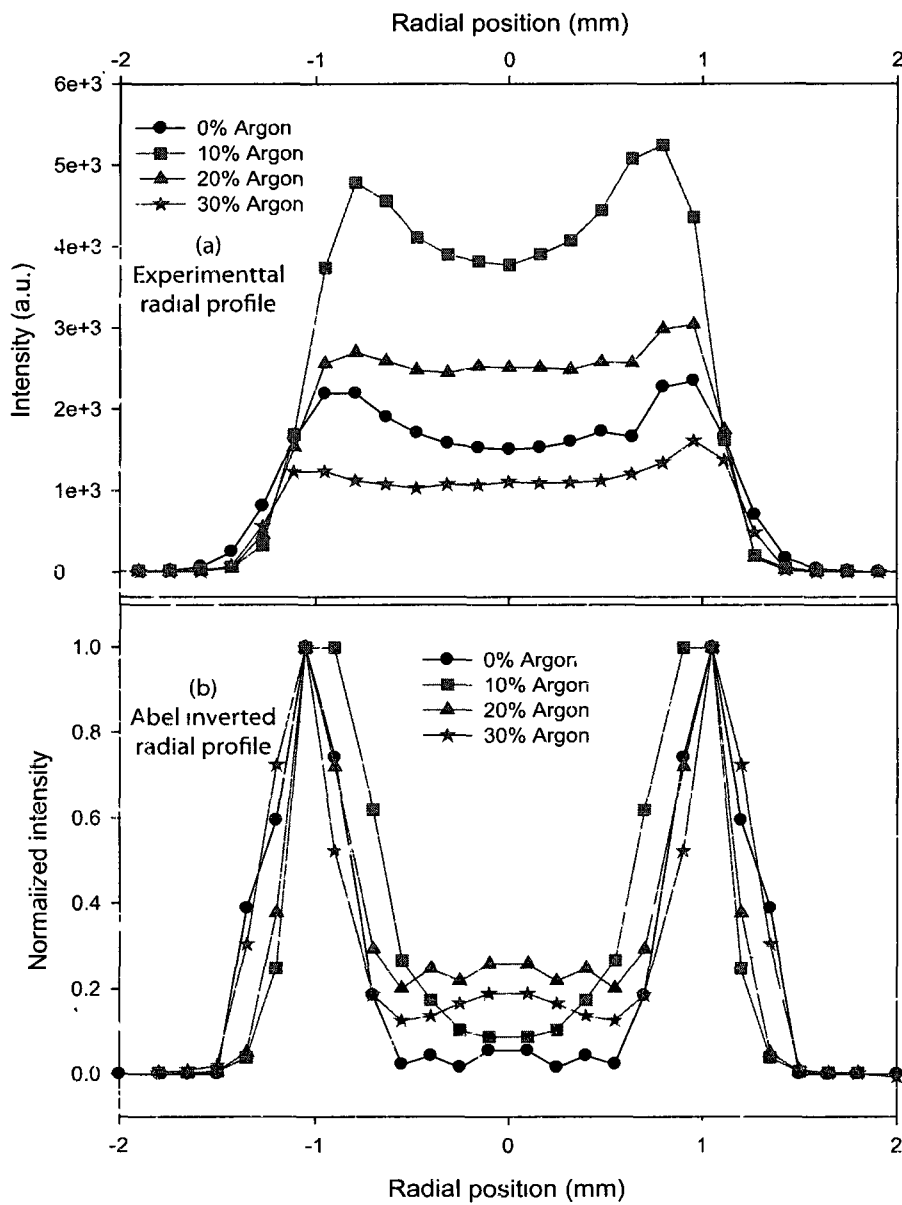


FIG. 64. Radial profiles of  $N_2$  SPS at 337.1 nm for different argon admixtures (0%, 10%, 20% and 30%): (a) experimental radial profiles; (b) Abel inverted radial profiles (applied voltage: 8 kV; pulse width:  $2 \mu s$ ; repetition rate: 5 kHz; flow rate: 5 L/min)

## V.5 ROTATIONAL AND VIBRATIONAL TEMPERATURE

Low temperature plasmas can be classified by their electron temperature ( $T_e$ ), vibrational temperature ( $T_{vib}$ ), rotational temperature ( $T_{rot}$ ), and translational temperature ( $T_{trans}$ ). The order of magnitude of these temperatures in these plasmas is usually  $T_e > T_{vib} > T_{rot} \cong T_{trans}$ . Each electronic state has vibrational levels (quantum number  $v$ ), and each vibrational level splits into rotational levels (quantum number  $J$ ), where rotational levels should follow the selection rules:  $\Delta J = 0, \pm 1$  called the P, Q, and R branches. In addition, a vibrational level of a molecule in the ground state can be excited into electronically upper state via the Frank-Condon principle [80, 81].

The vibrational temperature provides information about the energy transfer from high energy electrons to cold heavy species because the vibrational excited level is created by electron excitation [33]. Stated differently, the value of the vibrational temperature is usually between the gas and electron temperatures.

If inelastic collisions are sufficiently high as in atmospheric pressure plasmas for a particular electronic and vibrational state, the rotational temperature provides valuable insight into the gas kinetic temperature [80, 82, 83]. Since the inelastic collisions are insufficient for low pressure plasmas, the rotational temperature becomes higher than the gas kinetic temperature.

Both the vibrational and rotational temperatures can be obtained from either the Boltzmann plot or a comparison of vibrational bands with simulations of the spectra based on molecular constants. In this section, the comparison method will be employed by a radiative code PASTIS [12], which enables simulation of the emission spectrum of molecular nitrogen in UV, visible, and near-infrared ranges. This radiative code determines the population of the upper state of the transitions as determined by a Boltzmann distribution and the specified temperature of the internal energy mode. The transition probabilities will be calculated by tabulated data for a given set of transitions to determine the upper state populations instead of performing a collisional radiative study [26–80, 82]. For our plasma jet, the following transitions will be used to determine the rotational and vibrational temperatures from 0–0 band and  $\Delta v = -2$  of  $N_2$ , second positive system (SPS) ( $C^3\Pi_u \rightarrow B^3\Pi_g$ ), respectively. Experimental parameters were set to 8 kV applied voltage, 2  $\mu s$  pulse width, 5 kHz repetition rate, and 5 L/min flow rate. The slit width and integration time of the monochromator are adjusted to 40  $\mu m$  and 100 ms.



Figure 65.a [12] shows the simulated spectra of SPS 0 – 0 band in comparison with the experimental spectra. Based on this figure, the experimental spectra is in good agreement with the simulated spectra for  $325K \pm 50K$ . Due to the sufficiently high collision frequency of atmospheric pressure, the gas ( $T_{gas}$ ) and rotational temperatures ( $T_{rot}$ ) are assumed to be equal. For this low temperatures, even though the accuracy of the measurements is limited to  $\pm 50K$ , the rotational temperature results provide insights into the suitability of the APLTPJs for biomedical applications.

Rotational temperature data obtained from 0 – 0 band of SPS is used to determine the vibrational temperature by fitting  $\Delta v = -2$  bands (0-2, 1-3, 2-4) of  $N_2$  into the experimental data. Therefore, the vibrational temperature is found to be  $T_v = 3000 \pm 100K$  [12]. This finding states that the plasma bullet produced by the propagation of the ionization front exhibits highly non-equilibrium characteristics. In addition, the energy injected into the gas channel is mainly dissipated through inelastic collisions including excitation, dissociation and ionization between electrons and gas particles [12]. It is worth noting that the applied voltage amplitude does not affect the rotational and vibrational temperatures of pure helium plasma jets.

Rotational and vibrational temperatures are also studied for helium/argon mixture plasma jets [84]. (0-0) band experimental spectra of SPS for helium/argon mixtures is compared with that of pure helium in Figure 66.a. As seen in this figure, (0-0) band of SPS does not differ in their shapes for 5% argon admixture. This conclusion is also confirmed for 10%, 15%, 20%, 25%, and 30% argon mixtures. However, based on the comparison of  $\Delta v = -2$  bands (0-2, 1-3, 2-4) of  $N_2$  with the simulated spectra, the vibrational temperature is found to have a different behavior for different argon admixtures. Figure 66 b shows experimental and simulated  $\Delta v = -2$  bands of SPS for 5% argon admixture indicating the vibrational temperature is 2900 K. As more argon admixture is injected into the gas channel, the vibrational temperature decreases to as low as 1500 K (Figure 67).

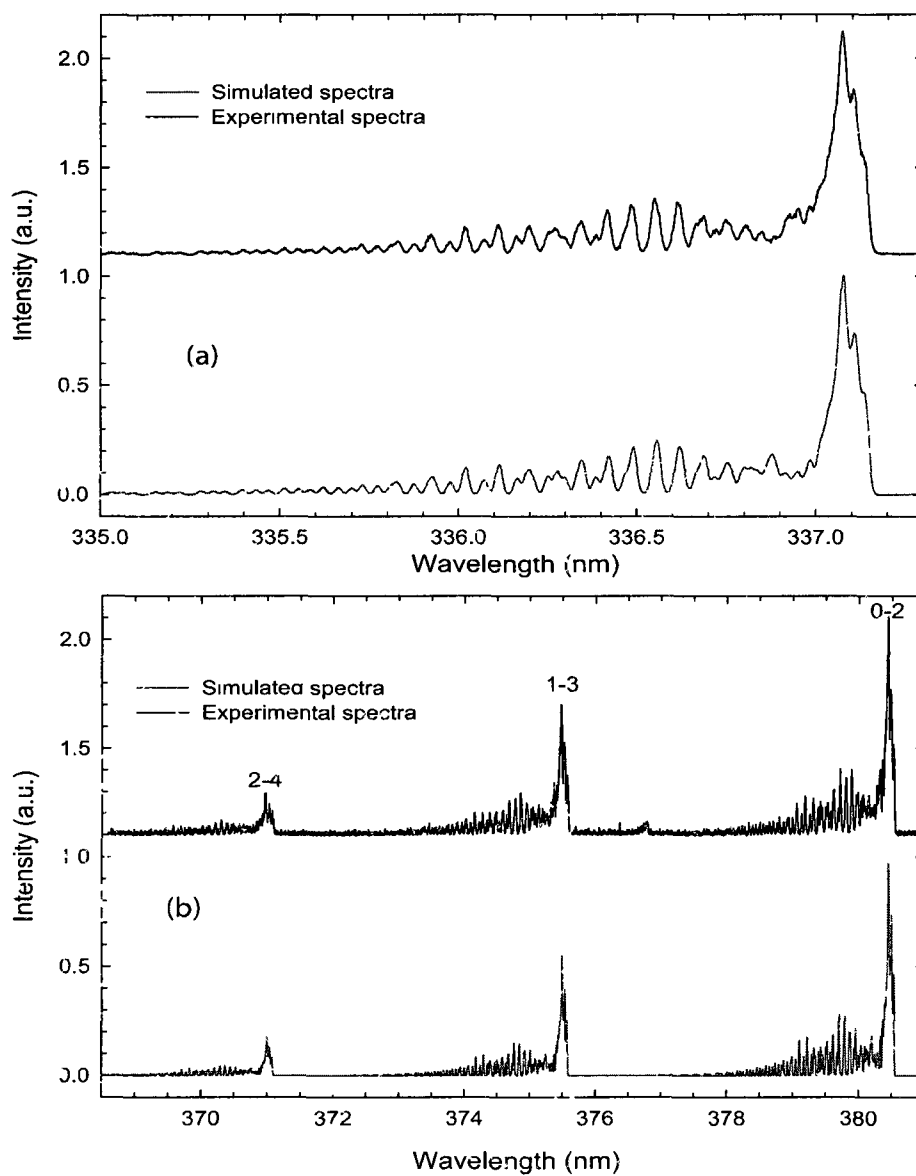


FIG. 65: Comparison of experimental and simulated spectra of  $N_2$  SPS for pure helium. (a) G-0 band.  $T_r = 325$  K; (b)  $\Delta v = -2(0-2, 1-3, 2-4)$  bands,  $T_r = 325$  K,  $T_v = 3000$  K (simulated spectra courtesy of J. Jarrige) [12].

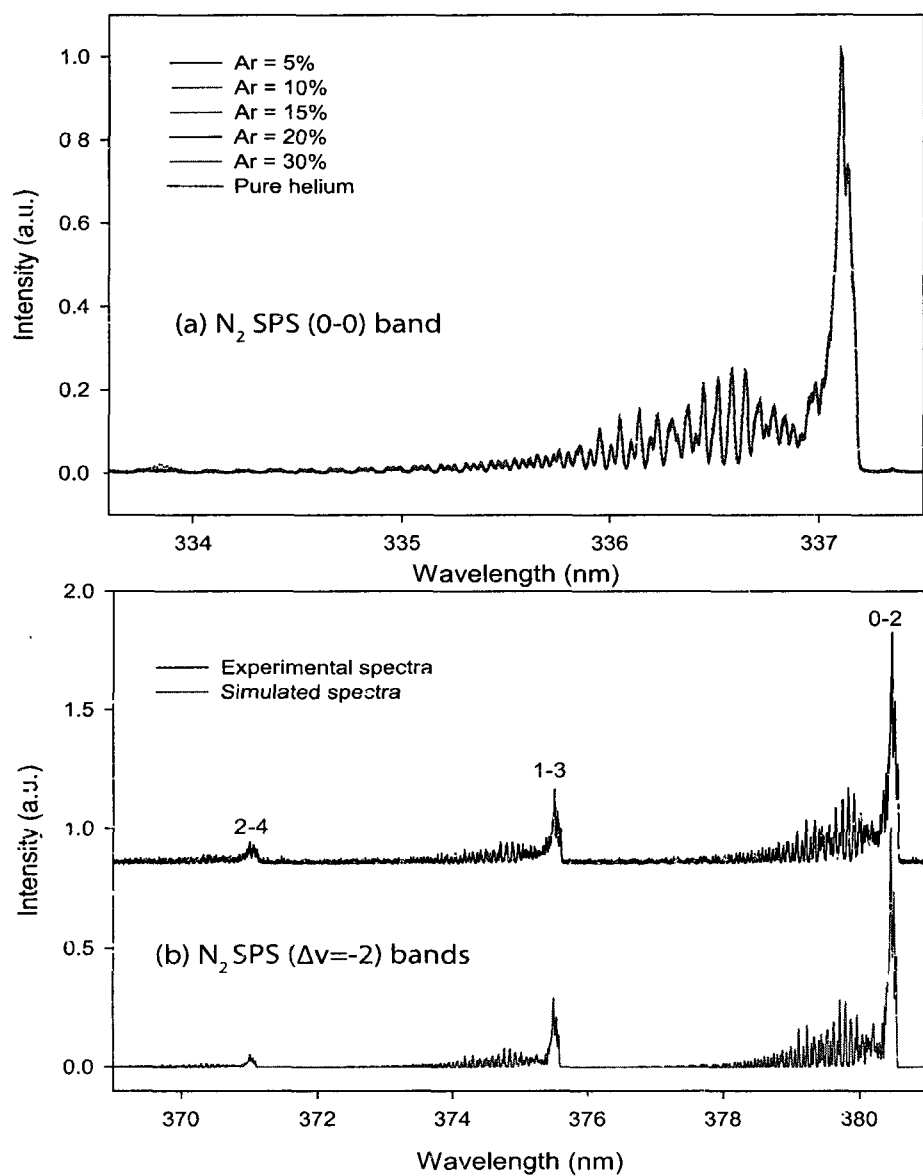


FIG. 66: Comparison of experimental and simulated spectra of  $N_2$  SPS for different argon admixtures: (a) 0-0 band,  $T_r = 325$  K; (b)  $\Delta v = -2$  (0-2, 1-3, 2-4) bands,  $T_r = 325$  K,  $T_v = 3000$  K (simulated spectra courtesy of J. Jarrige) [84].

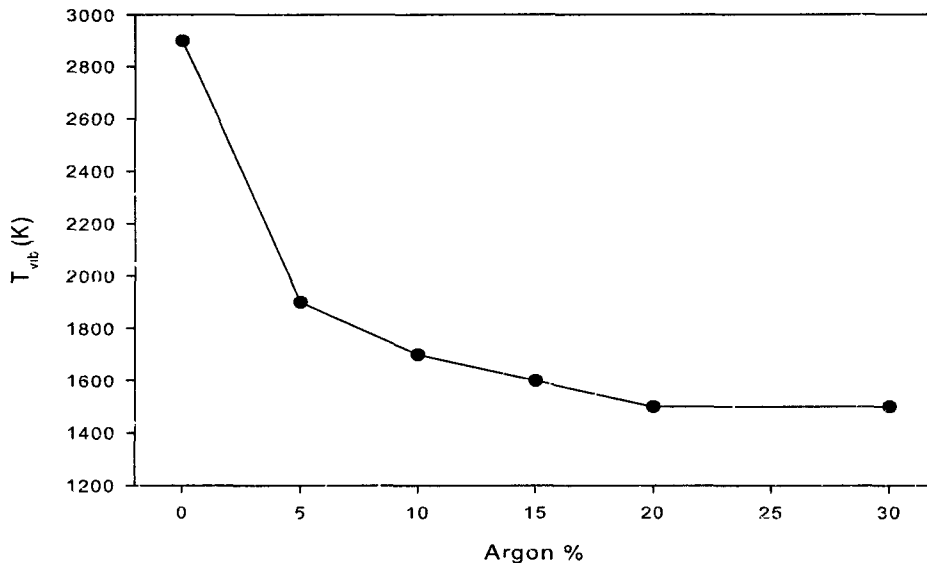


FIG. 67: Argon admixture effect on the vibrational temperature (courtesy of J. Jarrige) [84].

## V.6 LINE RATIO OF HELIUM LINE INTENSITIES

Electron density and temperature are the most fundamental parameters in the understanding of gas discharge physics [2, 4, 85]. The electron temperature or density information can be obtained by the ratio of the rate equation for an excitation level. The ratio of two emission lines is usually a function of the electron temperature  $T_e$  and electron density  $n_e$ . If the chosen lines have similar  $T_e$  or  $n_e$  dependence, the line-ratio can be a function of only  $T_e$  or only  $n_e$ . This provides the measurement of  $T_e$  without knowledge of  $n_e$  or the measurements of  $n_e$  without knowledge of  $T_e$ . The emission lines of the helium atom more accurately predict the electron temperature [86] as the lines of the argon atoms estimate the electron density [87]. Accurate determination of these plasma parameters highly depends on accurate cross sections [88].

We compare the 587.6 nm ( $2^3P \rightarrow 3^3D$ ) line with 706.4 nm ( $2^3P \rightarrow 3^3S$ ) line of helium corresponding to upper level electronic energies of 23.07 eV and 22.72

eV, respectively. The information obtained in this section elucidates the excitation characteristics of the helium plasma jet.

The plasma bullet propagates in the ambient air at atmospheric pressure, and it collides with numerous atoms and molecules. Even though recent developments offer promising results on the applicability of the line ratio methods to the plasma jets [89], there are several important questions that need to be answered, such as accuracy of the maxwellian electron distribution assumption or the effect of the gas mole fraction change along the ionization channel. Due to these drawbacks, our experimental results will not be correlated with the cross sections, but our result will stay as a good starting point for detailed future studies.

The ratio of two atomic line intensities is equivalent to the ratio of the upper states densities:

$$\frac{I_{587.6}}{I_{706.4}} = \frac{n(He^3D)}{n(He^3S)} = f\left(\frac{E}{N}\right) \quad (15)$$

where  $n(He^3D)$  and  $n(He^3S)$  are the densities of electronic states ( $3^3D$ ) and ( $2^3P$ ) of helium, and  $E/N$  is the reduced electric field. The cross-sections of the electronic collisions depend on the electron energy and, therefore, on the reduced electric field [12].

The line ratio of  $I_{587.6}/I_{706.4}$  intensities can be seen as a function of the applied voltage in Figure 68 inside the reactor (between the electrodes) and along the plasma jet (3 mm, 10 mm, and 20 mm). For all axial locations, the intensity ratio increases with higher HV pulse amplitude. The ratio of helium line intensities in the reactor becomes 2 times higher from 5.5 kV to 10 kV. Along the plasma jet axis, the ratio increases with a factor of 1.48, 1.281, and 1.353 for 3 mm, 10 mm, and 20 mm, respectively. Therefore, these results state that the high-energetic electrons are involved in the kinetic mechanism of the discharge not only inside the reactor but also along the plasma jet [12]. It is worth noting that the electron energy distribution is directly related to the applied electric field between the electrodes.

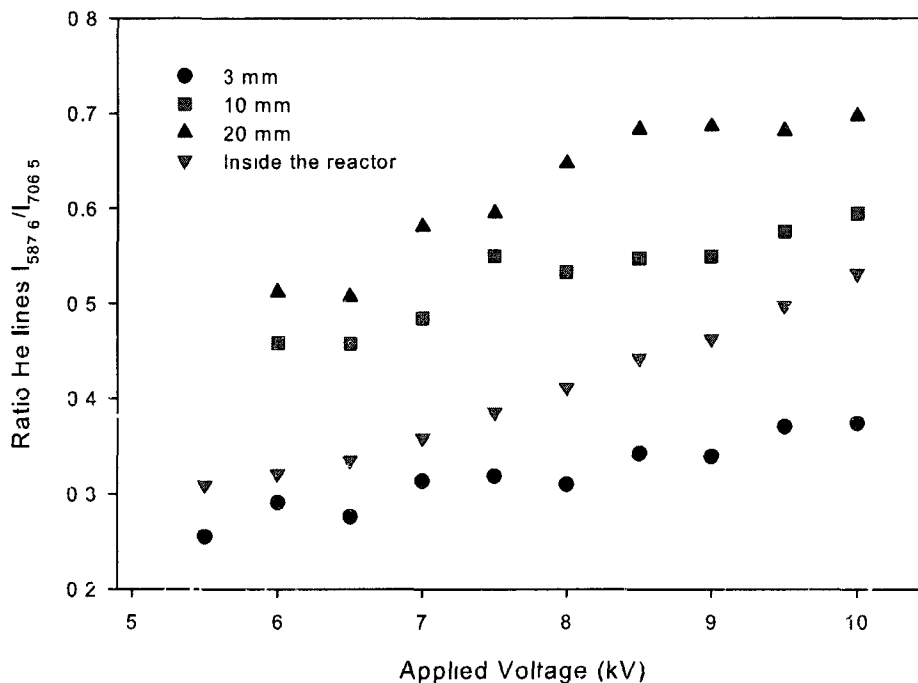


FIG. 68 Helium line ratio 587.6/706.5 nm as a function of the applied voltage pulse inside the reactor and along the plasma jet

## V.7 SUMMARY

In this chapter, the chemistry of atmospheric pressure low temperature plasma jets (APLTPJs) was investigated by spatio-temporally resolved optical emission spectroscopy (OES) for different experimental parameters

In the first section, the kinetic mechanism of the APLTPJs was discussed for pure helium, helium/oxygen, and helium/argon working gases. It was found that the kinetic mechanisms of pure helium and helium/oxygen mixture resemble each other while that of helium/argon mixture significantly differ. This differentiation provides an opportunity to understand the roles of different species in the plasma bullet and ionization channel. Our previous findings in chapter IV were also supported by these observations. One of the most important results in this chapter is that even a small amount of argon admixture significantly increases the intensity of  $N_2$  SPS

while decreasing  $N_2^+$  FNS dramatically. This change in chemistry could be very useful during applications of the APLTPJs. In addition, important emission lines of the species in the visible-infrared and ultraviolet spectra were explained in order to understand the role of the species in the generation of the plasma jets.

In section V.2, the behaviors of important emitting species were studied for different HV pulse amplitudes, pulse widths, repetition rates, and flow rates. These species include  $N_2$  SPS 0 – 0 band at 337 nm,  $N_2^+$  FNS 0 – 0 band at 391 nm,  $OH(A - X)$  at 308 nm,  $He$  ( $2^3P \rightarrow 3^3S$ ) at 706 nm and  $O$  ( $3^5S \rightarrow 3^5P$ ) at 777 nm. This experimental survey will provide a useful set of tabulated data for future experiments.

Spatio-temporally resolved distributions of excited species offered great insights into the plasma bullet's propagation mechanism. Based on the spatially resolved spectra, intensities of helium line at 706.4 nm, SPS of  $N_2$  at 336.5 nm, and FNS of  $N_2^+$  at 391 nm dramatically increase when the ionization wave starts interacting with air molecules. This is also true for  $OH(A - X)$  at 308 nm and  $O$  ( $3^5S \rightarrow 3^5P$ ) at 777 nm but the increase in the line intensities remains relatively at lower values. At around 12 mm, the intensities experience their maxima. Temporal behavior of excited states were also explored for pure helium and helium/argon (95:5) mixture at 20 mm axial position. Accordingly, the emitting species in pure helium reaches their peaks later than in helium/argon mixtures. Helium line at 706.5 nm, argon line at 751 nm,  $N_2$  SPS at 336.5 nm, and  $N_2^+$  FNS at 391 nm increase very quickly at the arrival of the ionization front. On the other hand,  $N_2$  SPS and  $N_2^+$  FNS decay slower than He and Ar. In pure helium, a second peak can be seen at relatively lower intensities of the first peaks. However, this second peak in helium/argon mixture is not as distinctive as in pure helium.

The radial profiles of the plasma bullets were determined for different species, axial positions, HV pulse amplitudes, and argon admixtures. These profiles indicated that the plasma bullet is not radially uniform. The Abel-inverted radial profiles revealed that the plasma bullet has a donut(or ring)-shaped structure.

The rotational and vibrational temperatures were obtained by comparing the rotational and vibrational spectra of  $N_2$  SPS with simulated spectra. It was found that the rotational temperature is well below 400 K, and it is not a function of HV pulse amplitude. On the other hand, the argon admixture does not affect the rotational temperature while it decreases the vibrational temperature.

In the last section, the ratio of 587.6 nm and 706.4 nm lines of helium excited states were employed to figure out excitation characteristics of the plasma jet. It is found that the high-energetic electrons play a key role not only inside the reactor but also along the plasma jet axis.



## CHAPTER VI

### APPLICATIONS IN BIOLOGY AND MEDICINE

Even though attempts to use plasmas in sterilization of medical equipments are not new, their inactivation process is not well known. About 15 years ago, a few engineers and biologists initiated a new interdisciplinary field, now called "Plasma Medicine". They were seeking the answers to some fundamental questions: What happens when biological cells are exposed to low temperature plasmas? Which biochemical pathways enter into play between plasmas and cells? Up to now, these questions have been only partially answered, and a complete picture has yet to emerge [9].

Experimental results showed that charged particles in low temperature plasmas indirectly play a role in biological applications. In the case of our plasma jets, the lifetime of charged particles is very short (usually in the order of the pulse width). However, these charged particles produce short-lived and long-lived reactive species such as  $O$ ,  $O_2^*$ ,  $O_3$ ,  $OH$ ,  $NO$ ,  $NO_2$ , etc. These reactive species interact with the articles under treatment. At the present time, which species exhibit a bactericidal effect is not exactly known. It was previously reported that radicals of atomic oxygen,  $O$ , and hydroxyl,  $OH$ , produced in humid air as a result of electron impact have bactericidal effects [90, 91].

In this chapter, we will discuss potential future applications of atmospheric pressure low temperature plasma jets (APLTPJs) in biology and medicine. First, we will introduce a pilot study examining cytotoxic effect of low temperature plasmas on living cells. Furthermore, the effectiveness of the APLTPJs will be shown on bacteria associated with dental caries and periodontal diseases. In the last section, the destruction of amyloid fibrils by the APLTPJs will be studied. Amyloid fibrils are known to cause Alzheimer's and Parkinson's diseases. In this manner, the destruction of these fibrils will open up a new horizon for applications of the APLTPJs.

#### VI.1 STUDIES ON CYTOTOXICITY OF THE PLASMA JETS

Low temperature plasmas are being actively considered for medical applications such as wound healing and blood coagulation. Several investigators have reported promising results regarding the treatment of chronic wounds and even the induction of apoptosis in some types of cancer cells. However, before seriously considering plasma

technology for these applications and others involving biological cells, it is important to evaluate its cytotoxicity. Cells can be damaged by various agents generated by plasmas. These include heat, ultraviolet radiation, and chemically reactive species. In this section, the behavior of a multi-cell organism, planaria worm (*dugesia tigrina*) species, is investigated after exposure to the plasma for a certain length of time. A postpharyngeal cut (the tails of the worms were sliced off) was carried out, such that the anterior section of the worm could feed. To maximize potential for regeneration, the worms were fed twice per week. Nearly all the worms survived the exposure, and most lived throughout the following 14 days. Figure 69 shows the growing process of the planaria to its normal dimensions in 14 days after a 40-second exposure to a plasma plume.

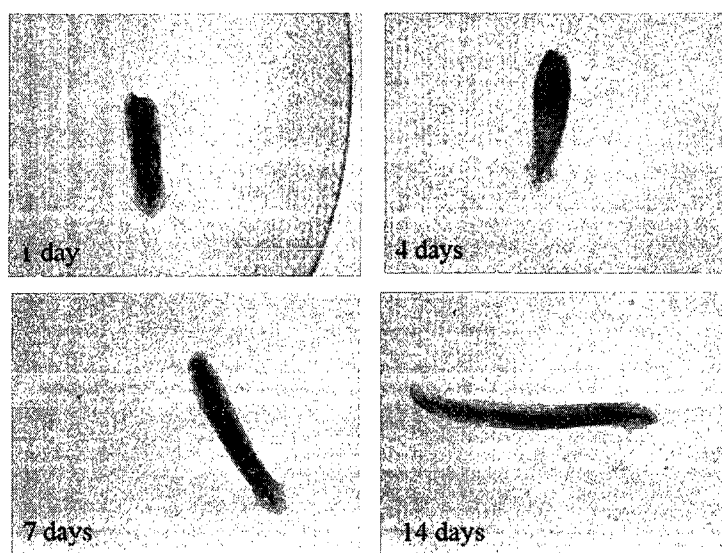


FIG. 69: Effects of the plasma pencil on cell regeneration after a cut. The plasma exposure duration is 40 seconds.

The Planaria regeneration process is observed for 10, 20, and 40 exposure times. Experiments for each exposure time are repeated 4 times. Planaria worms usually live in water. When they move, their body structure elastically changes. For example the length of the planaria gets longer when the width of the planaria gets narrower, or vice versa. This elastic structure of the planarian makes it difficult to quantitatively determine the growing pattern. For this reason, the length/width ratio is used for the

interpretation of the experimental results. As shown in Figure 70, this ratio remains at the same order for all exposure times during the regeneration process. Based on this pilot study, it can be concluded that no cytotoxicity effect of the APLTPJs is found during the regeneration of the planarian worms.

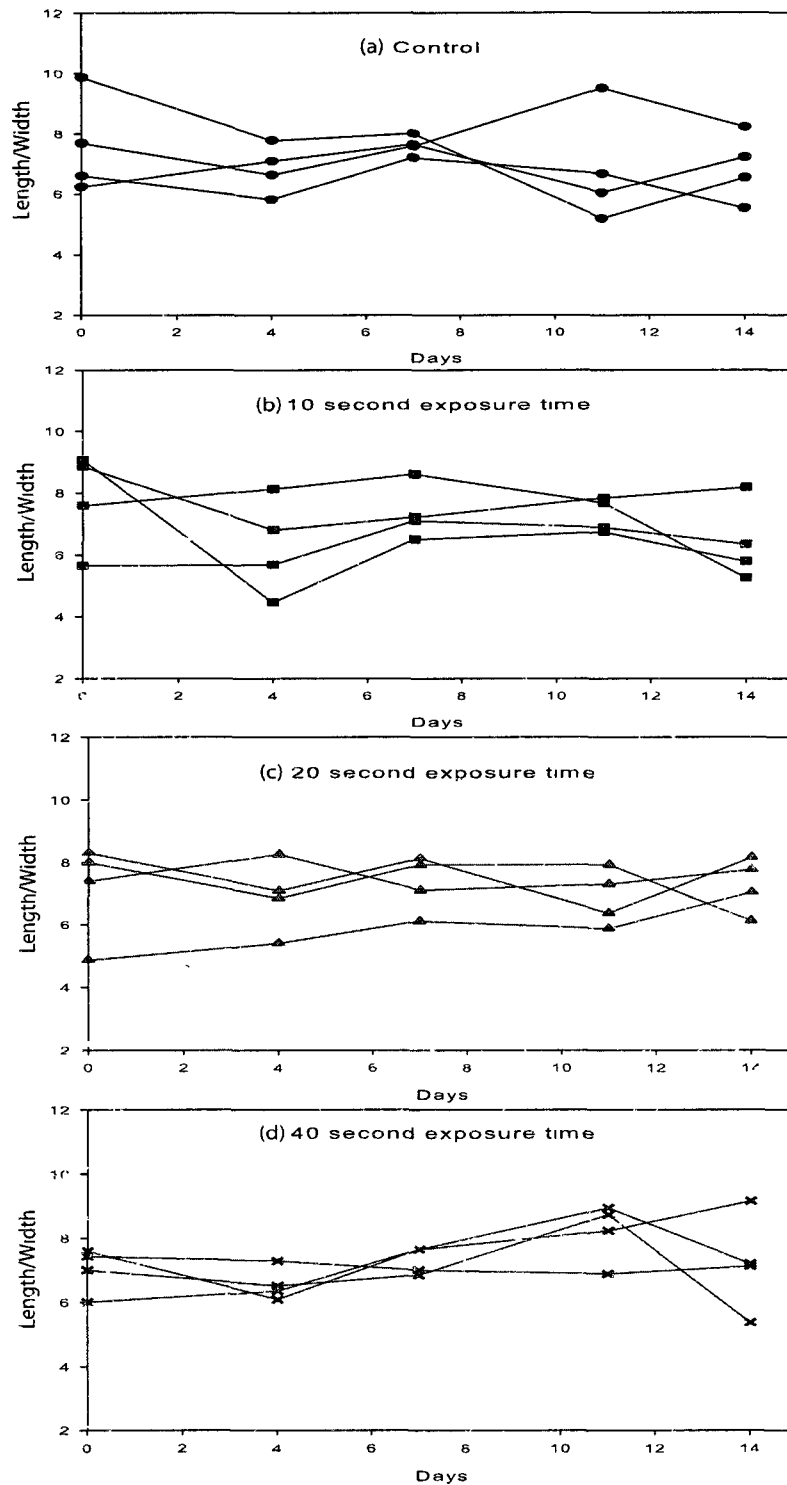


FIG. 70: Cell regeneration patterns after the plasma pencil exposure: (a) No plasma is exposed to samples; (b) 10 seconds plasma exposure; (c) 20 seconds plasma exposure, (d) 30 sec plasma exposure.

## VI.2 DENTAL HYGIENE APPLICATIONS OF THE PLASMA JETS\*

The effect of the APLTPJs is studied on bacteria of dental relevance\*. The plasma pencil is used in experiments. When necessary, a small pipe is added to the tip of the plasma pencil to confine helium flow on the samples. The diameter of this pipe is the same as that of the hole at the center of the ground electrode.

Selected microorganisms are associated with dental caries (*S. mutans*) and periodontal diseases (*P. gingivalis*, *T. denticola*, and *T. forsythensis*). Even though the plasma exposure procedure is similar for each bacteria type, the preparing of samples and the quantitative results after an exposure undergo different procedures. In this section, the details of inactivation result by comparing each time exposure will be statistically discussed. We will explore whether the APLTPJs are able to inhibit growth of *S. Mutans*, *P. gingivalis* and *T. denticola*. The results may lead to new application areas in periodontal therapy.

### VI.2.1 *Streptococcus mutans (S. Mutans)*

The current study offered a new method of inactivating *S. Mutans*. *S. Mutans* is one of the most important cariogenic microorganisms [92]. *S. Mutans* is a gram-positive and facultatively anaerobic microorganism. This microorganism is able to form biofilms on teeth (i.e. dental plaque), penetrate into fissures, and erode the enamel and dentine. Due to its facultatively anaerobic behaviour, *S. Mutans* prefers oxygen-free environment but it is also able to survive in the presence of oxygen. Therefore, it can be usually found in fissures where less oxygen is present. In addition inside fissures the antimicrobial activity of saliva is insignificant. Since the optimum growth temperature of *S. Mutans* is between 30 °C and 47 °C, the human body temperature of 37 °C provides a perfect environment for *S. Mutans*. Its inactivation temperature is above 60 °C [93].

An individual *S. Mutans* colony is usually easy to kill; however, *S. Mutans* colonies can form thick biofilms that are hard to penetrate into in the presence of a sucrose containing high-molecular weight glucans [92]. Current inactivation methods of *S. Mutans* include the rinsing with chemicals [93] and laser irradiation [94]. In clinical practice, drilling caries accompanied with healthy tissue is currently in use.

---

\*This section was presented as an invited talk in *Gordon Research Seminar*, July 10-11, 2010 New London, NH.

At this point, APLTPJs promise a great advance as a new inactivation method with fewer side effects.

The experimental procedure is as follows: cells are plated and incubated using a spiral-plating instrument. Various dilutions are used. CFUs quantified following different exposure times: 0, 60, 120, 180, and 300 seconds. Experiments are repeated five times for each exposure time. As shown in Figure 71, the average CFU decreases as the exposure time to the plasma increases.

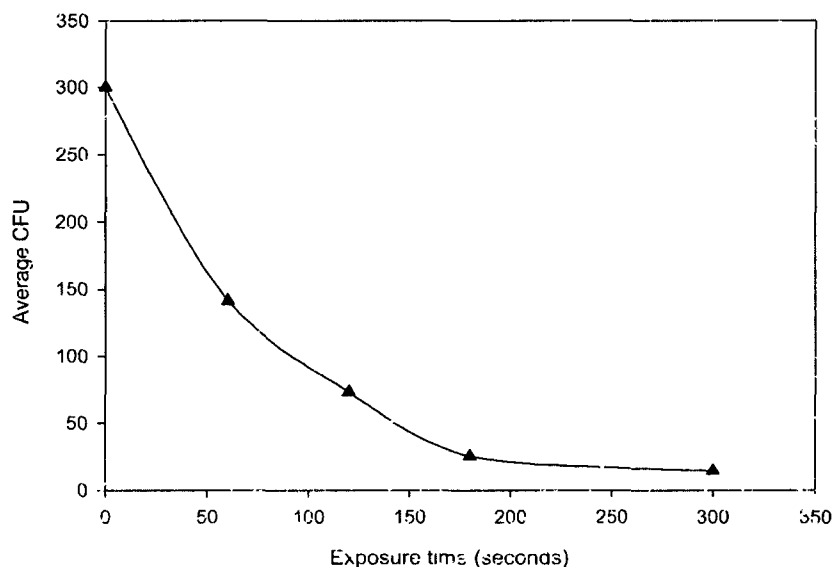


FIG. 71: Mean CFU change over time for *S. Mutans*.

Our experimental results are also statistically evaluated. In this manner, standard deviation,  $p$ -value,  $f$ -statistic, and inactivation factor are calculated by means of analysis of variance methods (ANOVA). Table 8 shows mean CFU/ml and standard deviation.  $p$ -value and  $f$ -statistic are revealed in Table 9 and Table 10 for the CFU/ml reduction compared to the control overall and each exposure time. Based on Table 8, Table 9, and Table 10 there is a significantly bactericidal effect APLTPJs on *S. Mutans* for each exposure time; for example, CFU/ml is 141.30 with a standard deviation of 46.06, a  $f$ -statistic of 5.12, and  $p$ -value of 0.0272. For 300 seconds exposure time, the APLTPJ significantly kills *S. Mutans*. In the statistical point of view,  $p$ -value is 0.0001 when compared to the control samples; however for exposure

times of 180-300 seconds,  $p$ -value is 0.4994 (  $f$ -statistic of 0.46), which statistically states that difference between 180 and 300 exposure times is not significant.

An inactivation factor is also revealed in Table 11 for each sample. Percent inactivation for *S. Mutans* increases with longer exposure times, such as 95% for 300 seconds. There is no significant difference between 180 and 300 exposure times.

TABLE 8: Summary statistics of CFU/ml for all samples, where N represents number of the repeated experiments for *S. Mutans*.

Exposure time(seconds)	N	Mean (CFU/ml)	Standard deviation
0	18	300	0.00
60	10	141.30	46.06
120	18	73.22	41.04
180	18	25.22	20.46
300	18	14.44	10.19

TABLE 9: CFU/ml repeated measures ANOVA for control versus the exposure times for *S. Mutans*.

Exposure time (seconds)	$f$ -statistic	$p$ -value
0 to 60	5.12	0.0272
0 to 120	30.85	<0.0001
0 to 180	95.09	<0.0001
0 to 300	108.72	<0.0001

TABLE 10: CFU/ml repeated measures ANOVA for the consecutive exposure times for *S. Mutans*.

Exposure time (seconds)	$f$ -statistic	$p$ -value
0 to 60	5.12	0.0272
60 to 120	5.22	0.0259
120 to 180	17.83	<0.0001
180 to 300	0.46	0.4994

TABLE 11: Summary statistics of inactivation factor (IF) for all samples for *S. Mutans*.

Exposure time(seconds)	N	% Mean	S. deviation	MinIF	MaxIF
0	18	0.00	0.00	0.00	0.00
60	10	0.53	0.15	0.29	0.71
120	18	0.76	0.14	0.53	1.00
180	18	0.92	0.07	0.78	1.00
300	18	0.95	0.03	0.89	1.00

### VI.2.2 *Porphyromonas gingivalis* (*P. gingivalis*)

*Porphyromonas gingivalis* (*P. gingivalis*) is a gram-negative anaerobic bacterium that is often found in deep periodontal pockets. *P. gingivalis* causes severe chronic periodontitis covering tissue colonization, destruction, and host defense perturbation [95]. Therefore, *P. gingivalis* is strongly associated with periodontal disease, disease progression, and refractory periodontitis.

A culture of ATCC-strain 33277 *P. gingivalis* is obtained. A total of 40 *P. gingivalis* samples are inoculated in TSB sheep's blood agar plates as a lawn for 48 hours at 37 °C. TSB sheep blood agar plates were exposed to the plasma pencil for 5, 7, 9, and 11 minutes. Control samples were exposed to helium gas only to control the flow effect of helium on the samples. Experimental parameters of the plasma pencil are as follows: 8 kV applied voltage; 5 kHz repetition rate; 500 ns pulse width. 5 L/min flow rate.

After the plasma pencil treatment, TSB sheep blood agar plates were incubated anaerobically for 72 hours at 37 °C in order to control whether a contamination is present. Since *P. gingivalis* does not grow as a colony, CFU counting procedure is not applicable. For that reason, the inhibition zone diameter of the treatment is measured after an exposure instead of CFU procedure. Example of exposed samples are shown in Figure 72. The inhibition zone of the samples can be seen.

The results indicate that the bactericidal effect of the APLTPJs is statistically significant for 5, 7, 9, and 11 minute exposure times if compared to control samples (Table 12). All control samples show no killing pattern (i.e. no zone of inhibition).

As shown in Figure 73, longer exposure time leads to a wider inhibition zone. It is worth noting that the inhibition zone goes beyond the diameter of the plasma plume. This indicates that continuous helium flow coming out from the reactor



carries long-lived species produced by the plasma chemical reactions over the surface of the samples. In addition, it also shows that these long-lived species are involved in the interaction with bacteria under treatment. This wide-range killing pattern makes this new method especially applicable and practical for future medical and dental applications.

APLTPJs inactivation mechanism on *P. gingivalis* including morphological and structural cellular changes needs further investigations using more advanced techniques, such as scanning electron microscopy.

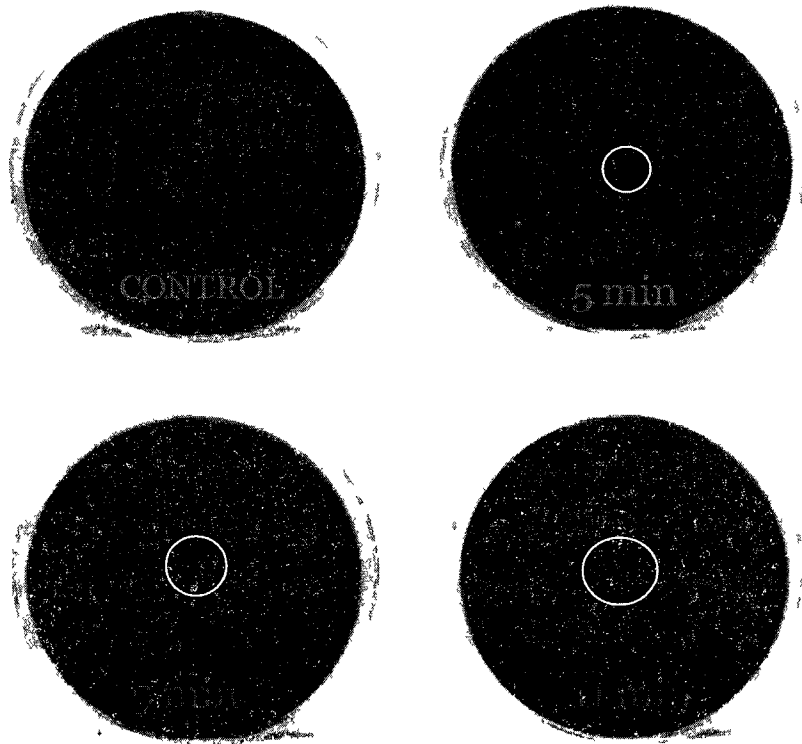


FIG. 72. *P. gingivalis* spread over sheep blood agar samples and exposed to the plasma pencil.

### VI.2.3 *Treponema denticola* (*T. denticola*)

*Treponema denticola* is a motile (spontaneous movement) and highly proteolytic (pertaining to the dissolution of proteins) bacterium. This gram-negative oral spirochete

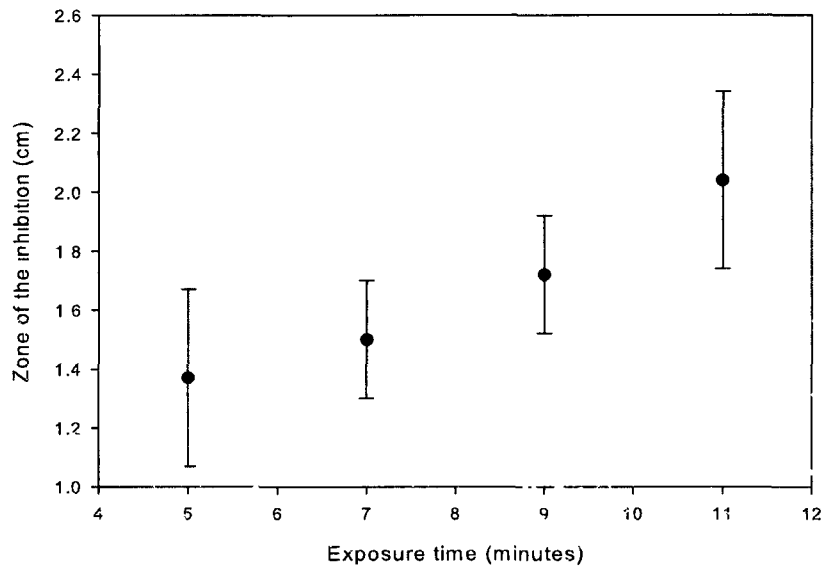


FIG. 73: Change in mean zones of inhibition for different exposure times.

is associated with the incidence and severity of human periodontal disease. *T. denticola* dwells in a complex and diverse microbial community in the oral cavity and is highly specialized to survive in this environment.

*T. denticola* was inoculated in NOS spirochete medium (three day old broth) and incubated for 48 hrs at 37 °C anaerobically. The bacteria are evaluated under the microscope using the live/dead stain procedure. Samples are exposed to the plasma pencil for 5, 7, 9, and 11 minutes. Control samples are exposed to He gas only. Experimental parameters are as follows: 7.5 kV the applied voltage, 5 kHz the repetition rate, 500 ns the pulse width, and 5 L/min the flow rate.

Live/dead stain procedure is an assay based on the emission of fluorescent light from live and dead cells by means of a microscope. Live/Dead Bacterial Viability Kits employ two nucleic acid stains: green-fluorescent 9 stain and red-fluorescent propidium iodide stain. These stains differ in their ability to penetrate healthy bacterial cells. Propidium iodide penetrates only bacteria with damaged membranes, reducing fluorescence when both dyes are present. Thus, live bacteria with intact membranes fluoresce green, while dead bacteria with damaged membranes fluoresce red.

TABLE 12: Summary statistics for the *P. gingivalis* samples exposed to the APLT-PJs. where N is the number of the repeated experiments and I is the zone of inhibition.

Exposure	N	Mean I	Min. I	Max. I	S. deviation	p-value
5 min	10	1.37 cm	1.00 cm	1.70 cm	0.25	<0.001
7 min	10	1.50 cm	1.30 cm	1.70 cm	0.12	<0.001
9 min	10	1.72 cm	1.50 cm	1.90 cm	0.15	<0.001
11 min	9	2.04 cm	1.80 cm	2.30 cm	0.18	<0.001

TABLE 13: CFU/ml repeated measured ANOVA for the consecutive exposure times of *P. gingivalis*.

Exposure	DF	Mean square	f-statistic	p-value
5 min to 7 min	1	0.08450	4.89	0.0360
7 min to 9 min	1	0.2420	14.01	0.0009
9 min to 11 min	1	0.4473	25.91	<0.0001

Live and dead *T. denticola* cells are shown in Figure 74. For the control samples both live and dead cells are present in Figure 74 while a 5 minute exposure shows a complete killing pattern.

Although the killing pattern of the APLTPJs is clearly shown in Figure 74, obtaining quantitative measurements remains a major obstacle in this method. If there is a complete killing on the sample, this procedure works perfectly. However, if the bacteria are partially killed, it is hard to obtain a quantitative outcome. Since the microscope needs to be focused on a certain region of the sample surface, there will be a lack of information about other points on the surface. On the other hand as seen in Figure 74, bacteria concentration seems more localized at some points on the microscope slide. Therefore, this localized bacteria accumulation may cause an underestimation. These difficulties need to be solved for future experiments.

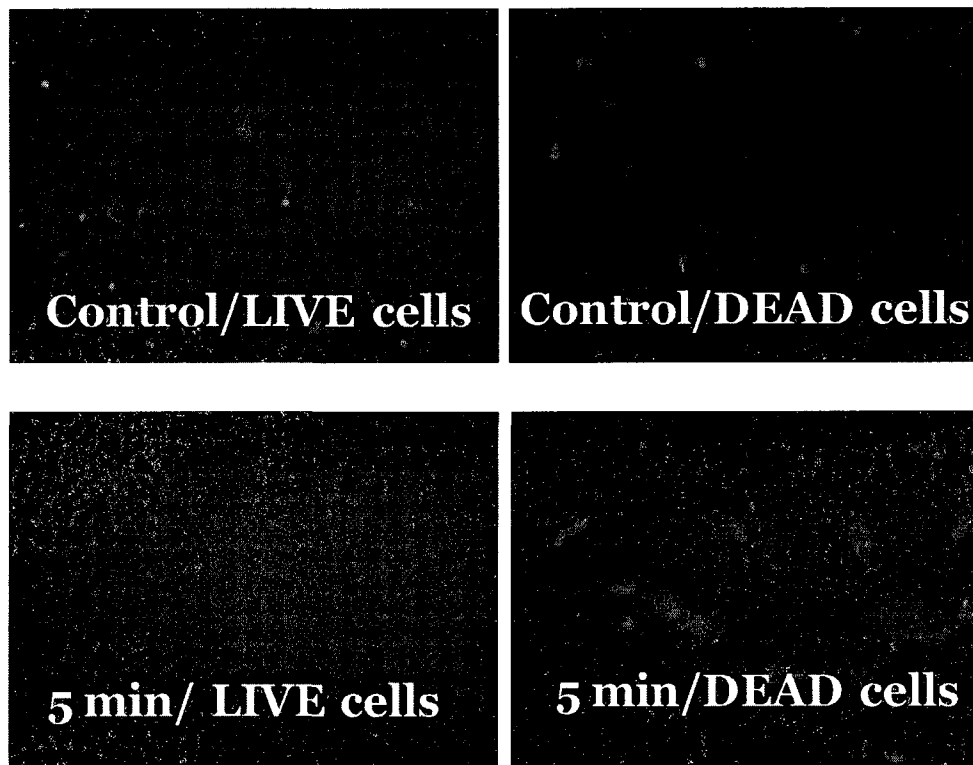


FIG. 74: A LIVE/DEAD stain procedure results for *T. dentocola*.

### VI.3 DESTRUCTION OF $\alpha$ -SYNUCLEIN BASED AMYLOID FIBRILS<sup>†</sup>

Amyloid fibrils are ordered beta-sheet aggregates that are associated with a number of neurodegenerative diseases such as Alzheimer's and Parkinson's [96]<sup>†</sup>. There are approximately twenty proteins that have been found to form fibrils in humans and are associated with disease states [96]. However, it has been postulated that all proteins can be induced to form this low energy state if subjected to the right conditions. We are investigating potential methods involving the use of cold plasma that will lead to the destruction of amyloid fibrils formed by the protein  $\alpha$ -synuclein, which underlies Parkinson's disease and the amyloid- $\beta$  peptide which is associated with Alzheimer's disease [97]. Parkinson's disease is a neurodegenerative movement disorder. It results

<sup>†</sup>This section was published in *Appl. Phys. Lett.* Vol. 97, p. 143702, 2010

from the degeneration of dopaminergic neurons in the substantia nigra, a region of the brain that controls movement. Death of dopaminergic neurons by the formation of amyloid fibrils with the protein  $\alpha$ -synuclein results in decreased production of dopamine. Lack of dopamine results in the major symptoms of Parkinson's disease: rigidity to muscles constantly contracted, resting tremor, postural instability and slowness in initiating movement. Alzheimer's disease is caused by the fibrillation of a peptide called amyloid- $\beta$  after it is cleaved from the precursor protein on the cell surface in the brain. The residues composing this peptide are 1-42 and spontaneously form amyloid fibrils. The fibrillation that causes Alzheimer's begins in the temporal lobes of the brain and then spreads to other parts of the brain, thus killing cells and interfering with neural transmissions. At present there is no cure for these progressive and debilitating diseases.

In our experiments, the human protein  $\alpha$ -synuclein was selected as the initial model system. It is produced by expressing it in *Escherichia coli* from a DNA clone inserted into the bacteria. The soluble protein is then extracted from the bacterial cells and purified by ion-exchange and gel filtration chromatography. The  $\alpha$ -synuclein protein (4-6 mg/ml) is dissolved in a buffer solution of 0.2 M NaCl in 20 mM Tris Base, pH 7.5 and incubated at 37 C in an incubator shaking at 150-190 rpm. After 15 days mature fibrils analogous to those in a patient's brain are formed in our test tubes.

The amyloid fibrils in solution are placed into small tubes (0.2ml) or glass slides and exposed to the plasma pencil for varying lengths of time (up to 10 minutes). After exposure the fibrils are immediately fixed onto 400 mesh formvar coated copper grids for analysis by electron transmission microscopy. Figure 75.a shows mature intact  $\alpha$ -synuclein fibrils, while Figure 75.b, 75.c, 75.d, and 75.e show the morphology of fibrils after 2, 4, 6, and 10 minute exposure to the plasma, respectively. It clearly shows that a 6 minute exposure induces severe damage to the fibril and causes extensive breakage. It is of note to mention that evidence of breakage starts showing up after only 2 minutes exposure to the plasma. Although preliminary, these are extremely important results as this methodology provides a facile and novel mechanism whereby amyloid fibrils can be easily destroyed. Recently, three other methods have also been shown to break fibrils. These are laser beam irradiation [98, 99], ultrasonication [100] and mechanical breakage by stirring at 1000 rpm [101]. However, unlike these methods which rely on physical mechanisms, our method is based on the "dry"

chemistry of the plasma. Non-equilibrium plasmas such as the one generated by the plasma pencil are sources of reactive oxygen species, ROS (such as atomic oxygen and superoxides) and reactive nitrogen species, RNS (such as  $NO_x$ ) which are known to chemically denature cellular lipids and proteins. Thus, we expect that under plasma exposure the fibrils undergo chemical reactions that compromise their structural as well as chemical integrity.

Even though the ability of the plasma pencil breaking amyloid fibrils offers a great advancement to cure Parkinson's and Alzheimer's diseases, the issues, such as the cytotoxicity and dehydration levels of the neuronal cells after the plasma exposure, need to be carefully investigated in future studies.

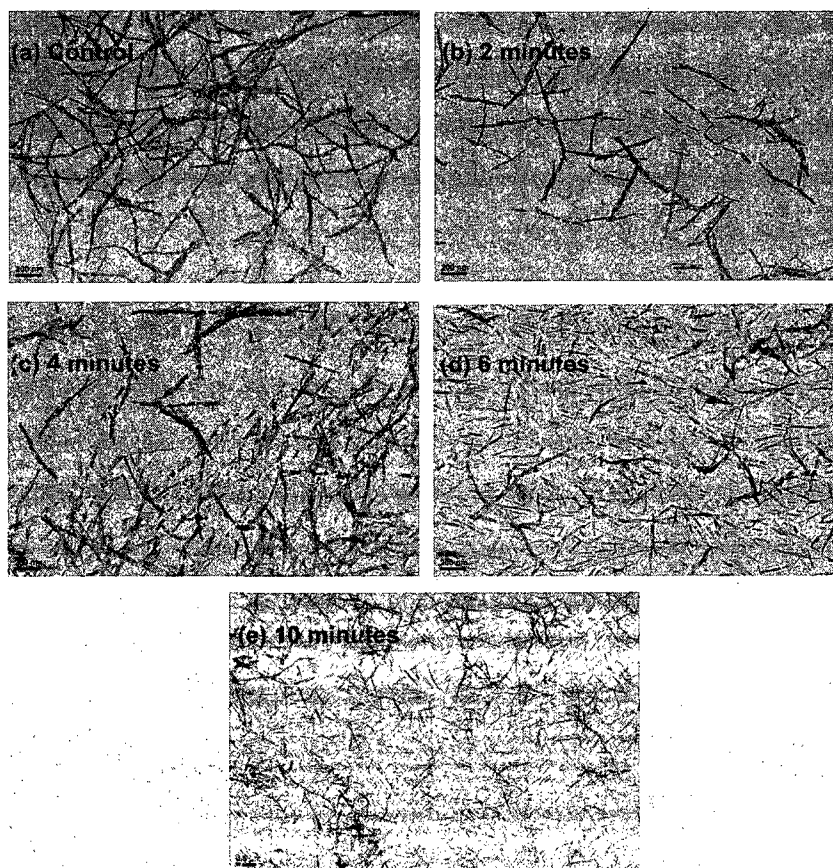


FIG. 75: (a) TEM image of mature intact  $\alpha$ -synuclein fibrils; (b), (c), (d), and (e) TEM images of the fibrils after 2, 4, 6, 10 minute exposures to the plasma plume, respectively, showing clear evidence of extensive breakage.

## VI.4 SUMMARY

Plasma medicine field is a field that is finding a place in the scientific community by combining a number of fields: physics, bio-chemistry, engineering, biology, microbiology, and medicine. Currently, several ongoing experiments are being carried out by several groups.

A pilot study was developed to investigate the cytotoxic effect of low temperature plasmas on living cells. No particular negative effect was found during the regeneration of the planarian worms after a cut. Even though more detailed studies are needed to figure out side effects, based on these current results, we can conclude that low temperature plasmas could be safe to use on living tissue.

Dental hygiene is one of the most promising applications of APLTPJs. The effectiveness of the APLTPJs was studied for different bacteria cultures associated with dental caries and periodontal diseases. The present study showed that there is a significant reduction or complete killing in these dental relevant bacteria after a plasma pencil exposure. It was also indicated that an increase in exposure time or applied power leads to more killing pattern on the samples.

We investigated potential methods that lead to the destruction of fibrils, formed by the protein alpha-synuclein, which underlie Parkinson's disease. At present there is no cure for this progressive and debilitating disease. Initial studies stated that APLTPJs can break these alpha-synuclein fibrils into smaller units in vitro. This avenue of research may facilitate the development of a medical treatment.

## CHAPTER VII

### CONCLUSIONS

#### VII.1 SUMMARY AND OUTLOOKS

Physical and chemical characteristics of atmospheric pressure low temperature plasma jets (APLTPJs) have been investigated with their potential applications in biology and medicine.

The plasma pencil and tube reactor were used to generate the plasma jet during this study. Research interest and application perspective determine the suitability of reactor type. For example, the secondary discharge ignition is more visible in the plasma pencil configuration due to the electrode configuration while characterizing the plasma chemistry more convenient in the tube reactor due to the symmetrical and stable flow structure.

The electrodes using dielectric materials exhibit different behavior. In these capacitive discharges, the displacement current ( $I_{NO}$ ) need to be subtracted from the total current ( $I_{TOT}$ ) to find the actual discharge current ( $I_{DIS}$ ). The discharge waveform includes two peaks with positive and negative polarities at the rising and falling edge of HV pulse, respectively. The first peak with positive polarity corresponds to a first discharge (i.e. breakdown time) in the reactor. The second peak with negative polarity indicates a secondary discharge occurring in the reactor when the applied voltage becomes zero. When more energy is injected into the reactor, the discharge current experiences larger values. Average power when 10 kV applied voltage pulse is applied was calculated as 2.03 W at a pulse repetition frequency of 10 kHz. It is also worth noting that the discharge waveform of the plasma pencil has another peak with a positive polarity just after the first discharge peak decays. It was found that the occurring time of this second peak corresponds to the launching time of the plasma bullet from the reactor. The plasma bullet itself also carries a current in the ionization channel, called the jet current ( $I_{JET}$ ). This jet current value was found to be in the order of 10 mA by means of a Rogowski coil.

High-speed fast photography techniques using ICCD camera allow the elucidation of the plasma bullet structure of the APLTPJs with a time resolution as low as 3 ns. It was revealed that the plasma bullet is in fact an ionization wave traveling in the ambient air along a gas channel. The dynamics, formation, and propagation



properties of the plasma bullets were investigated in chapter IV. The jet current measurements obtained in chapter III were used in the interpretation of the plasma bullet propagation mechanism. These results confirmed a recently proposed model based on the streamer discharges. Accordingly, the plasma bullet propagates further like the cathode-directed and anode-directed streamers for positive and negative HV amplitudes, respectively. These findings are highly important for future modeling approaches.

The velocity of the plasma bullet is on the same order ( $10^4 - 10^5$  m/s) with the streamers. A new similarity was explored between the plasma bullets and streamers. Accordingly, the plasma bullet velocity is proportional to its area with  $v_b = 1.46A$   $m.ns^{-1}$ .

The early formation process of the plasma bullet was observed by head-on ICCD pictures showing that the early discharge develops into the plasma bullet from the center of the reactor. However, a mechanism of supplying energetic photons that are necessary for the propagation of the plasma bullet has remained as an important question to be answered.

The phenomena of the discharge formation inside the reactor, the plasma bullet propagation along the ionization channel, and the secondary discharge ignition effect causing the plasma bullet inhibition were well explained by jet current measurements. The physical mechanisms of these events were schematically drawn in chapter IV. Especially, how the secondary discharge ignition between the electrodes stops the plasma bullet propagation took an important role. Consequently, at the falling edge of the applied voltage, a secondary discharge occurs between electrodes by means of the residual charges in the ionization channel. The electrons of this new discharge are accelerated back towards the plasma bullet by the negative charges accumulated on the dielectric surface of the positive electrode during the main discharge. This motion of the electrons creates an opposing current, "negative current", along the ionization channel. These electrons cancel out the positive space charges at the head of the bullet, and consequently interrupt the bullet propagation.

Depending on the width of the applied HV, the plasma bullet comes to an end due to either the secondary discharge ignition or low helium mole fraction. When the pulse width is large enough, low helium mole fraction along the ionization channel causes the inhibition of the plasma bullet. This limit, called the "transition point", was experimentally determined as a function of HV pulse magnitudes. Low helium

mole fraction values inside the surrounding air were extracted from the fluid dynamics simulation results for different helium flow rates and HV pulse magnitudes. These simulations have been only done for laminar flow regime by a commercially available software, COMSOL, based on finite element method. During this study, laminar, transition, and turbulent flow regimes were also experimentally identified as a function of the helium flow velocity. Based on these experiments, it was revealed that higher helium flow rates and HV amplitudes create longer plasma jets

The average and instantaneous velocities of the plasma bullet provide important insights into its dynamics. In this manner, an ICCD camera is often employed to measure the velocity of the plasma bullet. Although the ICCD camera is an excellent tool for this purpose, their high cost and sensitivity to external effects could impact their operation. Therefore, an alternative method could be very critical to measure the velocity. A new method was developed using a temporally resolved OES system. Since the plasma bullet is an ionization wave passing through the focal point of the monochromator, a peak occurs in the temporal evolution of light emitting species. When the focal point of the monochromator was shifted from one point to another in the axial direction of the plasma jet, the occurring time of this temporal peak also displaced in the time domain, accordingly. Hence, the instantaneous velocity could be measured from the consecutive measurements while the average velocity could be obtained at the end of the plasma jet. This new technique improved the time resolution of the instantaneous velocity curve to as low as a few nanoseconds. Accordingly, it was found that the plasma bullet experiences three different regimes: launching, propagation, and ending.

In chapter V, spectroscopic investigations of the API/FPJs were discussed to identify the various reactive species generated by the plasma jet in the 200-800 nm wavelength range. An optical emission spectroscopy (OES) system consisting of a half-meter monochromator with a photomultiplier (PMT) was used for this identification.  $N_2$  SPS,  $N_2^+$  FNS, and  $OH$  emission lines for the UV wavelength range, and  $He$  and  $O$  emission lines for the visible-IR range are the dominant reactive species. The kinetic mechanisms for pure helium and helium/argon mixture plasma jets were also given with necessary explanation of the radiative transitions. Argon admixture to a helium plasma jet enhances the plasma chemistry, which can be desirable for applications. This enhanced chemistry also provided an opportunity to better understand the kinetic mechanism of low temperature plasma jets.

The effect of experimental parameters on excited states was determined at 20 mm away from the tube reactor as a set of tabulated data. These experiments will especially help future investigation to optimize experimental parameters.

Spatially resolved OES was also employed along the plasma jet axis. The emitting species show a peak at 12 mm away from the reactor after the plasma bullet starts propagating. The plasma bullet reaches a chemical equilibrium at this point.  $N_2$  SPS at 336.5 nm especially decays slower than  $N_2^+$  FNS at 391 nm and  $He$  at 706.4 nm in the axial direction.

In order to find out the temporal evolutions of excited states, the PMT of the monochromator was connected to the oscilloscope after the required diffraction grating was adjusted on the software. Rising times of excited species were found to be 20 ns while their decaying times varied from 200 ns to several microseconds. After the first peak decays, a second peak reaches relatively lower values. Helium/argon mixture also temporally exhibits different behavior. It was shown that the timing of the plasma bullet is about 400 ns faster in helium/argon mixture. On the other hand, the second peak only exists for  $Ar$  emission at 750 nm for helium/argon mixture.

The bullet-like structure of the plasma jet was observed by the ICCD camera. The Abel-inverted radial profiles by OES revealed that the plasma bullet has, in fact, a ring (donut)-shaped makeup. This important finding was also confirmed for different excited species, axial positions, HV pulse magnitudes, and argon admixtures. Especially, the radial profiles for different axial positions were found to be very interesting. Accordingly, the ring-shaped structure of the plasma bullet collapses towards its center as it propagates forward in the ionization channel.

Rotational and vibrational temperatures in low temperature plasmas at atmospheric pressures give insights into their kinetic gas temperature and excitation characteristics, respectively. In this respect, rotational and vibrational bands were experimentally obtained from SPS (0-0) and  $\Delta\nu = -2$  bands of  $N_2$  by the OES system. The best-fit spectra procedure was used to figure out the rotational and vibrational temperatures by comparing these bands with the simulated one. Therefore, the rotational temperatures for pure helium and helium/argon mixtures were found to be  $325 \pm 50$  K regardless the HV amplitudes. On the other hand, the vibrational temperature for pure helium plasma jet also remains constant around 3000 K for different HV amplitude. However, an increase in argon admixture decreases the vibrational temperature from 3000 K to 1500 K.

The electron temperature or density could be estimated from the line ratios of similar-dependent excited states. An initial study has been performed to obtain an idea about the excitation characteristics of the discharge as a function of different HV amplitudes and axial positions. The ratio of 587.6 nm/706.4 nm of helium atom was used for this purpose. The behavior of these ratios indicated that high energetic electrons play an important role not only inside the reactor (between the electrodes) but also along the plasma jet.

Potential applications of the APLTPJs in biology and medicine were presented at the end of this document. A model has been developed to test the cytotoxicity effect of the APLTPJs on living cells. This was one of the important questions remaining partially unanswered until now. Based on this pilot study, no negative effects have been detected on the growing pattern of living cell. This is a good indication for future medical applications of the APLTPJs.

Dental hygiene applications of the APTLPJs have recently found a great interest in literature. We investigated the killing effect of the APLTPJs on different kind bacteria associated with dental caries and periodontal diseases, namely *S. Mutans*, *P. gingivalis*, and *T. denticola*. It was found that the APLTPJs show a very successful pattern in killing these kind of bacteria.

Parkinson's and Alzheimer's diseases are neurodegenerative disorders in humans. Amyloid fibrils are mainly responsible for these diseases. We have shown that the plasma jet is able to destroy fibrils associated with Parkinson's, effectively. Even though these initial studies exhibit promising results, they still need further investigations.

## VII.2 RECOMMENDATIONS FOR FUTURE RESEARCHES

Our new findings confirmed the model based on the photo-ionization mechanism for the plasma bullet propagation. For future self-consistent modeling studies, it is important to figure out reactions supplying the energetic photons to create the electron avalanche.

The ionization wave of the plasma bullet always follows the trajectory of the working gas. In this manner, larger plasma jets could be generated by sustaining a homogeneous flow structure in the ionization channel. A systematic study with larger tube diameters and higher flow rates can be employed to produce larger volume plasma jets. In addition, the observation of the plasma bullet behavior in different

ambient gases could be interesting.

Attempts have been made to measure ozone concentration around the plasma jet environment by using attenuation of the 253 nm line emitted from mercury/xenon lamp. Under some circumstances like higher applied voltage pulses, a 10 ppm ozone concentration was detected. However, when we repeated the experiments in different or similar conditions, no consistent results were obtained. This was due to low ozone generation of the plasma jet, probably less than 1 ppm. For future projects, a KrF laser could be employed in order to measure such a low ozone concentration.

Line ratio experiments should be extended to carry out more detailed studies by obtaining appropriate cross sections. It is noteworthy that the OES system should be relatively and absolutely calibrated to estimate electron temperature and density along the plasma jet. The variation of the helium mole fraction along the plasma should be taken into account.

We presented very important results about destroying amyloid fibrils to cure Parkinson's and Alzheimer's diseases. This avenue of research should be elaborated for different experimental parameters and environments.

In general, the applications of the APLTPJs were concentrated on biology and medicine. There is no doubt that the advantages of the APLTPJs will open new application areas in different fields, such as microfluidic device fabrication

## BIBLIOGRAPHY

- [1] J. D. Cobine, *Gaseous Conductors: Theory and Engineering Applications*. Dover Publications, Inc. New York, 1958.
- [2] F. F. Chen, *Introduction to Plasma Physics and Controlled Fusion*. New York: Plenum, 2nd ed., 1984.
- [3] F. F. Chen and J. P. Chang, *Introduction to Plasma Physics and Controlled Fusion*. Springer, 2006.
- [4] M. A. Lieberman and A. J. Lichtenberg, *Principles of Plasma Discharges and Materials Processing*. New York: Wiley, 2nd ed., 2005.
- [5] A. Fridman and L. A. Kennedy, *Plasmas Physics and Engineering*. Taylor & Francis, 2007.
- [6] J. R. Roth, *Industrial Plasma Engineering*. IOP, 1995.
- [7] Y. P. Raizer. *Gas Discharge*. Springer Berlin, 1991
- [8] M. Laroussi and T. Akan, "Arc-free atmospheric pressure cold plasma jets: A review," *Plasma Process. Polym.*, vol. 4, pp. 777-778. 2007.
- [9] M. Laroussi, "Low-temperature plasmas for medicine?," *IEEE Trans. Plasma Sci.*, vol. 93, pp. 3813-3825, 2009.
- [10] X. Lu and M. Laroussi, "Dynamics of an atmospheric pressure plasma plume generated by submicrosecond voltage pulses," *J. Appl. Phys.*, vol. 100, pp. 063302-6, 2006.
- [11] N. Mericam-Bourdet, M. Laroussi, A. Begun, and E. Karakas, "Experimental investigations of plasma bullets," *J. Phys. D: Appl. Phys.*, vol. 42, pp. 055207-7. 2009
- [12] J. Jarrige, M. Laroussi, and E. Karakas, "Formation and dynamics of plasma bullets in a non-thermal plasma jet: influence of the high-voltage parameters on the plume characteristics," *Plasma Sources Sci. Technol.*, vol. 19, pp. 065005-10, 2010.

- [13] S. V. Vladimirov and M. Y. Yu. "Solitary ionizing surface waves on low-temperature plasmas," *IEEE Trans. Plasma Sci.*, vol. 21, pp. 250–253, 1993.
- [14] J. Jarrige, E. Karakas, A. Begum, and M. Laroussi, "Investigations of plasma bullets formed in a non-thermal plasma jet in air," in *62nd Gaseous Electronics Conference*. (Saratoga Springs, NY, USA), October 20-23 2009.
- [15] E. Karakas, M. Koklu, A. Begum, and M. Laroussi, "Effects of fluid flow on the characteristics of an atmospheric pressure low temperature plasma jet," in *36th IEEE International Conference on Plasma Science (ICOPS)*, (San Diego, CA, USA), May 31 - June 5 2009.
- [16] M. Laroussi, E. Karakas, and A. Begum, "Experimental investigations of ring-shaped plasma bullets emitted by a pulsed plasma jet," in *17th IEEE International Pulsed Power Conference*, (Washington, DC, USA), 2009.
- [17] M. Laroussi, A. Begum, and E. Karakas. "Role of the species generated by plasma jets in the formation of the plasma bullets," in *36th IEEE International Conference on Plasma Science (ICOPS)*, (San Diego, CA, USA), May 31 - June 5 2009.
- [18] M. Laroussi and E. Karakas, "A study on the cytotoxicity of low temperature plasma," in *36th IEEE International Conference on Plasma Science (ICOPS)*, (San Diego, CA, USA), May 31 - June 5 2009.
- [19] A. Begum, E. Karakas, and M. Laroussi, "Formation, propagation, and contraction of the plasma bullets emitted by a pulsed plasma jet." in *36th IEEE International Conference on Plasma Science (ICOPS)*. (San Diego, CA, USA), May 31 - June 5 2009.
- [20] E. Karakas, A. Begum, M. Lemaster, M. Laroussi, G. McCombs, M. Darby, and W. Hynes, "Experimental investigations of plasma bullets and their effect on streptococcus mutans," in *2nd International Conference on Plasma Medicine (ICPM)*, (San Antonio, TX, USA), March 16-20 2009.
- [21] A. Begum, E. Karakas, and M. Laroussi, "Formation and propagation of the plasma bullets emitted by a pulsed plasma jet." in *61st Annual Gaseous Electronics Conference*, (Dallas, TX), October 13-17 2008.

- [22] A. Begum, E. Karakas, N. Mericam-Bourdet, and M. Laroussi, "Dynamics of the plasma bullets emitted by a pulsed plasma jet," in *Gordon Research Conference (GRC)*, (Mount Holyoke, MA, USA), July 13-19 2008.
- [23] A. Begum, N. Mericam-Bourdet, E. Karakas, S. K. Dhali, and M. Laroussi, "Investigation of the plasma bullets generated by low temperature plasma jets," in *35th IEEE International Conference on Plasma Science (ICOPS)*, (Karlsruhe, Germany), June 15-19 2008.
- [24] J. Kedzierski, J. Engemann, M. Teschke, and D. Korzec, "Atmospheric pressure plasma jets for 2d and 3d materials processing," in *Particle Beams and Plasma Interaction on Materials and Ion Plasma Surface Finishing*, vol. 107, pp. 119–123, Trans. Tech. Pub., 2004.
- [25] M. Teschke, E. G. Finantu-Dinu, D. Korzec, and J. Engemann, "High-speed photographs of a dielectric barrier atmospheric pressure plasma jet," *IEEE Trans. Plasma Sci.*, vol. 33, no. 2, pp. 310–311, 2005.
- [26] M. Laroussi and X. Lu, "Room-temperature atmospheric pressure plasma plume for biomedical applications," *Applied Physics Letters*, vol. 87, pp. 113902-3, 2005.
- [27] M. Laroussi, W. Hynes, T. Akan, X. Lu, and C. Tendo, "The plasma pencil: a source of hypersonic cold plasma bullets for biomedical applications." *IEEE Trans. Plasma Sci.*, vol. 93, pp. 3813–3814, 2008.
- [28] J. Shi, F. Zhong, J. Zhang, D. W. Liu, and M. G. Kong, "A hypersonic plasma bullet train traveling in an atmospheric dielectric-barrier discharge jet." *Physics of Plasmas*, vol. 15, pp. 013504-6, 2008.
- [29] G. S. Selwyn, H. W. Herrmann, J. Park, and I. Hennis, "Materials processing using an atmospheric pressure,rf-generated plasma source," *Contrib. Plasma Phys.*, vol. 6, pp. 610–619, 2001.
- [30] M. Laroussi, "Low temperature plasma-based sterilization: Overview and state-of-the-art," *Plasma Process. Polym.*, vol. 2, pp. 391–400, 2005.



- [31] M. Laroussi, C. Tendero, X. Lu, S. Alla, and W. L. Hynes, "Inactivation of bacteria by the plasma pencil," *Plasma Process. Polym.*, vol. 3, pp. 470–473. 2006.
- [32] M. Laroussi, "Sterilization of contaminated matter with an atmospheric pressure plasma," *IEEE Trans. Plasma Sci.*, vol. 24, no. 3, pp. 1188–1191. 1996.
- [33] E. Stoffels, A. J. Flikweert, W. W. Stoffels, and G. M. W. Kroesen, "Plasma needle: a non-destructive atmospheric plasma source for fine surface treatment of (bio)materials." *Plasma Sources Sci. Technol.*, vol. 11, no. 383-388, 2002.
- [34] G. Fridman, M. Peddinghaus, H. Ayan, A. Fridman, M. Balasubramanian. A. Gutsol, A. Brooks, and G. Friedman, "Blood coagulation and living tissue sterilization by floating electrode dielectric barrier discharge in air," *Plasma Chem. and Plasma Process.*, vol. 26, pp. 425–442, 2006.
- [35] E. Karakas, A. Mulyanyı L. Grenc, and M. Laroussi, "Destruction of  $\alpha$ -synuclein based amyloid fibrils by a low temperature plasma jet" *Appl. Phys. Lett.*, vol. 97, pp. 143702–3. 2010.
- [36] pco. imaging, *Dicam-Pro Operating Instructions*. Donaupark 11 D-93309 Ket-heim. 2004.
- [37] M. Laroussi, X. Lu, V. Kolobov, and R. Arslanbekov. "Power consideration in the pulsed dielectric barrier discharge at atmospheric pressure," *J. Appl. Phys.*, vol. 96, pp. 3028–3030, 2004.
- [38] L. Loeb and J. Meek, "The mechanism of spark discharge in air at a mospheric pressure i," *J. Appl. Phys.* vol. 11, no. 6, pp. 438–447. 1946
- [39] J. Loeb and J. Meek, "The mechanism of spark discharge in air at atmospheric pressure ii," *J. Appl. Phys.*, vol. 11, no. 7, pp. 459–474, 1940.
- [40] L. Loeb, "Recent developments in analysis of the mechanisms of positive and negative coronas in air," *J. Appl. Phys.*, vol. 19, no. 10, pp. 882–897, 1948.
- [41] H.J White, "A study of the initial stages of spark discharges in gases," *Physical Review*, vol. 46, no. 2, pp. 099-0106, 1934

- [42] G. Trichel, "The mechanism of the negative point to plane corona near onset," *Physical Review*, vol. 54, no. 12. pp. 1078–1084, 1938.
- [43] G. Trichel, "The mechanism of the positive point-to-plane corona in air at atmospheric pressure," *Physical Review*, vol. 55, no. 4, pp. 0382–0390, 1939.
- [44] A. Kip, "Onset studies of positive point-to-plane corona in air at atmospheric pressure," *Physical Review*, vol. 55, no. 6, pp. 0549–0556, 1939.
- [45] L. Loeb, *Fundamental processes of electrical discharge*. John Wiley and Sons, Inc, 1939
- [46] L. Loeb. *Basic Processes of Gaseous Electronics*. University of California Press, 1955
- [47] H. Raether. *Electron Avalanches and Breakdown in Gases*. Butterworths: London 1964.
- [48] L. Loeb and J. M. Meek, *The Mechanism of the Electric Spark*. Stanford University Press: Stanford University, 1941.
- [49] G. Dawson and W. Winn, "A model for streamer propagation," *Zeitschrift Fur Physik*, vol. 183, no. 2, p. 159. 1965.
- [50] M. Wang and E. Kunhardt, "Streamer dynamics," *Physical Review A* vol. 42, no 4 pp. 2366–2372. 1990.
- [51] T. Brieis, J. Kos, G. Winands, E. van Veldhuizen, and U. Ebert, "Positive and negative streamers in ambient air: measuring diameter, velocity and dissipated energy." *J. Physics D: Appl. Phys.*, vol 41, no. 23, pp. 234005–11, 2008
- [52] W. Sroka, "Vacuum uv emission of oxygen (gas-ionising radiation of a corona discharge)," *Physics Letters*, vol. 14, no 4, p. 301. 1965.
- [53] W. Sroka, "Excitation of extreme ultra-violet radiation (gas-ionizing radiation) in oxygen by electron collisions," *Physics Letters A*, vol. A 25, no 10, p 770. 1967.
- [54] G. Penney and G. Hummert, "Photoionization measurements in air, oxygen, and nitrogen." *J. Appl. Phys.* vol. 41, no 2, p 572, 1970.

- [55] E. Karakas, M. Koklu, and M. Laroussi. "Correlation between helium mole fraction and plasma bullet propagation in low temperature plasma jets," *J. Phys. D: Appl. Phys.*, vol. 43, pp. 155202–5, 2010.
- [56] K. Urabe, T. Morita, K. Tachibana, and B. Ganguly, "Investigation of discharge mechanisms in helium plasma jet at atmospheric pressure by laser spectroscopic measurements," *J. Phys. D: Appl. Phys.*, vol. 43, no. 9. pp. 095201–13, 2010.
- [57] Y. Sakiyama, D. B. Graves, J. Jarrige, and M. Laroussi, "Finite element analysis of ring-shaped emission profile in plasma bullet," *Appl. Phys. Lett.*, vol. 96, pp. 041501–3, 2010.
- [58] W. Martin, "Energy levels and spectrum of neutral helium (he-4<sub>1</sub>)," *Journal of Research of the National Bureau of Standards Section a-Physics and Chemistry*, vol. 64, no. 1. pp. 19–28, 1960.
- [59] J. Garcia and J. Mack *J. Opt. Soc. Am.*, vol. 55, p. 654, 1965.
- [60] Q. Li, J.-T. Li, W.-C. Zhu, X.-M. Zhu, and Y.-K. Pu, "Effects of gas flow rate on the length of atmospheric pressure nonequilibrium plasma jets," *Appl. Phys. Lett.* vol. 95, pp. 041502–3, 2009.
- [61] R. F. Satti and A. K. Agrawal, "Flow structure in the near-field of buoyant low-density gas jets," *J. Heat and Fluid Flow*, vol. 27, pp. 336–347, 2006.
- [62] Q. Li, X.-M. Zhu, J.-T. Li and Y.-K. Pu, "Role of metastable atoms in the propagation of atmospheric pressure dielectric barrier discharge jets." *J. Appl. Phys.*, vol. 107, pp. 043304–7, 2010.
- [63] Y. B. Golubovskii, V. A. Mayorov, J. Behnke, and J. F. Behnke, "Modeling of the homogeneous barrier discharge in helium at atmospheric pressure," *J. Phys. D: Appl. Phys.*, vol. 36, pp. 39–49, 2003.
- [64] B. M. Smirnov, *Ions and Excited Atoms in Plasma* Moscow: Atomizdat, 1974. In Russian.
- [65] W. J. M. Brok, M. D. Bowden, J. van Dijk, J. J. A. M. van der Mullen, and G. M. W. Kroesen. "Modelling of the homogeneous barrier discharge in helium at atmospheric pressure," *J. Phys. D: Appl. Phys.* vol. 98, p. 13202, 2005.

- [66] F. R. Gilmore, R. R. Laher, and P. Espy *J. Phys. Chem. Ref. Data*, vol. 21, p. 1005, 1992.
- [67] J. W. Shon and M. J. Kushner *J. Appl. Phys.*, vol. 75, p. 1883, 1994.
- [68] F. Krema and M. Zakova. "Pink afterglow in nitrogen-argon mixtures." *Eur. Phys. J. D*, vol. 54, pp. 369–375, 2009.
- [69] G. Nersisyan and W. Graham, "Characterization of a dielectric barrier discharge operating in an open reactor with flowing helium," *Plasma Sources Sci. Technol.*, vol. 13, pp. 582–587, 2004.
- [70] Y. B. Golubovskii, V. Maiorov, J. Behnke, and J. Behnke, "Modelling of the homogeneous barrier discharge in helium at atmospheric pressure," *J. Phys. D: Appl. Phys.*, vol. 36, pp. 39–49, 2003.
- [71] N. Bibinov, A. Fetenev, and K. Wiesemann, "On the influence of metastable reactions on rotational temperatures in dielectric barrier discharges in he- $n_2$ ,"
- [72] R. Deloche, P. Monchicourt, M. Cheret, and F. Lambert. "High-pressure helium afterglow at room temperature." *Physical Review A*, vol. 13, no. 3, pp. 1146–1176, 1976.
- [73] E. Ferguson, F. Fehsenfeld, and A. Schmeltekopf, "Dissociative recombination in helium afterglows." *Physical Review A*, vol. 138, no. 2A, pp. A381–A385, 1965.
- [74] N. Bibinov, A. Fetenev, and K. Wiesemann, "Variations of the gas temperature in he/ $n_2$  barrier discharges." *Plasma Sources Sci. Technol.*, vol. 10, pp. 579–588, 2001.
- [75] K. V. Kozlov, H-EWagner, R. Brandenburg, and P. Michel, "Spatio-temporally resolved spectroscopic diagnostics of the barrier discharge in air at atmospheric pressure," *J. Phys. D: Appl. Phys.*, vol. 34, pp. 3164–3176, 2001.
- [76] A. Shashurin, M. N. Shneider, A. Dogaru, R. B. Miles and M. Keidar. "Temporal behavior of cold atmospheric plasma jet," *App. Phy. Lett.*, vol. 94, pp. 231504–3, 2009.

- [77] J. L. Walsh and M. G. Kong, "Contrasting characteristics of linear-field and cross-field atmospheric plasma jets," *Appl Phys. Lett.*, vol. 93, pp. 111501–3, 2008.
- [78] S. D. Anghel, A. Simon, and T. Frentiu, "Spectroscopic investigations on a low power atmospheric pressure capacitively coupled helium plasma." *Plasma Sources Sci. Technol.*, vol. 17, no. 4, pp. 045016–9, 2008.
- [79] D. Setser, D. Stedman, and J. Coxon, "Chemical applications of metastable argon atoms," *J. Chem. Phys.*, vol. 53, no. 3, pp. 1004–1020, 1970.
- [80] U. Fantz, "Basics of plasma spectroscopy," *Plasma Sources Sci. Technol.* vol. 15, no. S137-S147, 2006.
- [81] U. Fantz, "Atomic and molecular emission spectroscopy in low temperature plasma containing hydrogen and deuterium," ipp-report, Max-Planck-Institut für Plasmaphysik 2002.
- [82] O. Motret, C. Hiberz, S. Pellerin, and J. M. Pouvesle, "Rotational temperature measurements in atmospheric pulsed dielectric barrier discharge gas temperature and molecular fraction effects," *J. Phys. D: Appl. Phys.*, vol. 33, pp. 1493–1498, 2000.
- [83] A. N. Goyette, W. B. Jameson, L. W. Anderson, and J. E. Lawler, "An experimental comparison of rotational temperature and gas kinetic temperature in a  $h_2$  discharge," *J. Phys. D: Appl. Phys.*, vol. 29, pp. 1197–1201, 1996.
- [84] J. Jarrige, E. Karakas, and M. Laroussi, "Dynamics of atmospheric pressure plasma bullets in helium-argon mixtures," in *3rd Gaseous Electronic Conference* (G. D. Sprouse, ed.), vol. 55 of 7, (Paris), p. CTP169, Bulletin of the American Physical Society, October 2010.
- [85] X. M. Zhu, Y. K. Pu, and R. Boswell, "Measurement of the electron density in atmospheric pressure low-temperature argon discharges by line-ratio method of optical emission spectroscopy," *J. Phys. D: Appl. Phys.*, vol. 42, 2009.
- [86] R. F. Boivin, J. L. Kline, and E. E. Scime, "Electron temperature measurement by a helium line intensity ratio method in helicon plasmas," *Physics of Plasmas*, vol. 8, pp. 5303–5314, 2001.

- [87] J. Vlcek, "A collisional-radiative model applicable to argon discharges over a wide range of conditions," *J. Phys. D: Appl. Phys.*, vol. 22, pp. 623-631, 1989.
- [88] V. M. Donnelly, "Plasma electron temperatures and electron energy distributions measured by trace rare gases optical emission spectroscopy," *J. Phys. D: Appl. Phys.*, vol. 37, pp. R217-R236. 2004.
- [89] X. M. Zhu, Y. K. Pu, N. Balcon, and R. Boswell, "Measurement of the electron density in atmospheric-pressure low-temperature argon discharges by line-ratio method of optical emission spectroscopy," *J. Phys. D: Appl. Phys.*, vol. 42, pp. 142003-5, 2009.
- [90] J. Verhoef. "The phagocytic process and the role of component in host defense," *J. Chemother. Suppl.*, vol. 1, no. 5, pp. 93-97, 1991.
- [91] J. Gutteridge, G. Quinlan, and P. Kovacic. "Phigomimetic action antimicrobial agents," *Free Radic. Res.*, vol. 28, no. 1, pp. 1-14, 1998.
- [92] J. Goree, B. Liu, D. Drake, and E. Stoffels. "Killig of *S. Mutans* bacteria using a plasma needle at atmospheric pressure," *IEEE Trans. on Plasma Sci.*, vol. 34, no. 4, pp. 1317-1324, 2006.
- [93] Y. Ma and R. Marquis. "Thermcphysiology of *S. Mutans* and related lactic-acid bacteria," *Antonie Van Leeuwenhoek*, vol. 72, no. 2, pp. 91-100 1997.
- [94] "Laser in densistry: Revolution of dental treatment in the new millenium," International Congress Series, (Amsterdam, The Netherlands), p. 1248. Elsevier. 2003.
- [95] M. Naito, H. Hirkawa, A. Yamashita, N. Ohara, M. Shoji, H. Yukitake, , K. Nakayama, H. Toh, F. Yoshimura, S. Kuhara, M. Hattori, T. Hayashi, and K. Nakayama, "Determination of the genome sequence of porphyromonas gingivalis strain atcc 33277 and genomic comparison with strain w83 revealed extensive genome rearrangements in p. gingivalis," *DNA RESEARCH*, vol. 15, pp. 215-225. 2008.
- [96] F. Chiti and C. M. Dobson. "Protein misfolding, functional amyloid and human disease," *Ann. Rev. Biochem.*, vol. 75, p. 33, 2006.

- [97] G. B. Irvine, O. M. El-Agnaf, G. M. Shankar, and D. M. Walsh, "Protein aggregation in the brain: The molecular basis for alzheimers and parkinsons diseases," *MOL MED*, vol. 14, no. 7-8, pp. 451-464, 2008.
- [98] D. Ozawa, H. Yagi, T. Ban, A. Kameda, T. Kawakami, H. Naiki, and Y. Goto, "Destruction of amyloid fibrils of a  $\beta_2$ -microglobulin fragment by laser beam irradiation." *J. Biol. Chem.*, vol. 284, p. 1009, 2009.
- [99] H. Yagi, D. Ozawa, K. Sakurai, T. Kawakami, H. Kuyama, O. Nishimura, T. Shimanouchi, R. Kuboi, H. Naiki, and Y. Goto. "Laser-induced propagation and destruction of amyloid  $\beta$  fibrils," *J. Biol. Chem.*, vol. 285, p. 19660. 2010.
- [100] E. Chatani, Y. Lee, H. Yagi, Y. Yoshimura, H. Naiki, and Y. Goto *Proc Natl Acad Sci USA*, vol. 106, p. 11119, 2009.
- [101] W.-F. Xue, A. Hellewell, W. Gosal, S. Homans, E. Hewitt, and S. Radford *J. Biol. Chem.*, vol. 284, p. 34272, 2009.

## VITA

ERDINC KARAKAS

Department of Electrical and Computer Engineering  
Old Dominion University  
Norfolk, VA 23529

Erdinc Karakas was born in Odemis/IZMIR, TURKEY. He obtained his B.Sc. in Physics and Mathematics (double majoring) from Eskisehir Osmangazi University. He received M.Sc. and M.Ed. degrees from Eskisehir Osmangazi University and Anadolu University, in Plasma Physics and Physics Education, respectively. After a few years teaching, he joined Dr. Laroussi's group as a Graduate Research Assistant in 2007 at Old Dominion University (ODU). He studied atmospheric pressure low temperature plasma jets and their biomedical applications during his Ph.D. research. Erdinc Karakas has authored and co-authored 7 refereed journal publications, 5 conference papers, and more than 25 oral or poster presentations. He is an IEEE member since 2007. He is the recipient of the 2010 Outstanding Ph.D. Researcher Award from Department of Electrical and Computer Engineering, ODU. His oral presentation at the 63<sup>rd</sup> Gaseous Electronics Conference in Paris, France, was nominated as the best student award. Upon graduation in April 2011 with his Ph.D. from ODU, he will work with Prof. Vincent M. Donnelly and Prof. Demetre J. Economou in the Department of Chemical and Biomolecular Engineering at the University of Houston as a post-doctoral research associate.